MATERIALS TECHNOLOGY FOR COAL-CONVERSION PROCESSES

Thirteenth Quarterly Report,
January—March 1978

ANL-78-54

ARGONNE NATIONAL LABORATORY
9700 South Cass Avenue
Argonne, Illinois 60439

MATERIALS TECHNOLOGY FOR COAL-CONVERSION PROCESSES

Thirteenth Quarterly Report,
January—March 1978

W. A. Ellingson
Project Leader

Materials Science Division

Previous reports in this series

ANL-76-7	July—September 1975
ANL-76-22	October—December 1975
ANL-76-60	January—March 1976
ANL-76-111	April—June 1976
ANL-76-125	July—September 1976
ANL-77-5	October—December 1976
ANL-77-41	January—March 1977
ANL-77-62	April—June 1977
ANL-78-6	July—December 1977

TABLE OF CONTENTS

LIST OF FIGURES

HIGHLIGHTS

Task A -- <u>Evaluation of Ceramic Refractories for Slagging Gasifiers</u>
<u>(C.R. Kennedy, R.J. Fousek, D.J. Jones, and R.B. Poeppel)</u>

The preliminary results of run 6 have been revised and are presented.
Although a temperature excursion to $\sim$ 1700-1800°C that occurred during this
test makes intertest comparison difficult, refractory number 38, a fused-cast
Al_2O_3-Cr_2O_3 composition, exhibited promising corrosion resistance and will be
retested.

Test runs 7 and 8 were completed. The corrosion resistances of
Al_2O_3-Cr_2O_3 bricks (numbers 23, 852, and 260) and ramming mixes (numbers 18 and
88) were very good, although several bricks (numbers 260 and 852) seemed to
possess poor thermal-shock characteristics.

Several samples of slag and the slag outlet block were obtained from
the Bi-Gas pilot plant in Homer City, PA. The composition of the CaO-fluxed
Montana Rosebud slag from Bi-Gas was found to be very close to that of the
simulated Montana Rosebud slag utilized in tests 5-8. The slag outlet block
showed only minimal corrosion in 114 h of operating time.

Task C -- <u>Application and Development of Nondestructive Evaluation Methods for</u>
<u>Coal-conversion Processes</u> (W.A. Ellingson, K.J. Reimann, W.J. Shack,
and C.A. Youngdahl)

The HYGAS external cyclone separator was again ultrasonically
inspected after an additional 1092 hours of operation (total exposure now
3142 h). The erosive wear was shown to be significant and will be more
frequently inspected for optimizing replacement time. Additional results
from ANL Instrumented Elbow II in the main coal feed line of the Synthane
pilot plant after transfer of 133000 kg of coal indicated small amounts of
erosive wear comparable to the error band of the field measurements
($\sim$ 0.13 mm/measurement). Data from the Bi-Gas plant transfer lines have
been refined by further measurements and analysis, and the amount of
erosion appears to have been very small: techniques have been introduced
to improve the measuring accuracy in order to detect the wall-thickness
changes. In-service tests of the operation of the erosive-wear monitoring
system are planned. Improved methods of attachment of ultrasonic wave-
guides to specimen piping are being tested. Experiments and analysis to
develop methods for characterization of eroded metallic surfaces by exami-
nation of reflected ultrasonic pulse echos are in progress.

Amplitude-distribution analyses of acoustic emissions from two thick
refractory-concrete samples, one fired at a slow heating rate ($\sim$ 50°C/hr)
and one at a fast heating rate ($\sim$ 300°C/hr), suggest that this parameter may
be a useful real-time indicator. The fast heating rate produced consistently

lower characteristic slope values than the slow heating rate; however, significant acoustic activity was detected during cooling of the slowly heated panel, whereas little additional activity was detected during cooling of the panel with the faster heating rate.

Task D -- Corrosion Behavior of Materials in Coal-conversion Processes
(K. Natesan)

Uniaxial tensile data were generated for Incoloy 800, Type 310 stainless steel, U.S. Steel Alloy 18-18-2, and Inconel 671 in the as-received condition and after 1000-h exposures to multicomponent gas mixtures that simulate a coal-gasification environment. The results, obtained at 871 and 750°C, showed a decrease in the flow stress of the material after exposure to complex gas mixtures, when compared with that of the as-received material. The preexposure of the materials to complex gas mixtures resulted in a decrease in 0.2% yield stress and ultimate tensile strength with only minimal increases in the uniform strain over the range of $\sim$ 4 to 10%.

Task E -- Erosion Behavior of Materials in Coal-Conversion Processes
(W.J. Shack and J.Y. Park)

The erosion test apparatus was assembled for preliminary check out and room-temperature calibration. New rotor designs were completed to allow higher particle speeds and better control of particle impingement angle. Preliminary room-temperature erosion tests were performed on six materials with 50-μm Al_2O_3 particles at a velocity of 70 m/s and at five impact angles.

Task F -- Component Performance and Failure Analysis (S. Danyluk, G.M. Dragel, W.J. Shack, and J.Y. Park)

Failed components from the HYGAS Pilot Plant (hydrogen-compressor leaf spring and pump hinge-pin), the HYGAS Ash Agglomerating Gasifier (internal cyclones), and the Grand Forks Energy Research Center (taphole cooling coil) were examined in this quarter.

MATERIALS TECHNOLOGY FOR COAL-CONVERSION
PROCESSES: THIRTEENTH QUARTERLY REPORT,
JANUARY-MARCH 1978

ABSTRACT

This broad-base materials engineering program, begun
in 1974, includes studies on ceramic (refractory) and metal-
lic materials presently being used or intended for use in
coal-conversion processes. The program entails studies
of erosive wear, nondestructive testing, corrosion, re-
fractory degradation, and failure analysis. Appropriate
laboratory and field experiments are integrated such that
the results have impact on present pilot-plant and proposed
demonstration-plant designs. This quarterly report, for the
period January-March 1978, presents the technical accomplish-
ments of the program.

INTRODUCTION

The economical conversion of coal into clean and usable fuels will be
advanced through the use of durable materials systems. The technical infor-
mation base required for materials selection in plant design for the operating
environments of various coal-conversion processes is extremely limited. Hence,
reliable selection and life-time prediction methods of materials under these
conditions are not available. This project is designed to provide part of
the materials information necessary for successful operation of coal-conversion
systems. The present report is the thirteenth quarterly progress report sub-
mitted by ANL to the Division of Coal Conversion under project Number 7106,
"Materials Technology for Coal Conversion Processes."

The project includes six tasks: (A) evaluation of commercial re-
fractories exposed to coal slag under conditions typical of those encountered
in slagging gasification processes; (B) evaluation of erosion/corrosion-
resistant coatings when exposed to prototype operating environments; (C) de-
velopment, evaluation, and application of nondestructive evaluation methods
applicable to coal-conversion systems; (D) evaluation of the corrosion be-
havior of commercial alloys; (e) development of analytical models to predict
the erosive-wear behavior of materials used in coal-conversion plants; and
(F) analysis of failed coal-conversion plant components.

1

Task A -- Evaluation of Ceramic Refractories for Slagging Gasifiers
(C.R. Kennedy, R.J. Fousek, D.J. Jones, and R.B. Poeppel)

As reported previously[1], the sixth run, which was designed to evaluate the corrosion resistance of three fused-cast bricks (numbers 2, 38, and 39) and one high-density sintered brick (number 40) to a simulated Montana Rosebud slag, has been completed. Cut sections of the 3/4-length bricks and the temperature history of the test have also been described.[1] Note that after ∿ 300 h at 1500°C, a malfunction caused the furnace plenum temperature to reach 1700-1800°C. The detailed chemical analysis from run 6 has been received and is shown in Table I. The preliminary results from run 6 have been revised and are presented in Table II.

In light of the severe conditions in this test, as indicated by the large depth of removal and penetration in the other compositions, refractory number 38, a fused-cast solid solution of alumina-chromia within a complex alumina-chromia spinel, exhibited good corrosion resistance. However, extensive thermal-shock cracking parallel to the hot face occurred in both numbers 38 and 2 during the test.

Test run 7 exposed alumina-chromia and alumina-silica refractories to a simulated Montana Rosebud slag, the composition of which is presented as a function of time in Table III. Full-, 3/4-, and 1/2-length bricks of four different refractories listed in Table IV were first exposed to a slag pool (∿ 30 mm in depth) at 1500°C for 48 h (see Fig. 1). Then additional slag was added to the bath until it was 80 mm in depth, and the refractories were held at 1500°C for 480 h. Oxygen partial pressure was maintained at ∿ 10^{-3} Pa throughout the test. The thermal profile that existed within each refractory on October 12, 1977 is shown in Fig. 2. The refractory-slag interfacial temperature was 1380-1430°C as determined by a pyrometer. Two lines of slag attack are visible on refractory number 17 (see arrows on Fig. 3b), the least corrosion-resistant refractory, whereas only one line of slag attack (corresponding to the exposure for 480 h at 1500°C) is visible on the other three refractories. The two alumina-chromia refractories (numbers 23 and 852) performed the best, exhibiting only slight attack after 480 h (2-4 mm on the full-length bricks). These results are in contrast to those in test run 3, in which uncooled bricks of refractories 23 and 852 performed somewhat poorly. As with the silicon carbides[2], the corrosion resistance of the alumina-chromia refractories improved significantly with water cooling. Comparison with results of test 5 reveals that, when exposed to an acidic slag, the alumina-chromia refractories outperformed the magnesia-chromia refractories with respect to corrosion resistance. However, as a result of the thermal gradient, the front faces of the number 852 bricks cracked at an ∿ 45° angle to the top front edge.

Test run 8 evaluated 1/2- and full-length specimens of five ramming mixes (two alumina-silica, two alumina-chromia, and one alumina-magnesia) and one sintered alumina-chromia refractory, number 260 (Table V). Wedge-shaped bricks were produced from the five as-received mixes by hand-ramming into a rigid mold with removable sides. Care was taken to minimize lamination of the material. Each set of bricks was dried and cured according to the manufacturer's instructions. The cured bricks were then placed in the slag corrosion furnace and the hot face was heated to 1500°C for ∿ 2 h while the cold face was maintained at

∿ 80°C. The furnace was then cooled to room temperature and the initial charge of slag was introduced to a depth of ∿ 15 mm.

Also included in this test was a 115-mm x 64-mm x 54-mm piece of refractory number 2. This specimen was placed in the slag bath near the center of the furnace and was not water-cooled (Fig. 4). Its purpose was to serve as a standard by which intertest comparisons could be made. Similar specimens will be included in all future tests. The densities of this standard (number 2) and future standards are presented in Table VI.

The temperature history of run 8 is presented in Fig. 5. A simulated Montana Rosebud slag (B/A = 0.7) was introduced to a depth of ∿ 15 mm, and the plenum temperature was raised to ∿ 1600°C for ∿ 24 h with a partial pressure of oxygen (ppO_2) of ∿ 10^{-2} Pa. The temperature of the brick-slag interface was added to raise the level to 60 mm. The furnace was held at ∿ 1500°C (brick-slag interface 1400–1430°C) for 475 h with a ppO_2 of ∿ 10^{-3} Pa. The temperature pro-files within each refractory at mid-depth are shown for furnace-plenum tem-peratures of 1610°C (Fig. 6) and 1520°C (Fig. 7). A detailed analysis of the composition of the slag as a function of time will be presented in the next report. Examination of the refractories and the standard reveals two lines of slag attack (Figs. 8–10). Since the vertical thermal gradient in the slag pool is steep (∿ 7°C/mm), the 475-h hold at 1500°C had a negligible effect on the bottom slag line. Thus, the bottom line of attack corresponds to 24 h at 1600°C whereas the top line of attack is the result of the 475-h exposure at 1500°C. Table V summarizes the relative resistance of the refractories tested in run 8. The alumina-chromia compositions exhibited superior corrosion resistance, even during the short exposure at 1600°C. Brick number 260, a sintered Al_2O_3-Cr_2O_3 com-position, showed almost no attack, although a number of deep thermal-shock cracks developed during the test. Note that a crack parallel to the hot face of brick number 260, ∿ 20–30 mm from it (Fig. 9a), completely separated the hotter and cooler (not shown) portions of the brick. Refractory number 18, an Al_2O_3-Cr_2O_3 ramming mix, also exhibited negligible corrosion but substantial cracking which may have resulted from either thermal shock or physical growth. Since the amount of slag penetration in refractories 260 and 18 was difficult to determine visually because of their dark color, energy-dispersive X-ray analysis will be performed in an attempt to quantify the penetration. The other Al_2O_3-Cr_2O_3 ramming mix, number 88, did not crack and was also very resistant to corrosion although it did suffer considerable penetration. The Al_2O_3-SiO_2 ramming mixes, numbers 90 and 95, and the Al_2O_3-MgO ramming mix, number 220, did not exhibit any thermal shock cracks, but were much less resistant to corrosion than the Al_2O_3-Cr_2O_3 ramming mixes. These results are nearly identical to the results of run 7, which evaluated the relative corrosion resistances of Al_2O_3-SiO_2 and Al_2O_3-Cr_2O_3 sintered refractories.

In order to insure the applicability of the results from ANL's slag corrosion tests to pilot-plant conditions, several samples of slag and slag-outlet block were obtained from the Bi-Gas Plant in Homer City, PA. The slag-outlet block, fabricated from refractory number 2 by fusion casting and grinding, was ∿ 380 mm (15 in.) wide by ∿ 255 mm (10 in.) high and had a conical interior hole with a minimum diameter of 152 mm (6 in.). The block had experienced 114 h of coal feed before it was removed from the slag outlet assembly on

August 25, 1977.[3] During removal, it was fractured into numerous pieces, not all of which were received by ANL. Those pieces that were received were fitted together and are shown in Fig. 11. Many thermal-shock cracks, in addition to the fractures that occurred during removal, are evident. The hot faces of the block were covered with coal char, which had also penetrated into the thermal-shock cracks. Surprisingly, only a small amount of slag had adhered to the hot face, with little evidence of corrosion. A possible explanation for this observation is that a carbonaceous layer may have formed on the hot face of the refractory during startup, preventing the slag from adhering to the refractory. A core-drilled specimen was taken from an area where the slag had adhered to the refractory, and will be examined by scanning-electron microscopy (SEM). The diameter of the central hole was $\sim$ 150 mm (6 in.), indicating that only minimal material loss had occurred in the short time of operation. Three slag samples were also obtained from Bi-Gas and have been chemically analyzed (Table VII). The slag from Bi-Gas test G2P was from a Rosebud coal with no fluxing agent. However, since difficulties were experienced at Bi-Gas with plugging of the outlet hole by the slag, CaO was added to the coal to reduce the slag viscosity. Slags from tests G3 and G3E were from Rosebud coal with a CaO flux; the compositions of these slags are very similar to that of the simulated Rosebud slag utilized by ANL for tests 5-8.

TABLE I. Composition of Slag (wt %) During Corrosion
Test Run 6

	Exposure Time, h		
Component	8	137	303
SiO_2 (S)	40.6	40.1	35.5
Al_2O_3 (A)	18.0	17.8	24.8
Fe_2O_3 (F_1)	1.2	1.4	1.6
FeO (F_2)	6.0	5.8	5.0
CaO (C)	23.5	24.7	24.7
MgO (M)	6.9	6.9	6.9
Na_2O (N)	1.4	1.2	0.2
K_2O (K)	1.1	0.8	0.1
TiO_2 (T)	1.1	1.1	0.9
Other	0.2	0.2	0.3
. . . .			
B/A Ratio[a]	0.7	0.7	0.6
Ferritic Content[b], %	15	17	22

[a] Base-to-acid ratio $B/A = (F_1 + F_2 + C + M + N + K)/$

$$(S + A + T).$$

[b] Ferritic content $= \dfrac{wt\ \%\ Fe_2O_3}{wt\ \%\ Fe_2O_3 + 1.11\ wt\ \%\ FeO + 1.43\ wt\ \%\ Fe}$.

TABLE II. Relative Resistance to Corrosion of Refractories Exposed to Slag Attack in Run 6

Refractory Number	Composition	Depth of Removal, mm[a]			Depth of Obvious Penetration, mm[a]			Depth of Microstructural Alteration, mm		
		Full Length	3/4 Length	1/2 Length	Full Length	3/4 Length	1/2 Length	Full Length	3/4 Length	1/2 Length
2	Al_2O_3(99.3)-Na_2O(0.4)-CaO(0.1) (Fused Cast)	20	18	16	52	50	∿50	–	–	–
38	Al_2O_3(60.4)-Cr_2O_3(27.3)-MgO(6.0) -Fe_2O_3(4.2)-SiO_2(1.8) (Fused Cast)	10	8	9	∿12	10	∿10	–	–	–
39	MgO(56.5)-Cr_2O_3(20.0)-Fe_2O_3(10.5) -Al_2O_3(8.0)-SiO_2(2.5) -TiO_2(1.5)-CaO(0.5) (Fused Cast)	25	28	24	65	32	∿70	∿105	118	∿95
40	MgO(60.8)-Cr_2O_3(18.6)-Fe_2O_3(11.0) -Al_2O_3(6.6)-CaO(1.9) -SiO_2(1.1) (Sintered)	34	27	25	44	32	35	∿100	70	40

[a]Measured from the original hot face

TABLE III. Composition of Slag (wt %) During Corrosion
Test Run 7

Component	Exposure Time, h			
	7	192	387	499
SiO_2 (S)	37.9	39.4	40.6	39.7
Al_2O_3 (A)	18.1	16.4	16.6	17.2
Fe_2O_3 (F_1)	1.3	3.6	2.9	3.5
FeO (F_2)	6.1	4.4	4.6	4.5
CaO (C)	25.9	25.8	26.1	25.6
MgO (M)	6.4	6.3	6.2	6.8
Na_2O (N)	1.7	1.5	1.0	0.9
K_2O (K)	1.4	1.3	0.7	0.5
TiO_2 (T)	1.0	1.2	1.1	1.2
Other	0.2	0.1	0.2	0.1
. . . .	. . . .	. . . .	. . . .	. . . .
B/A Ratio[a]	0.8	0.8	0.7	0.7
Ferritic Content[b], %	16	43	31	42

[a]Base-to-acid ratio B/A = $(F_1 + F_2 + C + M + N + K)/(S + A + T)$.

[b]Ferritic content = $\dfrac{\text{wt } \% \text{ } Fe_2O_3}{\text{wt } \% \text{ } Fe_2O_3 + 1.11 \text{ wt } \% \text{ FeO} + 1.43 \text{ wt } \% \text{ Fe}}$.

TABLE IV.   Relative Resistance to Corrosion of Refractories Exposed to Slag Attack in Run 7

Refractory Number	Composition	Attack Line	Maximum Depth of Removal[a], mm			Maximum Depth of Penetration[a], mm		
			Full Length	3/4 Length	1/2 Length	Full Length	3/4 Length	1/2 Length
14	$Al_2O_3(91.6)-SiO_2(8.0)-Fe_2O_3(0.15)-$ Alkali(0.15) (Sintered)	Top	9	5	6	10	6	7
17	$Al_2O_3(83.9)-SiO_2(9.0)-Fe_2O_3(1.0)-$ $TiO_2(2.3)-P_2O_5(3.6)$ (Chemically Bonded)	Top Bottom	13 3	11 4	11 3	17 −	16 −	14 −
23	$Al_2O_3(89.7)-Cr_2O_3(10.0)-SiO_2(0.1)-$ $Fe_2O_3(0.1)-$Alkali(0.1) (Sintered)	Top	4	2	2	7	7	6
852	$Al_2O_3(81.1)-Cr_2O_3(16.6)-P_2O_5(0.8)-$ $SiO_2(0.5)-Fe_2O_3(0.5)-$ $Na_2O(0.5)$ (Chemically Bonded)	Top	2	2	1	8	9	4

[a]Measured from the original hot face.

8

TABLE V. Relative Resistance to Corrosion of Refractories Exposed to Slag Attack in Run 8

Refractory Number	Composition	Attack Line	Maximum Depth of Removal[a], mm		Maximum Depth of Penetration[a], mm	
			Full Length	1/2 Length	Full Length	1/2 Length
18	$Cr_2O_3(39.6)-Al_2O_3(21.4)-Fe_2O_3(22.6)-$ $MgO(9.6)-SiO_2(2.5)-$ $TiO_2(0.6)-P_2O_5(3.7)$ (Ramming Mix)	Top Bottom	∿1 ∿1	2 ?	45? 30?	30? ?
88	$Al_2O_3(85.2)-Cr_2O_3(9.7)-SiO_2(1.9)-$ $Fe_2O_3(0.5)-Na_2O(0.4)-$ $P_2O_5(2.3)$ (Ramming Mix)	Top Bottom	3 4	1 2	20 12	12 10
90	$Al_2O_3(89.5)-SiO_2(6.0)-Alkali(0.2)-$ $P_2O_5(3.7)-Other(0.6)$ (Ramming Mix)	Top Bottom	8 9	4 7	11 14	5 8
220	$Al_2O_3(89.6)-MgO(3.4)-SiO_2(0.7)-$ $P_2O_5(6.2)-Alkali(0.1)$ (Ramming Mix)	Top Bottom	8 9	7 7	23 24	20 10
95	$Al_2O_3(95)-SiO_2(0.2)-Na_2O(0.2)-$ $Fe_2O_3(0.05)-P_2O_5(4.55)$ (Ramming Mix)	Top Bottom	10 9	7 10	40 42	32 32
260	$Al_2O_3-Cr_2O_3$ (Sintered)	Top Bottom	1 2	2 2	20? ?	? ?

[a]Measured from the original hot face.

6

TABLE VI. Apparent Density and Open
Porosity of Standards Cut from
Refractory Number 2 Bricks

Number	Apparent Density, g/cm^3	Open Porosity, %
1	3.64	0.7
2	3.66	0.6
3	3.62	0.8
4	3.61	0.8
5	3.66	0.7

TABLE VII. Composition of Slag (wt %) from Bi-Gas Pilot Plant

Component	Sample Number		
	G2P	G3	G3E
SiO_2 (S)	46.2	37.0	42.1
Al_2O_3 (A)	17.5	20.6	15.3
Fe_2O_3 (F_1)	1.2	1.8	1.3
FeO (F_2)	5.1	3.1	5.0
CaO (C)	22.6	30.6	30.2
MgO (M)	5.3	4.0	4.0
Na_2O (N)	0.4	1.6	0.4
K_2O (K)	0.2	0.3	0.4
TiO_2 (T)	0.9	0.7	0.8
Other	0.6	0.3	0.5
. . . .			
B/A Ratio[a]	0.5	0.7	0.7
Ferritic Content[b], %	17	34	19

[a] Base-to-acid ratio $B/A = (F_1 + F_2 + C + M + N + K)/(S + A + T)$.

[b] Ferritic content $= \dfrac{wt \% \ Fe_2O_3}{wt \% \ Fe_2O_3 + 1.11 \ wt \% \ FeO + 1.43 \ wt \% \ Fe}$.
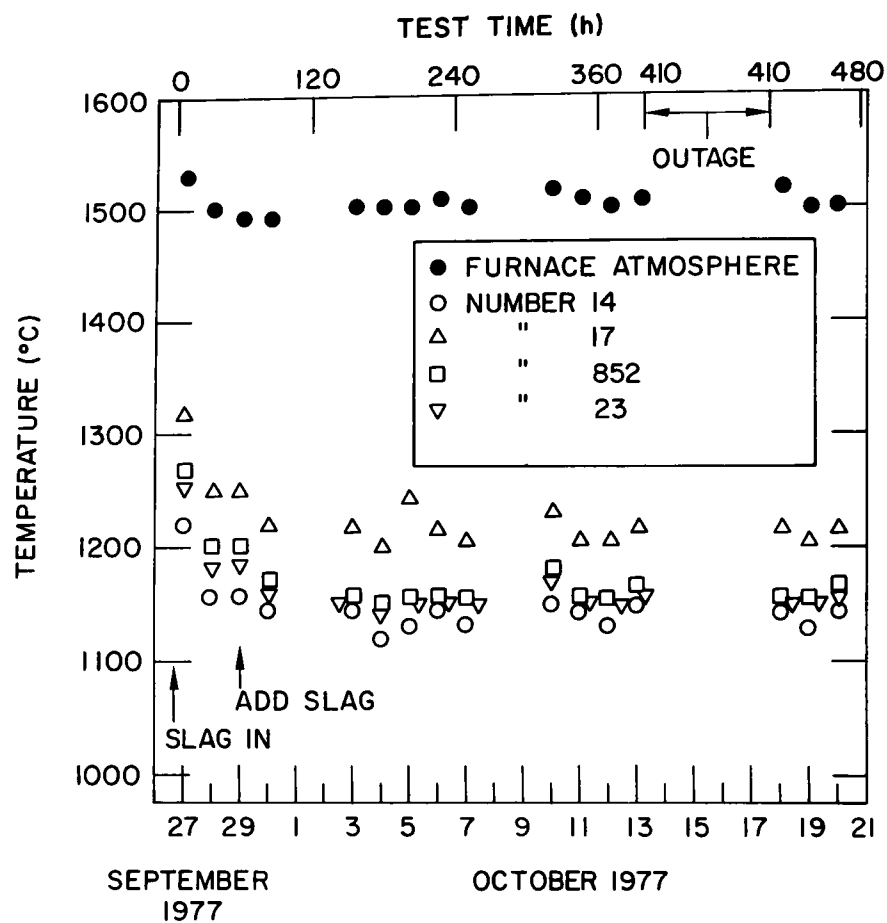
Fig. 1. Furnace Plenum Temperature and Brick Temperatures 12.7 mm (0.5 in.) from Hot Face of Each Composition During Test Run 7. Neg. No. ANL-306-78-416.
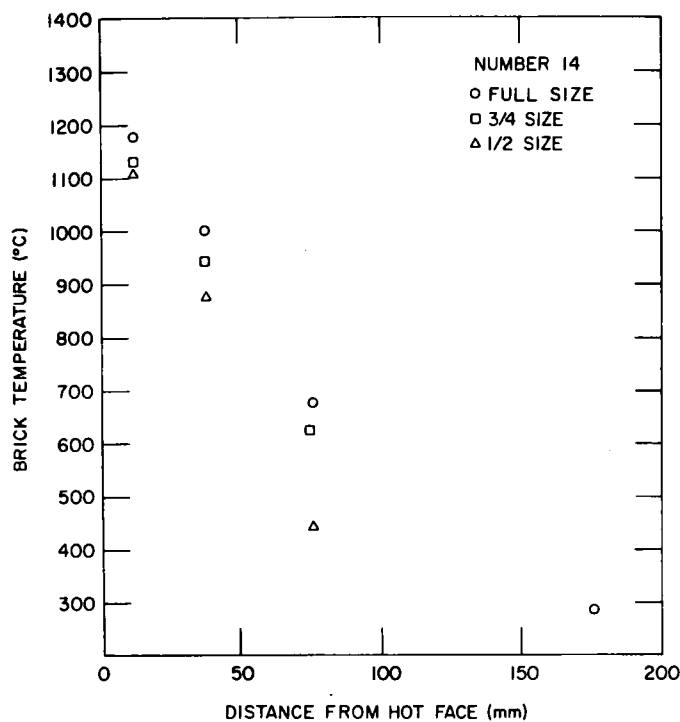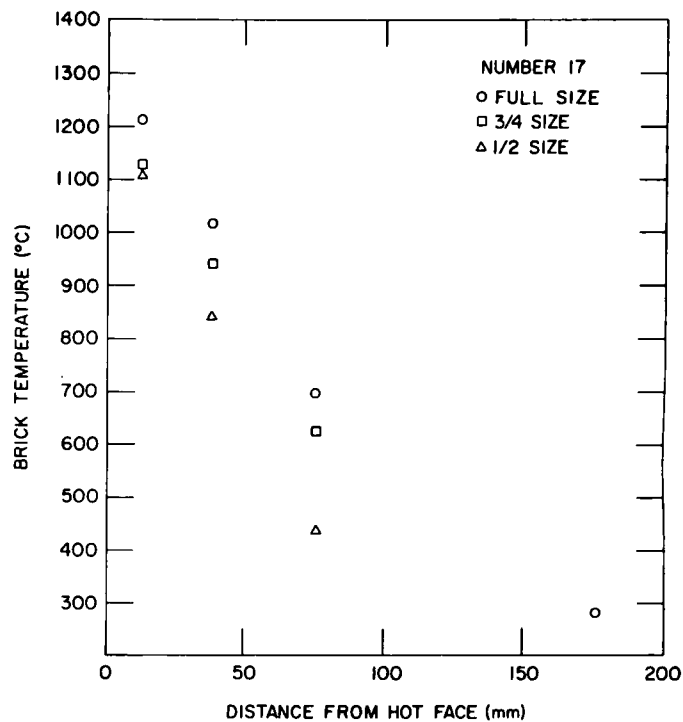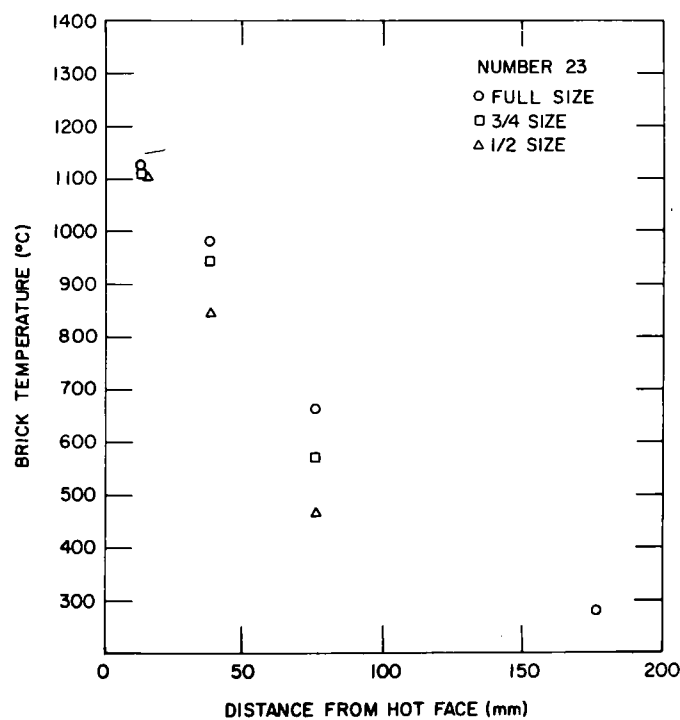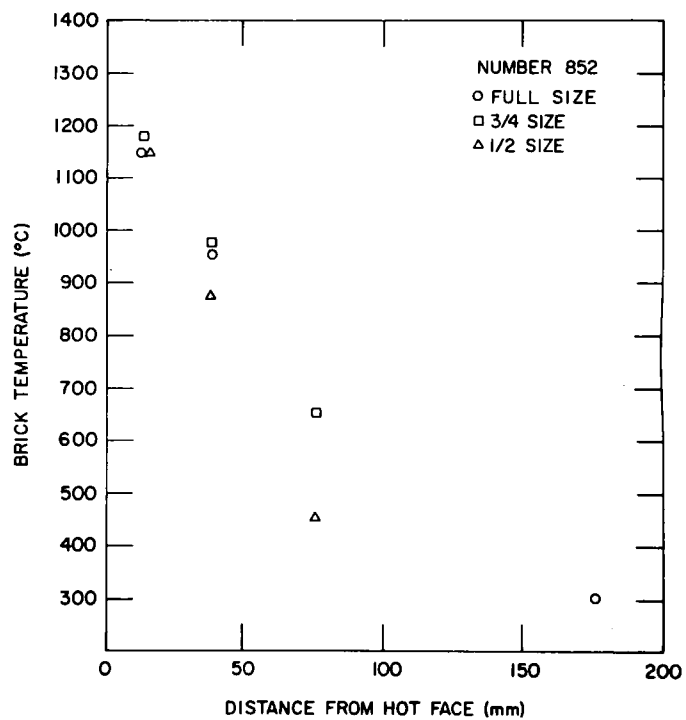
Fig. 2. Temperatures in Bricks at Midheight During Test Run 7 at Four Locations in Full-length Bricks and at Three Locations in 3/4- and 1/2-length Bricks (a) Alumina-silica (Number 14), (b) alumina-silica (Number 17), (c) alumina-chromia (Number 23), and (d) alumina-chromia (Number 852). Neg. Nos. ANL 306-78-425, 306-78-426, 306-78-431, 306-78-432
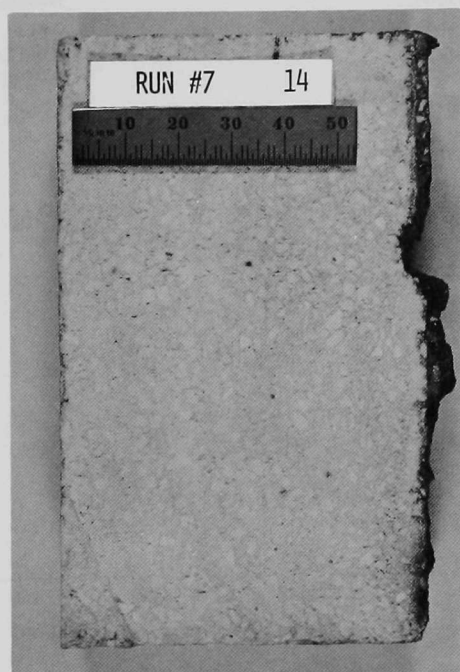
(a)
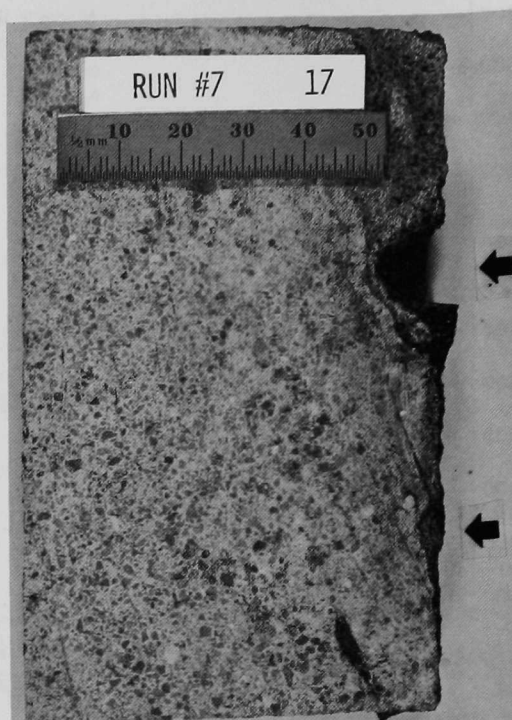
(b)
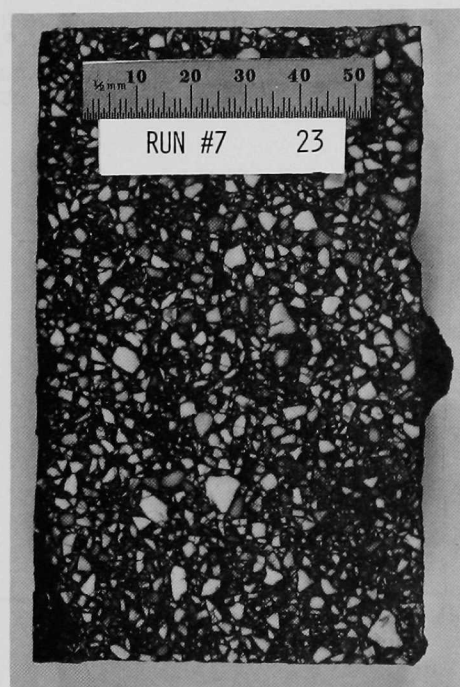
(c)

(d)

Fig. 3. Cut Sections of the 3/4-length Refractories Exposed to Slag Attack in Run 7. (a) Alumina-silica (Number 14), (b) alumina-silica (Number 17), (c) alumina-chromia (Number 23), and (d) alumina-chromia (Number 852). The vertical face on the right-hand side of each brick was exposed to the slag. Two lines of slag attack [see arrows in (b)] are visible on brick number 17.
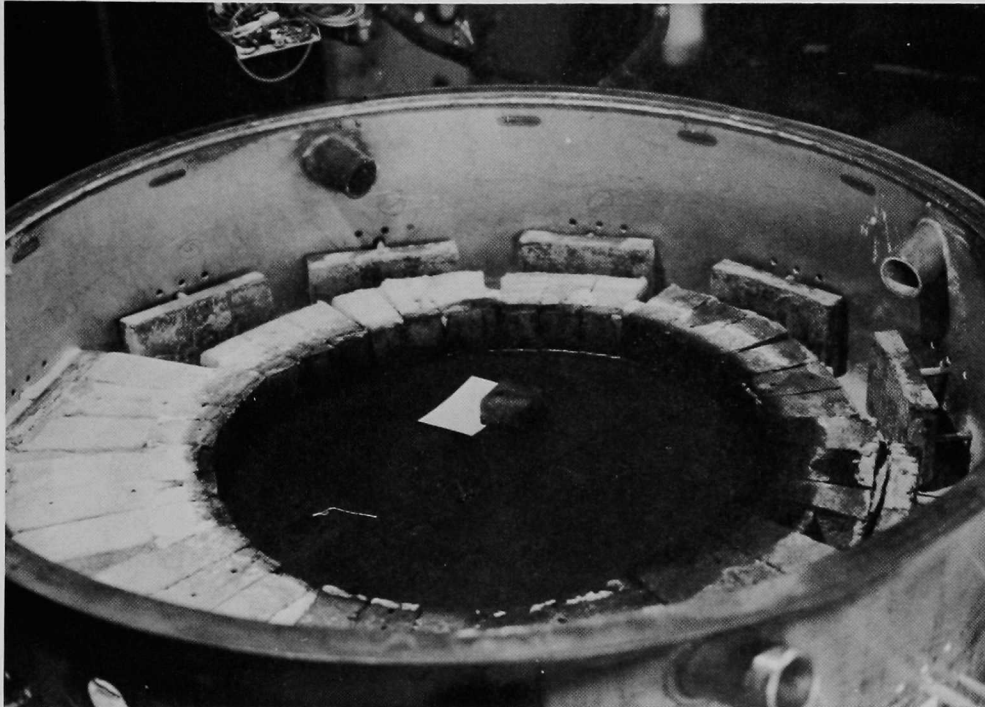
Fig. 4. Posttest Photograph Showing the Placement of the
Standard Specimen of Refractory Number 2. Note that the
furnace has been partially disassembled, the insulating
upper wall has been removed, and the cooling cans for
the 1/2-size bricks have been detached.
A 76-mm x 127-mm (3-in. x 5-in.) file card has been
placed next to the specimen to illustrate the depth
of corrosion.
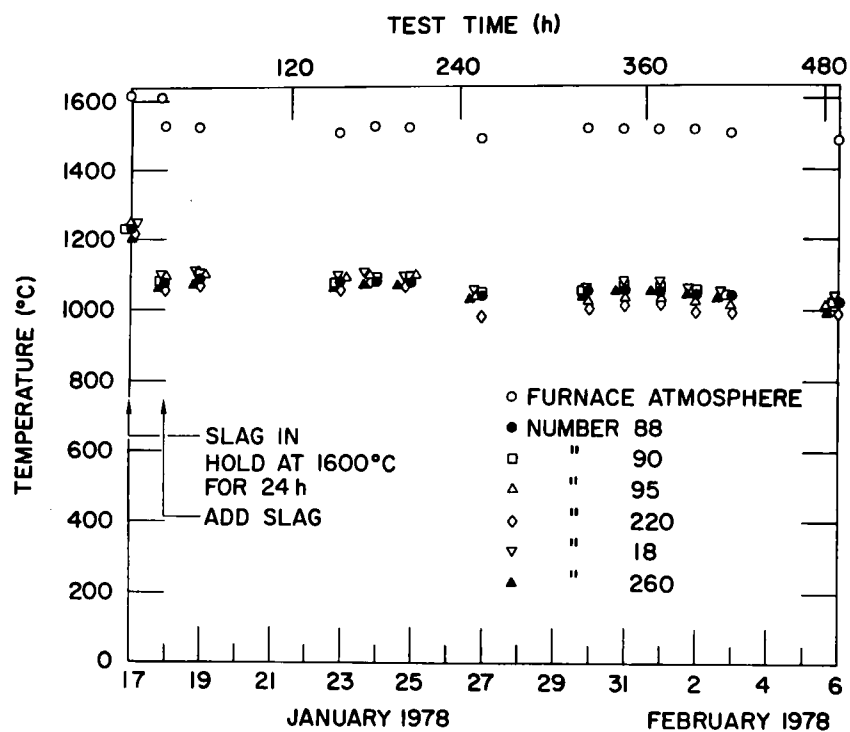
Fig. 5.   Furnace Plenum Temperature and Brick Temperatures 38.1 mm (1.5 in.)
from the Hot Face of Full-size Bricks of Each Composition During
Test Run 8.   Neg. No. ANL-306-78-417

16
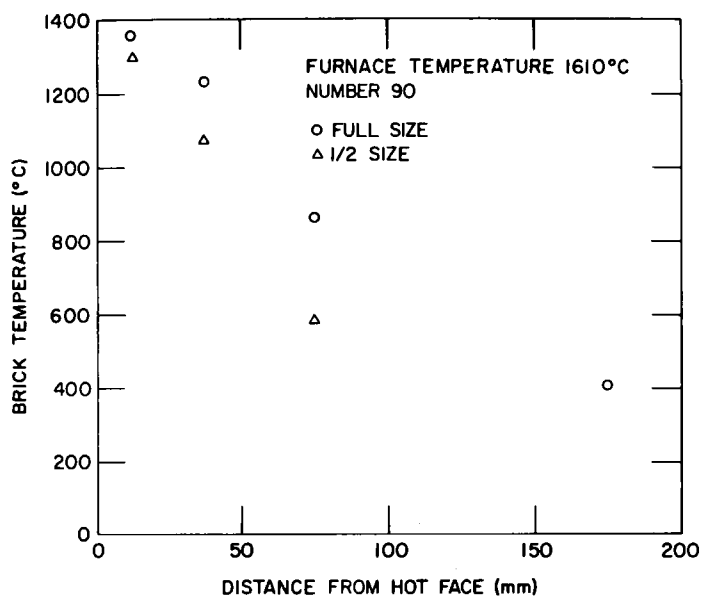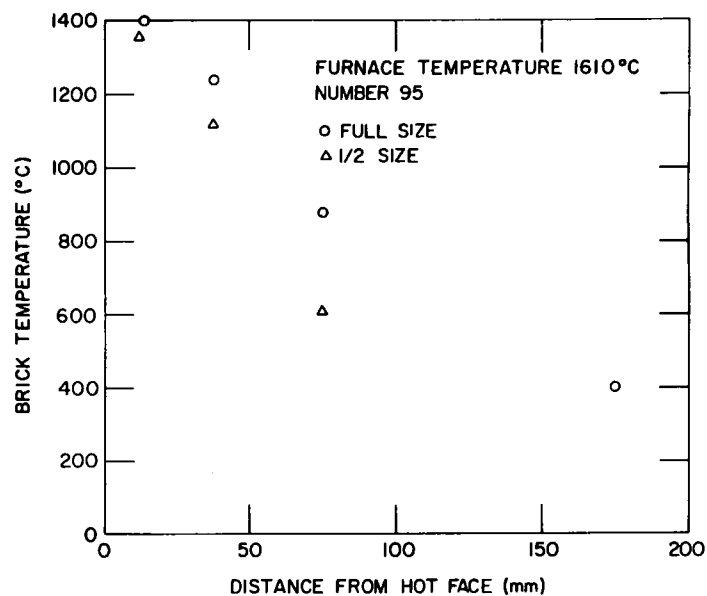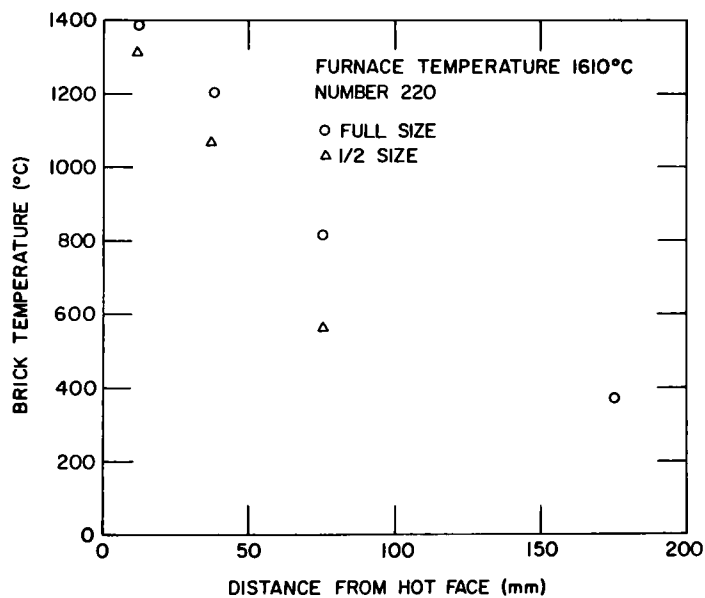
Fig. 6. Brick Temperature at Mid-height Versus Distance from Hot Face.
(a) Number 90, (b) Number 95, (c) Number 220, (d) Number 18, (e) Number 260, and (f) Number 88. Furnace plenum temperature = 1610°C.
ANL Neg. Nos. 306-78-420, 306-78-22, 306-78-24, 306-78-28, 306-78-429, 306-78-446.
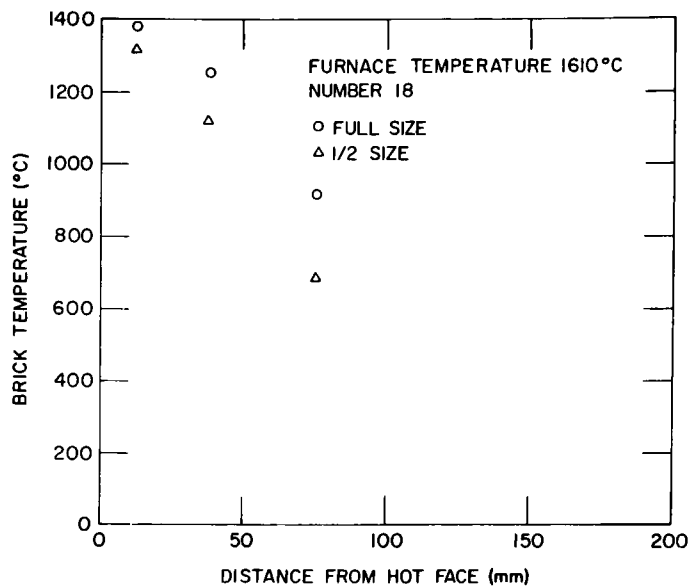
(d)
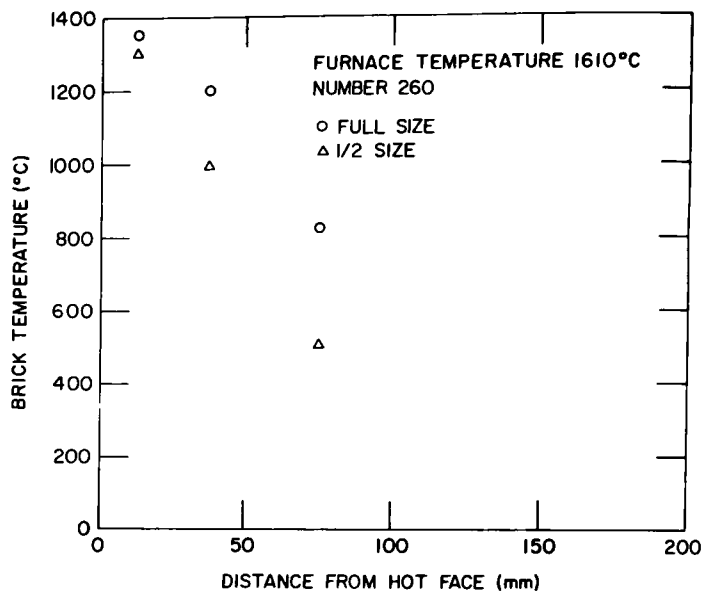
(e)
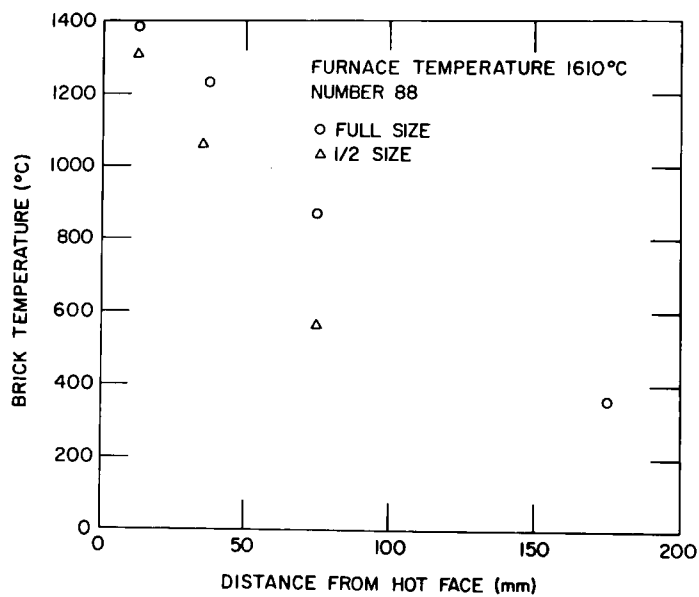
(f)

Fig. 6 (cont'd).
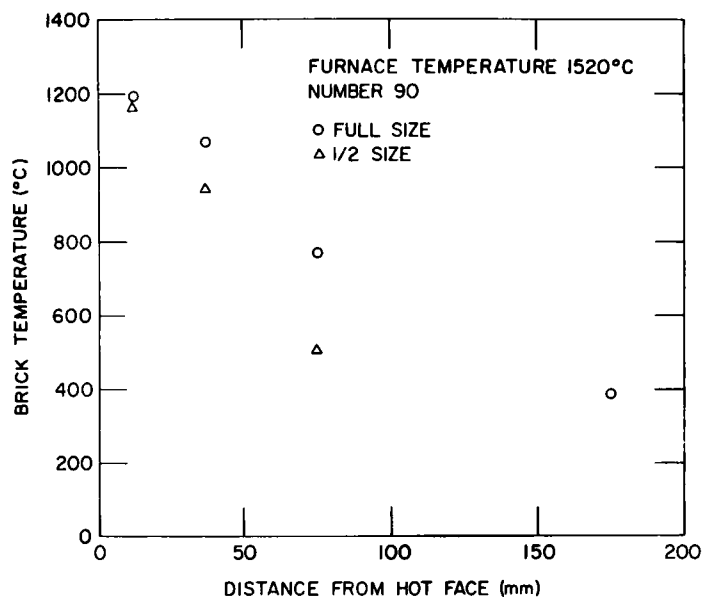
(a)
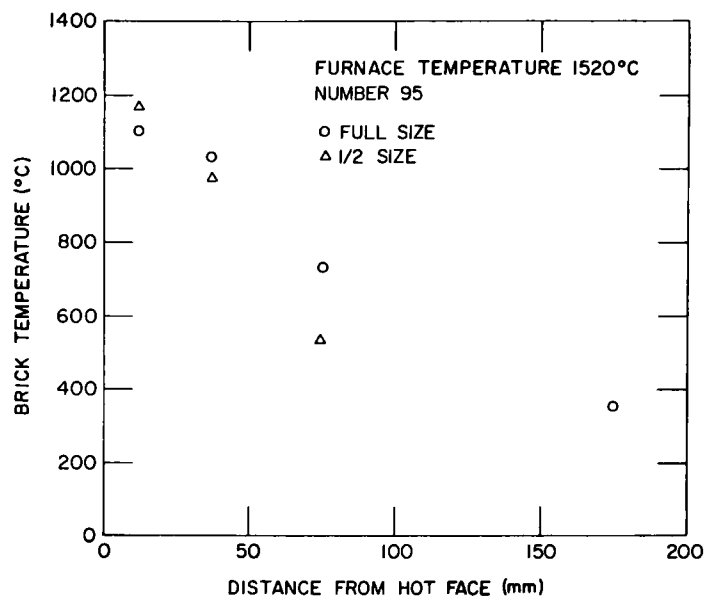
(b)
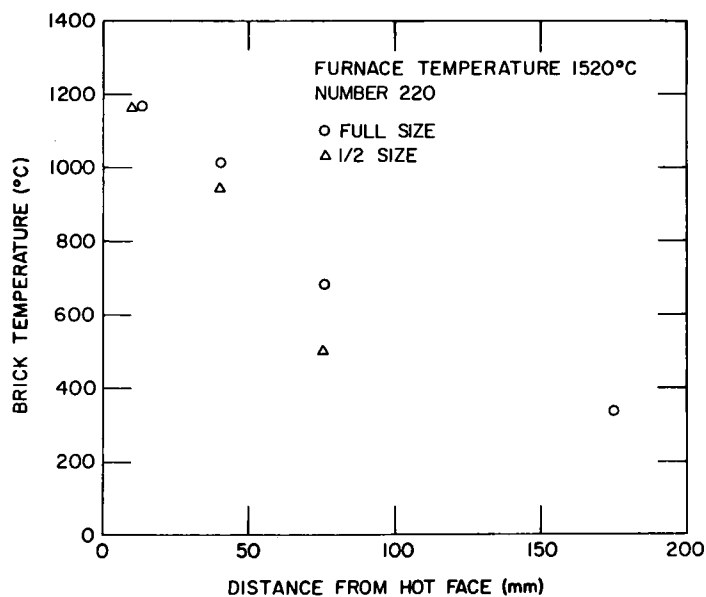
(c)

Fig. 7. Brick Temperature at Mid-height Versus Distance from Hot Face.
(a) Number 90, (b) Number 95, (c) Number 220, (d) Number 18, (e)
Number 260, and (f) Number 88. Furnace plenum temperature = 1520°C.
ANL Neg. Nos. 306-78-418, 306-78-419, 306-78-421, 306-78-423,
306-78-427, 306-78-430.

(d)

FURNACE TEMPERATURE 1520°C
NUMBER 18

○ FULL SIZE
△ 1/2 SIZE

BRICK TEMPERATURE (°C)

DISTANCE FROM HOT FACE (mm)

(e)

FURNACE TEMPERATURE 1520°C
NUMBER 260

○ FULL SIZE
△ 1/2 SIZE

BRICK TEMPERATURE (°C)

DISTANCE FROM HOT FACE (mm)

(f)

FURNACE TEMPERATURE 1520°C
NUMBER 88

○ FULL SIZE
△ 1/2 SIZE

BRICK TEMPERATURE (°C)

DISTANCE FROM HOT FACE (mm)

Fig. 7 (cont'd).

20
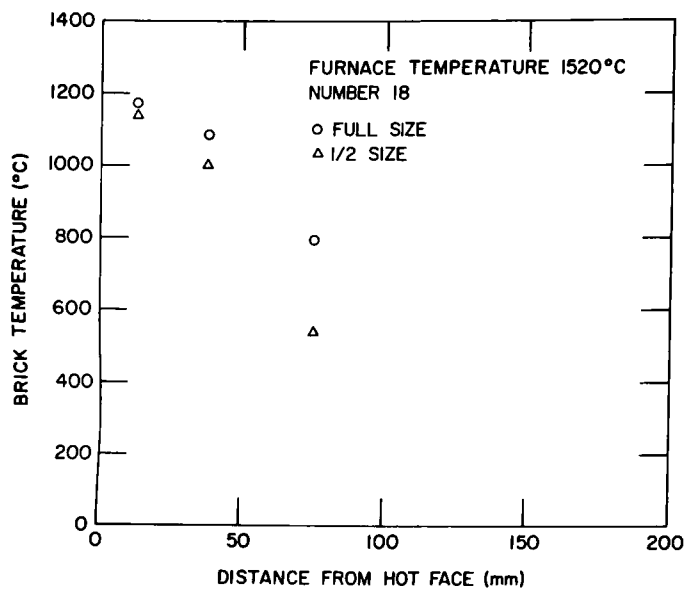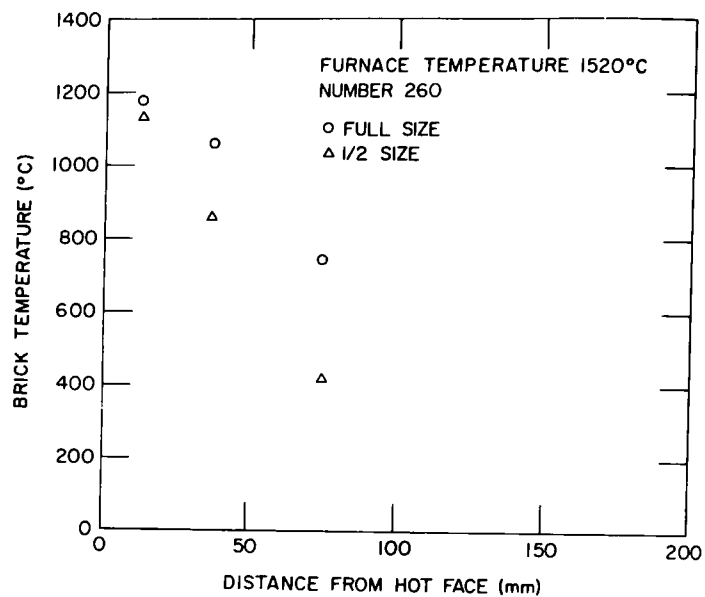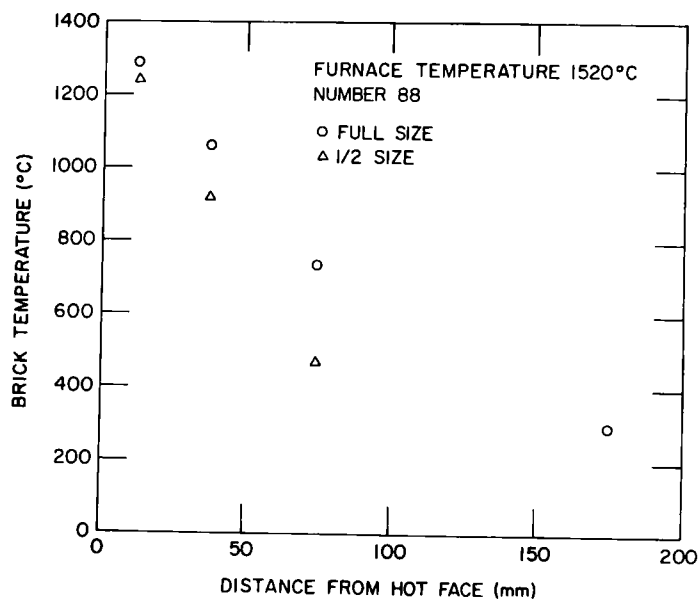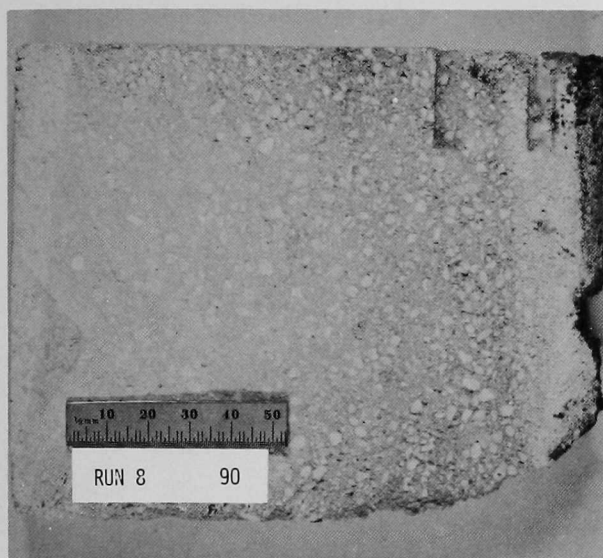
(a)
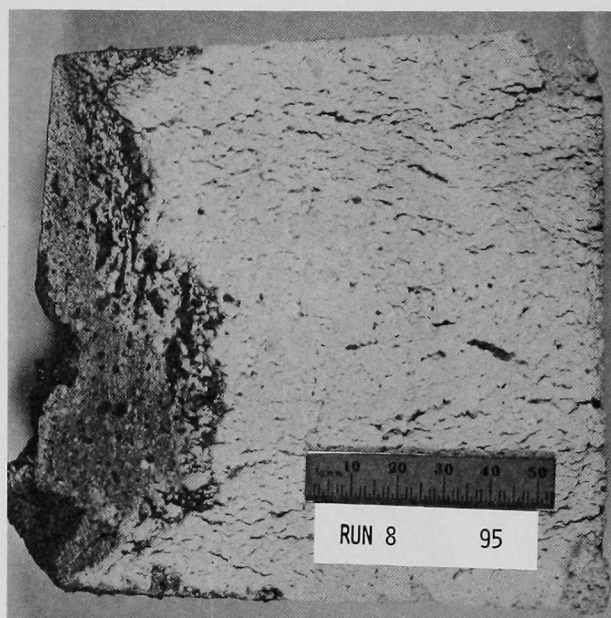
(b)

(c)
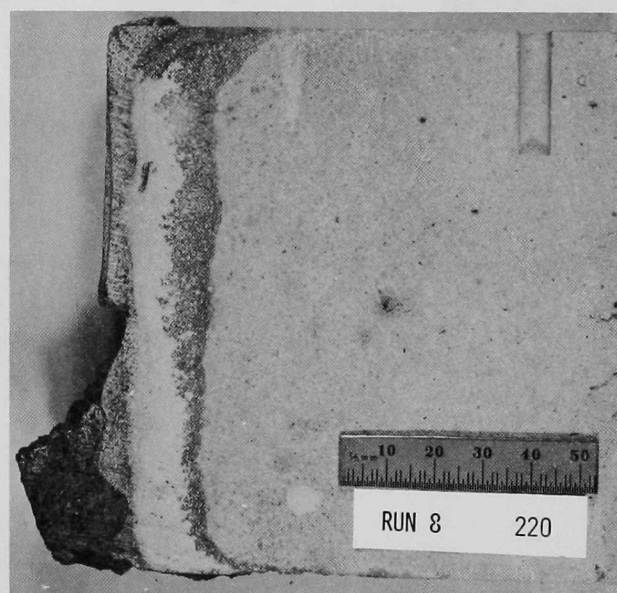
(d)

Fig. 8. Cut Sections of the Full-length Refractories Exposed to Slag Attack
in Test Run 8. (a) Number 90 (bottom slag-attack zone is broken off),
(b) Number 95, (c) Number 18 (bottom slag-attack zone is broken off),
and (d) Number 220. The vertical faces toward the center of the page
were exposed to two levels of slag.

21

(a)   (b)

Fig. 9. Cut Sections of Refractories Exposed to Slag Attack in Test Run 8.
(a) Number 260 and (b) Number 88. The left-hand vertical face was exposed.
Note that number 260 fractured ∿20 mm from the hot face (the cooler section
of the brick is not shown).
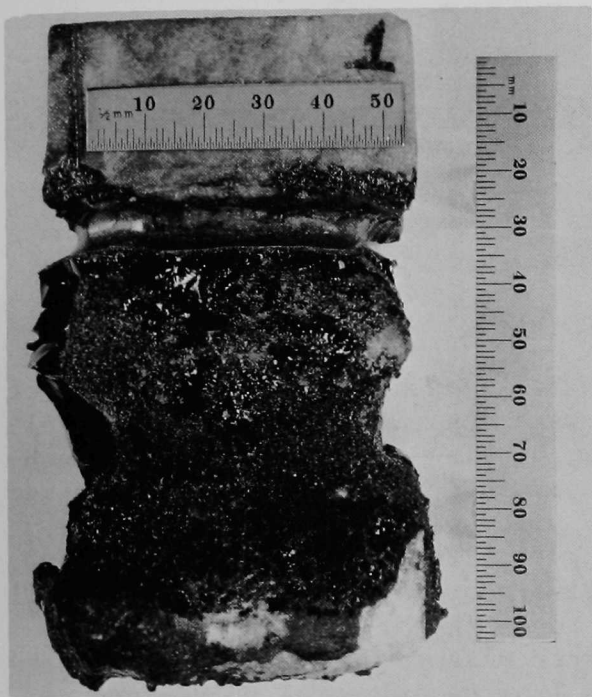
Fig. 10. Posttest Photograph of the Standard Specimen of Refractory Number 2 That Was Partially Immersed in the Slag Bath Without Water Cooling in Test Run 8. Note the two lines of slag attack extending around the specimen.

Fig. 11. Slag Outlet Block Obtained from Bi-Gas Pilot Plant, Homer City, PA.

Task B — Evaluation of Ceramic Coatings for Coal-conversion Plants
This task has been discontinued.

Task C — Application and Development of Nondestructive Evaluation Methods for Coal-conversion Processes *(W.A. Ellingson, K.J. Reimann W.J. Shack, and C.A. Youngdahl)*

1. **Erosive-wear Detection and Monitoring**

   a. **Metallic Transfer Lines**

   (1) Ultrasonic Studies - Pilot Plants. The periodic examinations of the HYGAS cyclone separator for erosive wear were continued with an additional ultrasonic survey during the reporting period; development of systems and techniques for ultrasonic monitoring of erosive wear in metallic lines and fittings has progressed. The separator from the HYGAS pilot plant was examined after 1092 hours of operation since the previous survey, i.e., 2842 hours since the first inspection. Additional results of erosive-wear monitoring of the Mark II instrumented 90°-bend elbow in the main coal feed line of the Synthane pilot plant were obtained during the quarter. Further measurements and analysis have refined the wall-thickness monitoring results from experimental pulse-echo instrumentation on the transfer lines and fittings of the Bi-Gas pilot plant. Efforts to improve the method of field attachment of ultrasonic waveguides to metallic lines are in progress, and noncontacting devices (EMATS) for determining wall thicknesses of high-temperature metallic lines are being investigated. Experiments are in progress to develop methods for the characterization of eroded metallic surfaces by analysis of reflected ultrasonic pulse echos.

   The HYGAS cyclone separator[2,4,5] was delievered to ANL on March 10, 1978, for examination of the progress of erosive wear. The stellite-lined inlet region and the 0.51-m-long Type 316 stainless steel internal cone were inspected by ultrasonic and x-ray techniques, and a molded impression of the erosion pattern at the solids outlet was made with rubber and measured microscopically.

   Wall thicknesses in the stellite-lined region of the cyclone were measured ultrasonically with a 5-MHz, 1/2-in. diameter Aerotech gamma transducer, Apiezon-L couplant, and Branson 303B pulser-receiver equipped with a time-analog gate. The measuring sites were the same as those previously monitored, defined by a matrix plate welded to the outer surface of the cyclone. Results of an azimuthal scan near the centerline of the matrix, which includes the matrix points of greatest thinning, are shown in Fig. 12. The curves were produced by smoothing in both the axial and azimuthal directions. An initial lack of concentricity as well as subsequent erosive wear produced the depression in the curve between points 5 and 9. The apparent wear in this zone since the first inspection, obtained by averaging these 3142-h points and subtracting the result from the average 300-h thickness measured at the same points in December, 1975, was 1.59 mm. The overall rate of wear (0.013 mm/day) was similar to that given in Ref. 2. It is estimated that 0.168 mm wear took place before the first inspection. If the nominal original thickness (3.175 mm) of the stellite lining was correct for the region defined by points 5-9, about 55% of the stellite has been eroded from that area.

An axial groove has developed at azimuthal position -2 of the cyclone, situated just past the end of the stellite-lined surface (Fig. 12). The material of the cyclone body is Type 304 stainless steel in the form of 8-in. schedule-160 pipe (original wall thickness 23 mm). Typically the inlet gas velocity is 15 m/s with a 1.8 kg/m^3 loading of 10-60-μm (about half) and 70-150-μm particles, according to IGT personnel. (Particle size was determined from samples recovered after discharge to slurry.) The groove was previously reported in Ref. 5 but has now become the site of minimum wall thickness in the inlet region. Inasmuch as the cyclone operates at 6.9 MPa and 316°C, subsequent monitoring of this zone may become important in terms of safety as well as material economics.

A substantial amount of erosion of the 0.51-m-long cone structure within the cyclone has occurred. The location of the Type 316 stainless steel cone in the assembly is shown in Fig. 13. The erosion process has produced a large-scale sawtooth ridge pattern on the inner surface of the long cone, with the ridges running generally in the axial direction and spaced 20-25° apart azimuthally. Ridge edges were irregular, as shown in an X-ray view exposed through the entire assembly and reproduced in Fig. 14. A schematic sketch of an end view of the sawtooth structure is shown in Fig. 15 together with thickness data based on a small number of determinations made ultrasonically with a 25-MHz Aerotech 1/4-in.-diameter alpha transducer fitted with a delay line, attached to a probe, and inserted to a depth of 0.5 m into the cyclone from the solids outlet flange. The limited data suggest that as much as 40% of the original 6.35-mm thickness of the cone has been eroded away.

Considerable erosion of a stainless steel solids outlet liner that had been added to the cyclone since the last examination was evident, and a molded replica was made of the erosion pattern. A photo of the replica is given in Fig. 16. A longitudinal sawtooth pattern similar to that seen in the long cone section (Fig. 15) was present, superimposed on the helical grooves. The peak-to-valley distances on the replica were typically ∿ 1 mm, with some as large as 2.5 mm.

The foregoing results were reported to responsible personnel at the HYGAS plant. They have tentatively concluded that operation of the cyclone can be resumed but preparation of a replacement cyclone should be considered.

Further results of erosive-wear monitoring of the Mark II instrumented elbow[1] in the main coal feed line of the Synthane pilot plant were obtained during the reporting period. The 0.3-m radius 90°-bend elbow, made of 1-in. schedule-80 Type 304 stainless steel pipe, was installed in the line in August, 1977, and used until February, 1978, to convey Illinois #6 coal into the process system. Wall thicknesses at sites on the extrados of the elbow were monitored ultrasonically from the control room by means of the ANL erosive-wear monitoring system described previously[1], operated in the manual mode. The scanner was advanced manually to allow time for adjustments of gain and timing controls of the Branson 303B pulser-receiver and time-analog gate in accordance with previous photographs of the waveforms and control settings. Such adjustments are needed because of variations in signal attenuation and noise generation at welds used to attach the ultrasonic waveguides to the elbow. (Effort to improve the method of attachment is noted in a later paragraph.) The same transducer and standards

used at the times of installation and subsequent measurements[1] were used to calibrate the time-analog gate during the most recent survey on January 28, 1978. Under these conditions, assuming that the properties of the material and reflecting surfaces are not significantly changed with time, an error limit of 0.13 mm is considered applicable to each field measurement of shoulder-to-inner-surface distance. The results from the Mark II elbow are shown in Table VIII. The erosive conditions reported by DOE personnel at the plant are described in footnotes to the Table. The apparent wear was very small. If the error limit is fully applied, the total wear was between 0 and 0.61 mm (0 to 24 mils). To accommodate a process change at the Synthane plant, the elbow was removed from service in February and returned to ANL. Other applications are being considered to provide additional in-plant operating experience as the monitoring system is more fully automated.

Further ultrasonic measurements and analysis have refined the wall-thickness monitoring results[1] from the carbon steel lines and fittings on the main coal feed line at the Bi-Gas pilot plant. Additionally, results have been obtained from the monitoring installation at the stainless steel blocked tee in the product off-gas line on the eighth floor of the plant. The most recent ultrasonic measurements of wall thickness of these components were obtained during a plant visit on March 29, 1978. At the same time the several reference blocks that have been used for machine calibration were checked magnetically for material verification and by micrometer for dimensional accuracy. It was found that one reference block that may have been used previously for carbon steel calibration was nonmagnetic and thus not of carbon steel. When calibration was done with other standards verified as noted, and distances from waveguide shoulder to component inner surface were determined ultrasonically, the results shown in Tables IX and X were obtained. These values, considered with some of the corrected previous results and the nominal starting dimensions, indicate that little erosive wear has been experienced at the various measuring sites. The references in Tables IX and X to $\lambda/2$ correction are discussed below. For perspective it is pointed out that the refinement of results is negligible from the standpoint of operating safety but significant in terms of erosive wear and material economics.

The half-wavelength ($\lambda/2$) corrections of Tables IX and X were introduced because of the fine structure of the waveforms of the ultrasonic echos. The echo from each reflecting site consists of a brief train of waves of differing amplitudes, which is rectified and displayed on the receiver oscilloscope; the time-analog gate is triggered by the oscilloscope signal voltages. Ordinarily the timing is adjusted to show the waveguide shoulder and pipe inner-surface reflections in the same display frame, and the wave train of each reflection site appears as a discrete entity in which the half-waves are not clearly resolved. It is important to standardize the number of half-waves of each echo that are included in calibration and measurement, because, for example, each 5-MHz half-wave interval is the equivalent at room temperature of 0.58 mm (23 mils) of carbon steel (annealed).[6] In practice, it is often unnecessary to consider the fine structure of each echo because calibration standards are used that are of similar geometry to that of the specimen. However, for measurements via waveguides that are welded to the specimen by the present technique, the amount of acoustic scattering from the weld zone varies greatly from waveguide to waveguide, so that the

amplitude of the waveguide-shoulder echo relative to that of the inner-surface echo differs greatly from site to site. Thus, as machine gain is adjusted to compensate for scattering, the measurements can be affected by the inadvertent inclusion of smaller-amplitude half-waves that typically precede the half-waves of largest amplitude within a given wave train with the apparatus presently used. Under certain other conditions, e.g., when the shoulder echo is relatively small, one or more half-wave intervals can be lost. Identification of corresponding half-waves in the wave train of each of the shoulder and inner-wall echos, when feasible, provides a basis for avoidance of or compensation for the half-wave errors. This identification is made through inspection of the echo patterns at a sweep rate high enough to resolve the half-waves and with gain adjustments as needed to compare the patterns. When patterns are changed by the curvature or roughness of a reflecting surface, such identification is doubtful. The overall problem would be reduced by elimination of small-amplitude leading waves; this appears to be feasible with a different type of transducer and is being studied. Improved methods for attachment of waveguides to specimens, discussed in a later paragraph, may also be helpful. In addition, a method of rationally accounting for patterns of echos reflected from surfaces roughened by erosion is under development (see below). At present, the problem is being managed by photographing the oscilloscope displays to provide references for subsequent measurements and by half-wave corrections, when feasible, to specify the correct distances at any time. Table IX shows the values measured by the time-analog gate (TAG) and tentatively corrected by the number of $\lambda/2$ intervals judged appropriate from inspection of echo wave trains.

Table X gives results from the waveguide sites at the Type 304 stainless steel blocked tee in the product off-gas line on the eighth floor of the Bi-Gas plant. The agreement with past data is within 0.025 mm (1 mil) in several instances. The small apparent changes shown may be caused in part by a lack of explicit $\lambda/2$ information for the 9/77 data. It is concluded that the erosive wear was negligibly small.

The automatic scanning mode of the erosive-wear monitoring system will be tested during plant operating periods in the next quarter, following repairs to some of the connecting cables of the system which were damaged after a burner rupture in February. The anticipated effect of specimen (pipe) temperature on indicated thickness will be verified, and the effects of any physical and electrical interference from the plant will be observed. The effectiveness of measures designed to improve the accuracy of wear measurements, described above, will be tested. Several measuring sites are not suitable for automatic scanning and will not be included in these tests. Also, the effect of the temperature of erosive-wear detection-system components on signal amplitude and measurement accuracy will be measured in the laboratory.

An improved method of waveguide attachment to specimens in the field is being sought to reduce the effect on the measuring process of the structural details at the attachment site. Solid acoustic contacts are desired that will not deteriorate with time at elevated temperature and that are substantially free of voids, inclusions, or other phases which produce significant and variable amounts of ultrasonic scattering and spurious pulses from site to site. A minimal effect of attachment on the integrity of the specimen metal is another requirement. Most of the attachment welds of waveguides in the existing field instal-

lations are satisfactory for ultrasonic thickness determinations performed manually by an operator who can make the necessary compensating adjustments of the instrument from point to point. The goal of comprehensive automatic operation of the scanning system, continous or intermittent, requires that such readjustments be unnecessary or be made automatically. It is believed that automatic compensation will not be needed if the method of waveguide attachment is improved.

A stud-welding firm is preparing specimens by the same method used in the existing field installations, using well-characterized materials and best-effort procedures to determine whether the method or the field implementation needs improvement for this application. If changes in the method are found to be necessary, the use of inert gas cover and/or a modified profile of waveguide tips is planned. Concurrently, experiments with stud attachment by percussion welding are in progress at ANL. The feasibility of friction welding of studs in the field is being considered, as are percussion brazing and a mechanical method of attachment that would use gold as a couplant.

Characterization of the roughness of reflecting surfaces by ultrasonic echo analysis is under study, both to enhance the capability for nondestructive evaluation and to provide a rational basis for improving accuracy when thickness measurements by pulse-echo technique involve an eroded reflecting surface. One possible approach employs a relatively broad-band transducer driven by pulsed sine waves at various frequencies, one at a time, with observation of amplitude and phase changes within the reflected echos from smooth and roughened surfaces. A 3.5-MHz "special alpha" transducer has been fabricated for this purpose by KB Aerotech; its sensitivity to off-resonant frequencies is not inhibited by the customary backing material on the crystal. (It is noted that this transducer does not produce small-amplitude, leading half-waves and therefore poses less risk of $\lambda/2$ errors as previously discussed.) Preliminary tests with this approach are promising. However, another technique has been more extensively explored during the quarter and is described in the following subsection.

TABLE VIII

Changes in Distance from Waveguide Shoulder to Elbow Inner Surface
at Sites on Synthane Mark II Instrumented Elbow[a]

Waveguide Number[b]	Change, 8/26/77 to 11/29/77		Change, 8/26/77 to 1/28/78	
	mils	mm	mils	mm
1	–[c]	–	–	–
2	-2	-0.051	-8.5	-0.216
3	(noisy)	–	–	–
4	-4	-0.102	-13.6	-0.345
5	(noisy)	–	–	–
6	-3	-0.076	-7.5	-0.191
7	-2	-0.051	-6.3	-0.16
8	-5	-0.127	-9.5	-0.241
9	-2	-0.051	-7.6	-0.193
10	±0	±0	-4.8	-0.122
11	-2	-0.051	(uncoupled)	–

[a]Installed in August, 1977. Material: Type 304 stainless steel. Erosive conditions: 8/26/77 to 11/29/77, 41256 kg (45.5 tons) (380 g/s max) of Illinois #6 coal conveyed by CO_2 at 3-11 m/s and 120°C mixed temperature; 11/29/77 to 1/28/78, an additional 91593 kg (101 tons) (380 g/s max) conveyed by CO_2 and steam at 11-15 m/s and 120-260°C mixed temperature.

[b]Numbers increase in direction of flow: No. 1 begins bend from horizontal to vertical flow.

[c]No. 1 was damaged during operations in the area, as was No. 11 between 11/77 and 1/78.

TABLE IX

Ultrasonically Measured Distance from Waveguide Shoulder to Inner Wall of
Carbon Steel Components in BI-GAS Main Coal Feed Line[a]

Waveguide Number	Sh-BW 3/29/78		$\lambda/2$ correction[b]	Waveguide Number	Sh-BW 3/29/78		$\lambda/2$ correction[b]
	in.	mm			in.	mm	
11	1.052	26.72	2	21	(open)	–	–
12	1.060	26.92	2	22	1.057	26.85	1
13	1.121	28.47	2	23	1.117	28.37	1
14	1.116	28.35	2	24	1.122	28.50	1
15	(open)	–	–	25	1.282	32.56	1
16	(noisy)	–	–	26	1.612	40.94	1
17	1.083	27.51	0	27	1.610	40.89	1
18[c]	(1.158)	(29.41)	1	28	1.610	40.89	1
19	1.076	27.33	2	29	1.616	41.05	1
20	1.051	26.70	0	30	1.620	41.15	1
				31	1.625	41.28	1

[a]The pulser-receiver was located at the reed relay box associated with each set of waveguides: Nos. 11-15, lower elbow, 6th floor; Nos. 16-20, upper elbow, 10th floor; and Nos. 21-31, upper tee, served from the 10th floor. Waveguides are numbered in the direction of flow except at the upper tee, where the order is reversed. Shoulder-to-outer-surface distance for most sites is ∿6.35 mm (1/4 in.)

[b]Number of acoustic half-wavelengths added to the value shown by the time-analog gate to produce the Sh-BW dimension listed. The basis for the correction is explained in the text.

[c]Values for site No. 18, a noisy site, are less certain.

TABLE X

Ultrasonically Measured Distances from Waveguide Shoulder to Inner Wall
of Stainless Steel Blocked Tee in BI-GAS Product Off-gas Line

Waveguide Number	Sh-BW[a]	$\lambda/2$ correction[b]	Corrected TAG value	Corrected Value x 0.975[c]	Adjusted Value for 9/77[d]	Change, 9/77 to 3/78	
						in.	mm
1	1.343		1.343	1.309	1.308[e]	0.001	0.025
2	1.339	+0.016	1.355	1.321	1.321	0.000	0
3	1.340		1.340	1.307	1.305	0.002	0.051
4	1.350		1.350	1.316	1.316	0.000	0
5	1.343		1.343	1.309	1.296	0.013	0.330
6	1.337		1.337	1.304	1.291	0.013	0.330
7	1.213	-0.016	1.197	1.167	1.142	0.025	0.635
8	1.162	-0.016	1.146	1.117	1.119	-0.002	-0.051
9	1.162	-0.016	1.146	1.117	1.117	0.000	0
10	1.173	-0.016	1.157	1.128	1.108	0.020	0.508

[a]Distance from waveguide shoulder to inner wall of Type 304 stainless steel tee or pipe, as measured by time-analog gate (TAG) calibrated in inches of carbon steel. A 3-point calibration had been used with standards verified magnetically and dimensionally, and with compensation for verified half-wave shift as required during calibration. The pulser-receiver was located at the site of the subject tee.

[b]Half-wave shift correction needed during measurement, determined by inspection of echos at high sweep rates on Branson 303B oscilloscope. Frequency is 7.5 MHz for transducers at this tee.

[c]Measured correction factor for several Type 304 SS standards; converts carbon steel calibration to Type 304 SS calibration.

[d]From data of 9/8/77 taken with a stainless steel-calibrated pulser-receiver at the tee site, corrected for use of a 19.456-mm (0.766-in.) standard marked ".741" and for $\lambda/2$ as indicated.

[e]includes $\lambda/2$ addition.
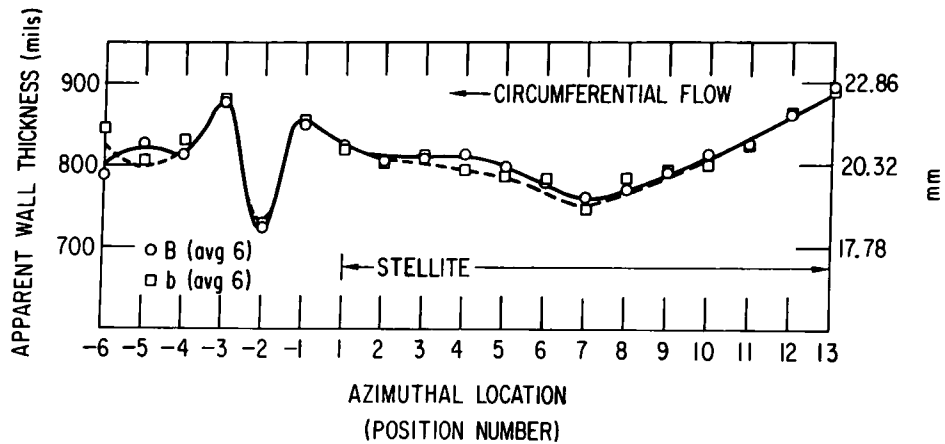
Fig. 12. HYGAS Cyclone Separator after 3142 Operating Hours. Wall thickness at matrix rows B and b versus azimuthal location, 3/78. Neg. No. MSD 65256
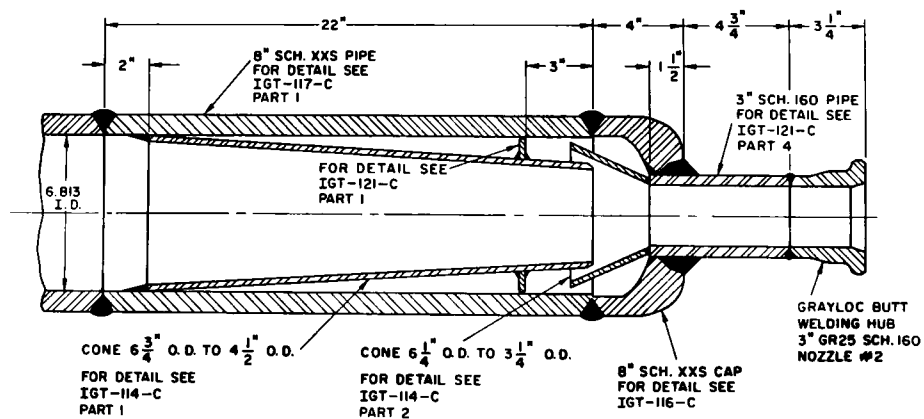
Fig. 13. Section of HYGAS Cyclone Separator Showing Location of 0.51-m-long Cone. Solids outlet neck is at right. Drawing provided by Institute of Gas Technology. Neg. No. ANL-306-78-561

10 mm ON X-RAY FILM
AXIAL DIRECTION
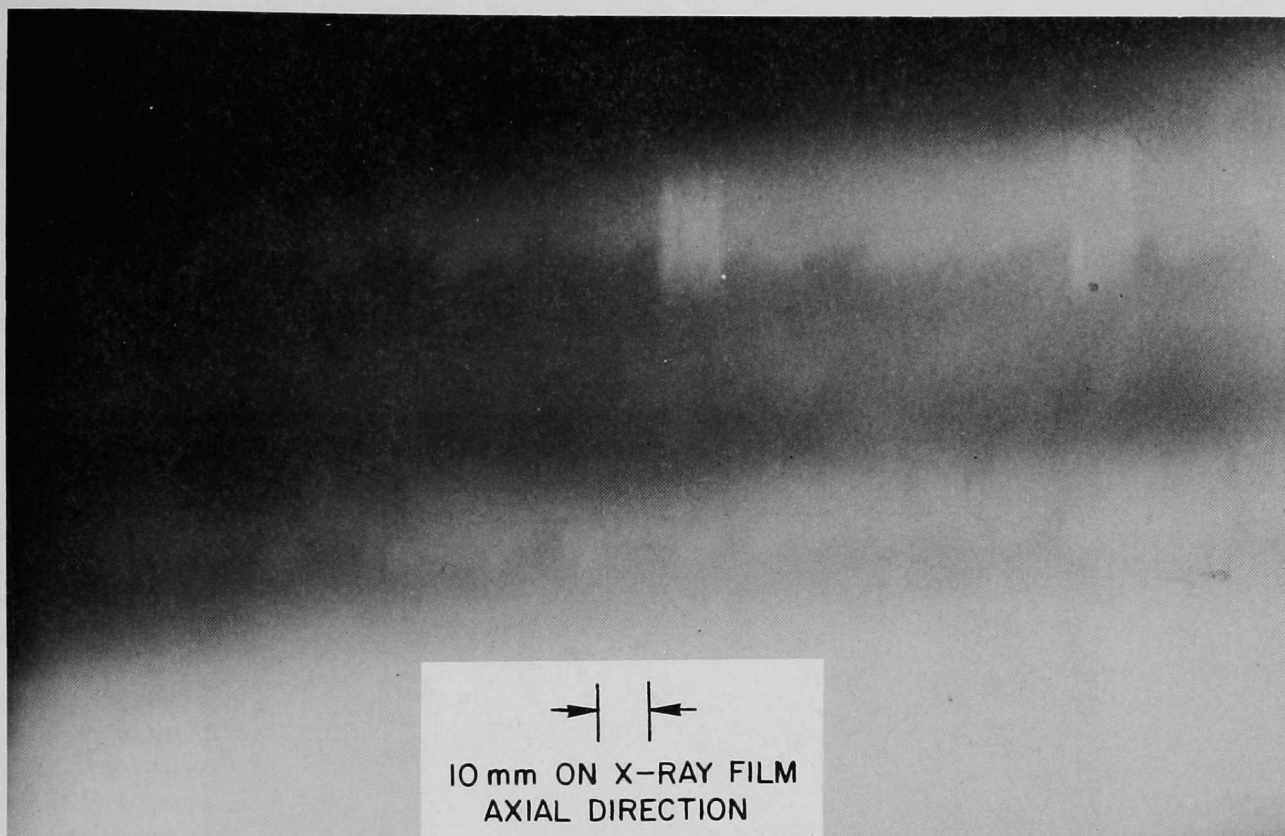
Fig. 14. Erosion Pattern of Longitudinal Sawtooth Ridges in 0.51-m-long Cone of Type 316 Stainless Steel Within Body of HYGAS Cyclone Separator. X-ray view exposed through the entire assembly. Neg. No. ANL-306-78-463

FLOW

5.84 mm

4.88 mm
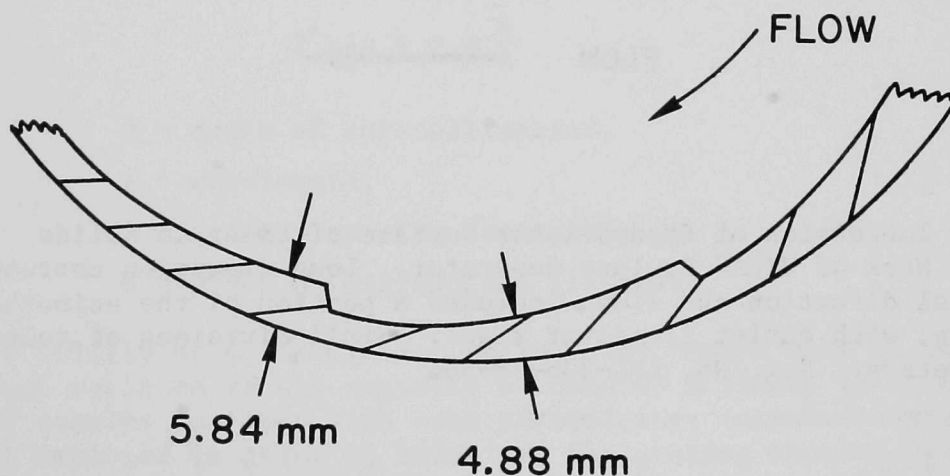
Fig. 15. Schematic of End View of Long Cone Within Body of HYGAS Cyclone Separator, Showing Sawtooth Erosion Pattern and Dimensions at Sites 0.5 m from Solids Outlet Flange. Original thickness of the cone was 6.35 mm. Neg. No. ANL-306-78-537
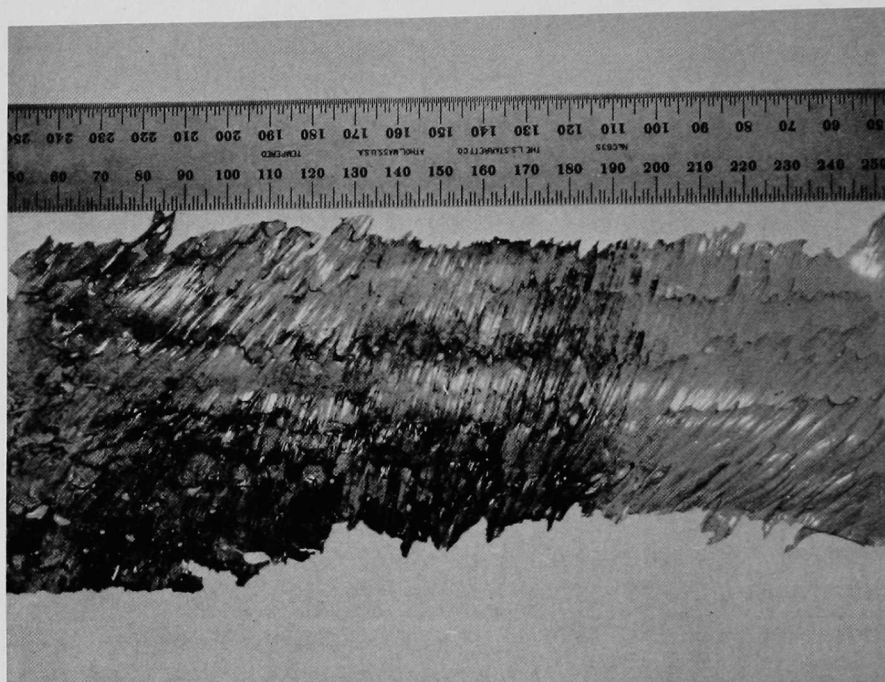
FLOW ⟶

Fig. 16. Rubber Impression of Eroded Inner Surface of Liner in Solids
Outlet Neck of HYGAS Cyclone Separator. Long dimension corresponds
to axial direction and width includes a portion of the azimuthal
surface, with outlet flange at right. Small divisions of ruler are
millimeters. Neg. No. ANL-306-78-566

(2)   Ultrasonic Studies - Scattering of Acoustic Waves from Rough Surfaces.   Measurement of erosion rates in coal-conversion plant components by means of noninvasive ultrasonic techniques is an important technique for optimizing component design and material selection. The accuracy of the ultrasonic measurements will be strongly dependent on the backscattering properties of the reflecting surface, e.g. the eroded inside surface of a tube. Moreover, in severely gouged surfaces a knowledge of the gouge depth is imperative, since the minimum wall thickness at the bottom of the groove will determine the lifetime of the component. The present study is aimed at identifying and quantifying surface-roughness effects on ultrasonic wall-thickness measurements and at establishing a viable technique to measure the effective value of surface roughness.

Scattering of acoustic and electromagnetic waves from rough surfaces has aroused the interest of investigators during the last two decades mainly because of its applicability to topographical terrain mapping and ultrasonic visualization of biological tissues. Eckart[7] developed a theory of ultrasonic scattering from stochastic surfaces such as the surface of the sea. Horton et al.[8,9] reviewed Eckart's theory, examined some surfaces using various covariance functions, and performed model studies. Other investigators[10-12] elaborated on the theory and measured the scattering of acoustic waves. More recently, deBilly and coworkers[13-15] performed backscattering measurements of rough surfaces under conditions closely related to nondestructive testing. Using angular dependence of the backscattered acoustic energy and "signature" analysis of back scattered acoustic signals from periodically rough surfaces, they compared their experimental results with theory, which is still limited to particular cases, and with various approximations or models. Their experimental findings showed that the scattering of ultrasonic waves at a given frequency becomes more diffuse if the surface roughness increases and the same effect is observed at a given roughness if the ultrasonic frequency increases. Surfaces with spatial periodicity exhibit peaks in their spectral "signature", which can be correlated with the grating spacing constant by the autocollimation equation

$$2 \sin \theta = m \frac{\lambda}{\Lambda} \tag{1}$$

where θ = angle of autocollimation,

               λ = wavelength,

               Λ = grating spacing constant,

and
               m = order of diffraction (integer).

The results of deBilly et al. show that calibration curves must be established for random rough surfaces if the rugosity of unknown surfaces is to be determined. In the case of complex surfaces with some periodicity, computer-averaging techniques must be employed in order to bring out the grating spacing peaks. In their discussion of the experimental results, deBilly et al. point out that most of the theoretical calculations were not applicable to their findings. One reason was the placement of the rough surface in the near field of the transducer. Another reason was the application of a pulsed transmission, which causes repartitioning of the ultrasonic field. A third reason is the large variation of

Beckman's roughness parameter in the experimental results. This parameter does not take into account the autocorrelation distance L, and in some experimental conditions the inequality L $\gg \lambda$ is not satisfied.

Even though the investigations of deBilly and coworkers are applicable to nondestructive testing, the conditions encountered in ultrasonic measurement of erosion differ in several important respects from the experimental conditions they employed. First of all, in coal-conversion components the scattering surface is a metal-gas or metal-slurry interface instead of a water-metal boundary. Secondly, the energy will often travel through a waveguide in a fixed position so that no angular scattering dependence can be measured. Thirdly, the scattering surface will often be a curved surface and not a flat interface. Finally, the surface will sometimes exhibit very deep gouging, which reduces the accuracy of effective-roughness measurements. By dealing with these four problems, the present scattering study will lead to the development of an adequate model and establish techniques to measure rugosity and periodicity of rough surfaces. Ultimately this will lead to improvements in the accuracy of wall-erosion measurement on actual, in-situ components.

Measurements of the angular dependence of scattered energy from periodically roughened flat samples, using longitudinal and shear-wave transducers of different center frequency and bandwidth, will be compared with results obtained by deBilly et al. This will allow evaluation of the applicability of their model. At the same time, ultrasonic spectroscopy will be used to establish the feasibility of determining rugosity and periodicity of rough surface by this type of signature analysis. Wall-thickness measurements of these rough samples with conventional equipment, and comparison of results with rugosity measurements, will establish the needed correction factor for such measurements. The effort will then be expanded to include randomly roughened samples, curved samples, and the effect of waveguides.

Six specimens were fabricated as shown in Fig. 17 to evaluate the effects of rough surfaces as encountered in eroded coal-gasification components (neck of cyclone separator). Specimens I-III were made with sharp groove corners, while the groove corners in specimens IV-VI were rounded. The groove dimensions are listed in Table XI.

Some preliminary ultrasonic spectroscopy experiments were performed on specimen II, using a 0.5-in.-OD, 5-MHz center-frequency transducer. Figure 18 shows the frequency spectrum of the echo obtained from the smooth part of specimen II; the spectrum of an echo from the medium (sharp-cornered) grooves is exhibited in Fig. 19. Interference from the surface structure at discrete frequencies is very obvious. These interference patterns have their origin in phase shifts caused by path-length differences and in lobe structures of directivity patterns.

A 180° phase shift will occur between points where the path-length difference equals half the wavelength. For the structure under consideration, this will occur for frequencies

$$f_n = \frac{2n - 1}{2} \frac{c}{h} \qquad n = 1, 2, \ldots \qquad (2)$$

and

$$f_n = \frac{2n - 1}{2} \frac{c}{d} \qquad (3)$$

where

c = velocity of sound

and

h and d are as defined in Fig. 17.

Interference by directivity patterns can have many causes, taking into account different surface-structure features. For example, area directivity will occur for frequencies

$$f_n = \frac{nc}{a \sin \theta} \qquad n = 1, 2, \ldots; \qquad (4)$$

and dipole radiation (sharp corners) will occur for frequencies

$$f_n = n \frac{N - 1}{N} \frac{c}{a \sin \theta} \qquad n = 1, 2, \ldots \qquad (5)$$

where

a = pole spacing or flat-surface width (for a 90° included

groove angle, $a = d \sqrt{2}$)

θ = angle between sound beam and surface normal.

Interference frequencies were calculated by means of these equations for the medium grooves of specimen II (sharp-cornered), using the measured sound-velocity value of $c = 5.7 \times 10^3$ m/sec. They are listed in Table XII along with the measured interference frequencies. The agreement between measured and calculated frequencies is quite good, considering that nonlinearity exists in the horizontal frequency scale of Figs. 18 and 19. Moreover, interaction between directivity patterns of two adjacent reflecting surfaces will modify the overall response (similar to dipole and N-tuple pole directivity differences).

A more systematic evaluation of spectral responses will be pursued during the next reporting period.

TABLE XI. Dimensions of Grooves in Test-block Specimens

Specimen	Sharp-Cornered Grooves	Groove Dimensions, mm		Specimen	Round-Cornered Grooves	Groove Dimensions, mm	
		d	h			d	h
I	Shallow	1.59	0.51	IV	Shallow	1.59	0.41
	Medium	1.59	0.79		Medium	1.59	0.64
	Deep	1.59	1.24		Deep	1.59	0.94
II	Shallow	3.18	0.97	V	Shallow	3.18	0.74
	Medium	3.18	1.63		Medium	3.18	1.22
	Deep	3.18	2.59		Deep	3.18	1.78
III	Shallow	4.76	1.32	VI	Shallow	4.76	1.02
	Medium	4.76	2.29		Medium	4.76	1.68
	Deep	4.76	3.84		Deep	4.76	2.46

TABLE XII. Measured and Calculated Interference Frequencies for Specimen II

Measured Frequency, MHz	Calculated Frequency, MHz	Inteference Model
1.75	1.8	Dipole, n = 1
2.95	2.7	Phase Shift by h and d, n = 2
2.95	3.2	N-tuple pole, n = 1 and N = 8
3.7	3.6	Area directivity, n = 1
4.2, 4.9	4.5	Phase shift by h and d, n = 3
5.6	5.4	Dipole, n = 2
6.1	6.3	N-tupple pole, n = 2 and phase shift, n = 4
7.5	7.2	Area directivity, n = 2
8.2	8.1	Phase shift by h and d, n = 5

A = 16 mm, B = 28.6 mm, C = 31.75 mm, D = 3.18 mm

1.59 mm
4.76 mm

12.6 mm

60° 90° 120°
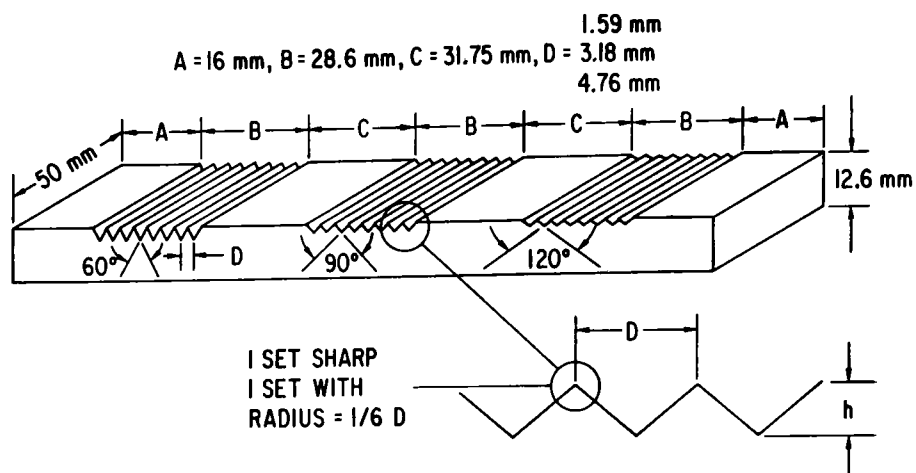
I SET SHARP
I SET WITH
RADIUS = 1/6 D

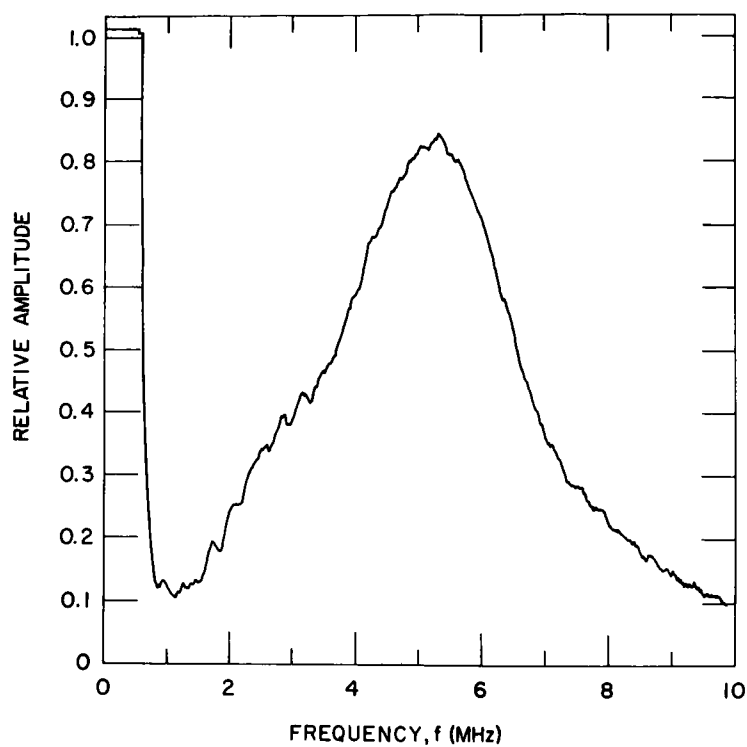Fig. 17. Schematic of Test-block Specimen
Neg. No. ANL – 306-78-486

Fig. 18. Spectral Response From Smooth Surface of Specimen II
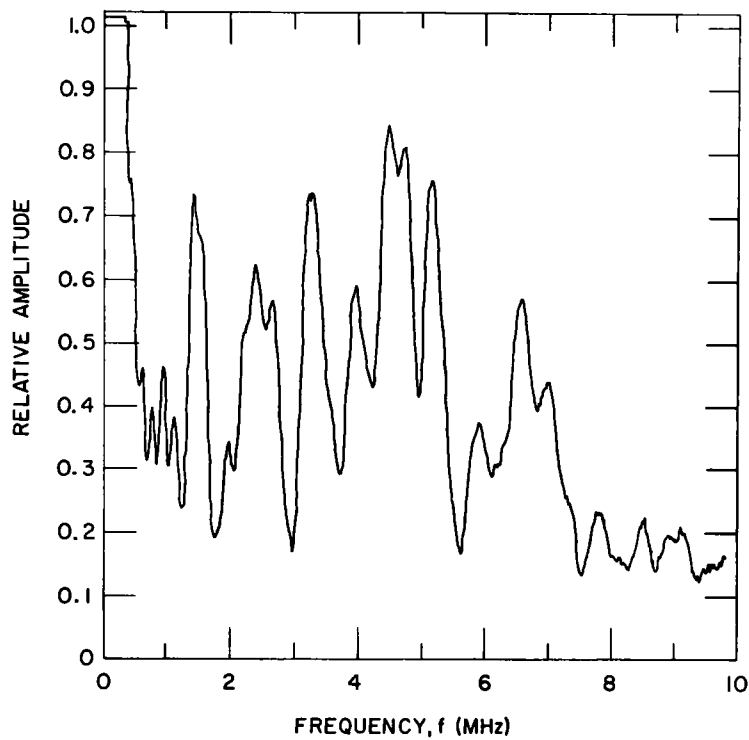Neg. No. ANL-306-78-519

40

Fig. 19. Spectral Response From Rough Surface (Medium Grooves)
of Specimen II. Neg. No. ANL-306-78-517

2. Refractory Installation Practices

a. Detection of Thermally Induced Acoustics from Refractory Materials

Work has continued during the present quarter on evaluation of the use of acoustic emission as a means to control the firing schedule of thick castable refractory concrete linings of the type envisioned for use in the main process vessels in coal-conversion (gasification, liquefaction) and fluidized-bed (atmospheric and pressurized) plants. Previous reports[1] have discussed the acoustic-emission parameters, i.e. ringdown count and count rate, which have been analyzed for application to this type of structure. Most recently, however, amplitude distribution has been of particular interest because of its potential ability to predict a priori the occurrence of large damaging events.

During this quarter, two high-density Castolast-G panels, 15 cm thick, were fired using electrical-resistance heating elements as the heat source. Panel I was 91 cm long x 61 cm wide; Panel II was smaller (36 x 36 cm) because the available furnace was smaller. The panels were cast with a water content of 11% and were cured in an environment of $\sim$ 95% relative humidity by enclosing each casting in a large polyethylene bag for three days. They were then allowed to cure in air for three more days prior to firing. Each panel had a 2.5-cm-thick steel-plate backing. Four conventional "Y"-type refractory hangers were used to keep the refractory and steel plate from separating. On each of three of the hangers, Type K thermocouples were placed at 2.5-cm intervals throughout the thickness. This provided a means of establishing the thermal gradient through the refractory at steady state as well as the dynamic temperature during heating and cooling. In addition, the thermocouple data yields the rate at which the compressive/tensile interface moves back from the hot face.

Two acoustic-emission waveguides of quartz, 23 cm long with a 2.5-cm OD, were coupled to each steel plate (see Fig. 20), one for a 175-kHz resonant transducer and one for a broadband transducer. Both transducers were in an acoustic-emission data-acquisition system which yielded total ringdown counts, total event counts, and amplitude distribution. A block diagram of the system is shown in Fig. 21. The test panels were acoustically isolated from the furnace by means of high-temperature rubber seals.

The panels were fired using an automatic temperature-control system. The intent was to fire panel I at a high heating rate to induce large-crack formation, so that acoustic-emission parameters for this process could be identified. However, problems with the heating elements caused the heating rate to be very low rather than very high as desired. The maximum heating rate was about 75°C/h (150°F/h). The actual temperature history of the hot-face thermocouple is shown in Fig. 22. For panel II, a maximum heating rate of 500°C/h was achieved, but only for a brief time (see Fig. 23). The typical rate was 300°C/h. Panel II reached 1000°C in 14 h for an average rate of 71°C/h, while panel I required 44 h (about three times longer) to reach 1000°C for an average rate of 25°C/h.

Figures 24a and 24b show the count rate, dn/dt, for panel I as a function of time, obtained from the 175-kHz and broadband transducer, respectively. Figures 25a and 25b show the count-rate data for panel II as a function of time,

obtained from the 175-kHz and broadband transducers, respectively. The sensitivity of the 175-kHz transducer is 30 db greater than that of the broadband transducer; however, the data obtained with the two transducers are qualitatively similar. The difference between the relative heating rates of panels I and II is reflected in the count-rate data. The value of the count rate for the slowly heated panel (panel I) fell to less than 20,000 counts/h during the apparent critical heating region up to 500°C (Fig. 24), whereas for panel II, most of the count-rate values during heating in the apparent critical region were above 30,000 counts/h and several peaks were in the 70,000-100,000 counts/h range (Fig. 25a). When each panel reached 1000°C, it was allowed to cool by turning the furnace off, yielding an exponential temperature decay. Panel I showed marked increase in acoustic activity during cooling, as evidenced by the count-rate values. However, panel II, which had significant acoustic activity on heatup, showed little activity even when cooling at a fast rate. This suggests that the crack damage on panel I occurred during cooling while that on panel II occurred during the fast heating.

Additional evidence of acoustic-activity difference between the panels is provided by a comparison of the amplitude distributions. Amplitude-distribution data were taken at intervals of nominally two to four hours, as this appeared to be an adequate time interval for accumulation of activity. Figures 26 and 27 show the characteristic slope, b, for panels I and II, respectively, obtained as a function of the heating and cooling schedule. What is perhaps significant is the absolute value of the characteristic slope, which correlates reasonably well with count-rate data. Low values of the characteristic slope correspond to large events preceded by a small number of small events, whereas a large characteristic slope value corresponds to a large number of small events. For panel I, lowest b values occur early in the schedule. The fact that none of these values is much less than one indicates that significant damage did not occur in this period; this finding is consistent with the count-rate data. Panel II, which was subjected to a much more severe thermal gradient than Panel I, shows much lower values of b (Fig. 27). Note that the characteristic slope values are closer to the 0.5 - 0.75 range during initial heating. During cooling, values of b closer to 1 are noted; this may indicate that little additional degradation occurs. In the previous report[1], initial amplitude-distribution results were obtained on uniformly heated samples. The values obtained for the characteristic slope were in the expected range of 1.6 to 2.0. These data, however, were obtained by summing the distribution over the entire firing, i.e., during both heating and cooling. The importance of the amplitude-distribution analysis lies in its potential ability to predict the formation of large cracks.[16] To have this predictive value, the characteristic slope must be obtained as a function of time.

The emphasize the potential detection capabilities of the b values, the change in b value was plotted as a function of time during the firing. The comparison between the data for panel I and panel II is shown in Figs. 28 and 29. Clearly, the largest negative change in b value for panel II occurs during heatup to 500°C, which is the period of maximum acoustic activity as evidenced by previous studies.[1] In contrast, (with the exception at 24 h) larger changes in b values for panel I occur during the cooling period, when significant acoustic activity was also detected in count-rate. Thus there is a suggested correlation between the higher count rate for each panel and the value of the change in time dependent b values.

Clearly the heterogeneous structure of the refractory concretes makes any quantitative analysis difficult. However, it is because of the heterogeneity of the material that high acoustic activity is present.

Work on acoustic emission from refractory concretes under cold-cracking, thermal-shock, and high-amplitude cyclic torsional testing has recently been reported by Davis.[17] This work also shows the high acoustic activity of refractory concretes.

In summary, this quarter's work has shown that amplitude distribution is a time-dependent parameter which can perhaps be correlated with other acoustic parameters and degradation mechanisms and shows promise of providing a way to predict large-crack formation.
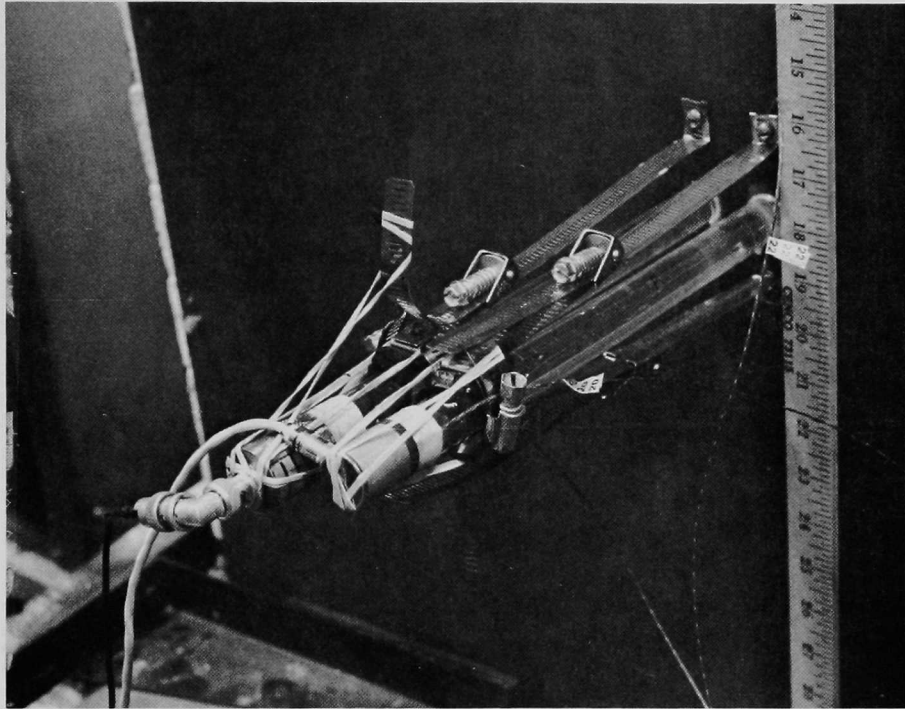
Fig. 20. Acoustic Waveguides Coupled to Steel Panel of Refractory
Concrete Test Sample
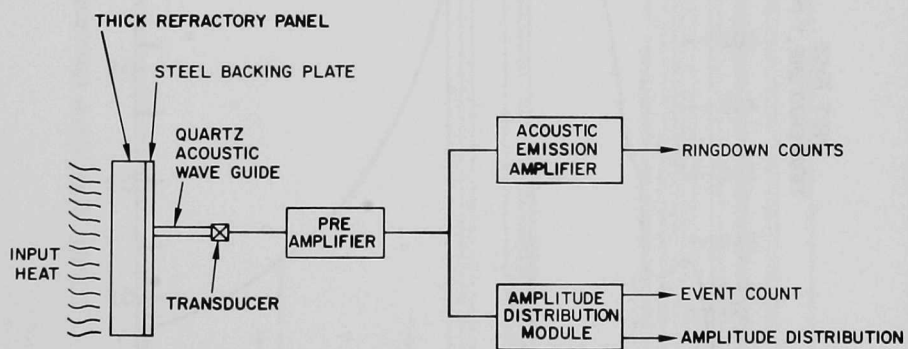
Fig. 21. Simplified Schematic of Test Setup to Measure Thermally
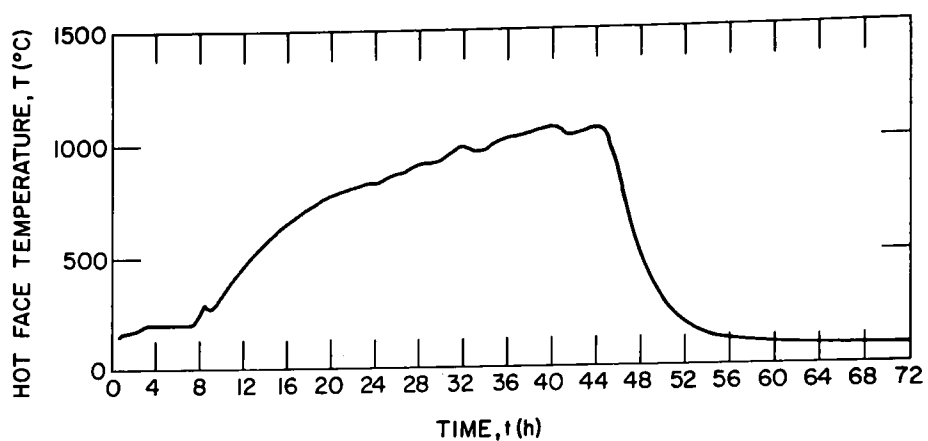Induced Acoustic Emissions. Neg. No. MSD 65255

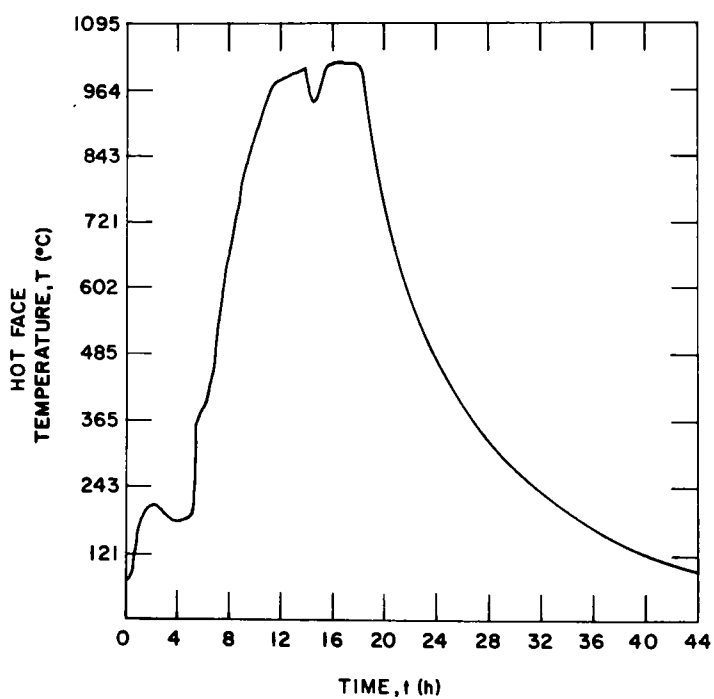Fig. 22. Time-dependent Surface Temperature of Hot Face of Panel I. Neg. No. ANL-306-78-502

Fig. 23. Time-dependent Surface Temperature of Hot Face of Panel II. Neg. No. ANL-306-78-507
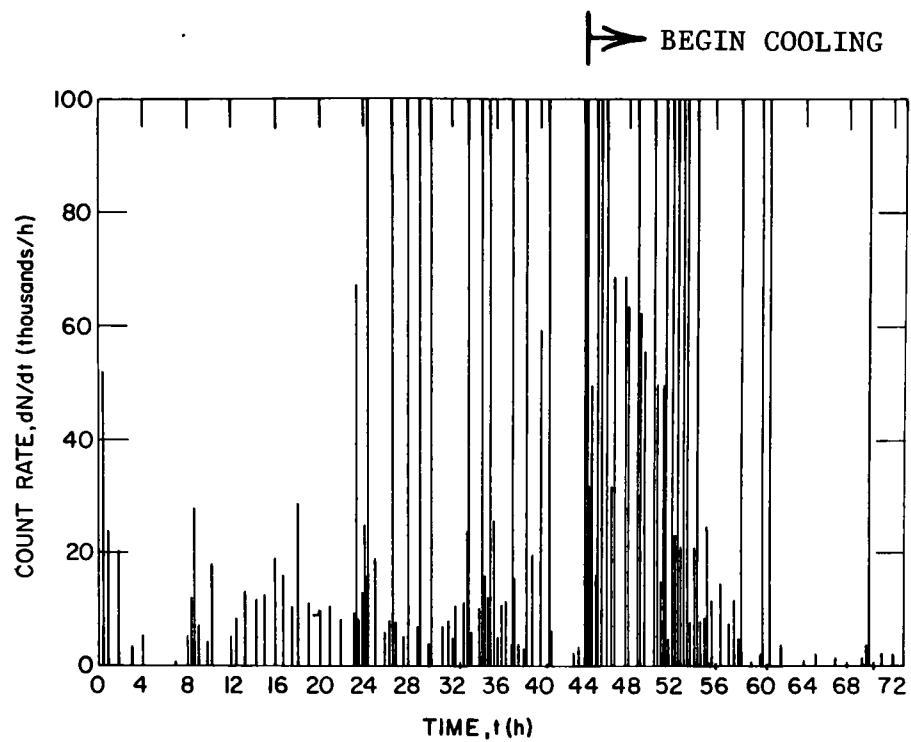
Fig. 24a. Count Rate vs Time for Panel I (175-kHz Resonant Transducer)
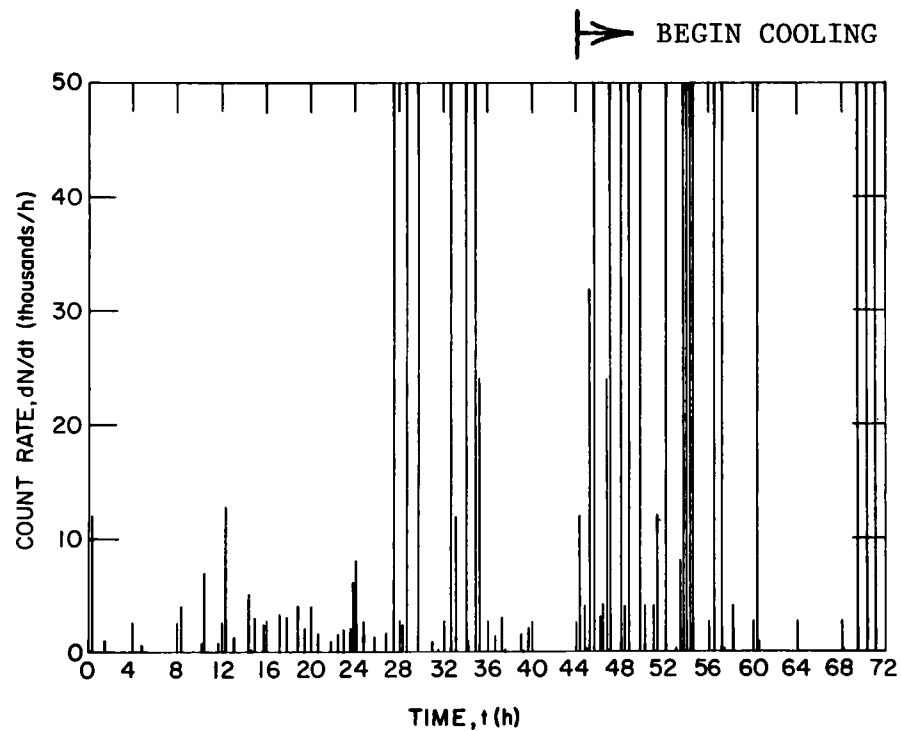Neg. No. ANL-306-78-503

Fig. 24b. Count Rate vs Time for Panel I (Broadband Transducer)
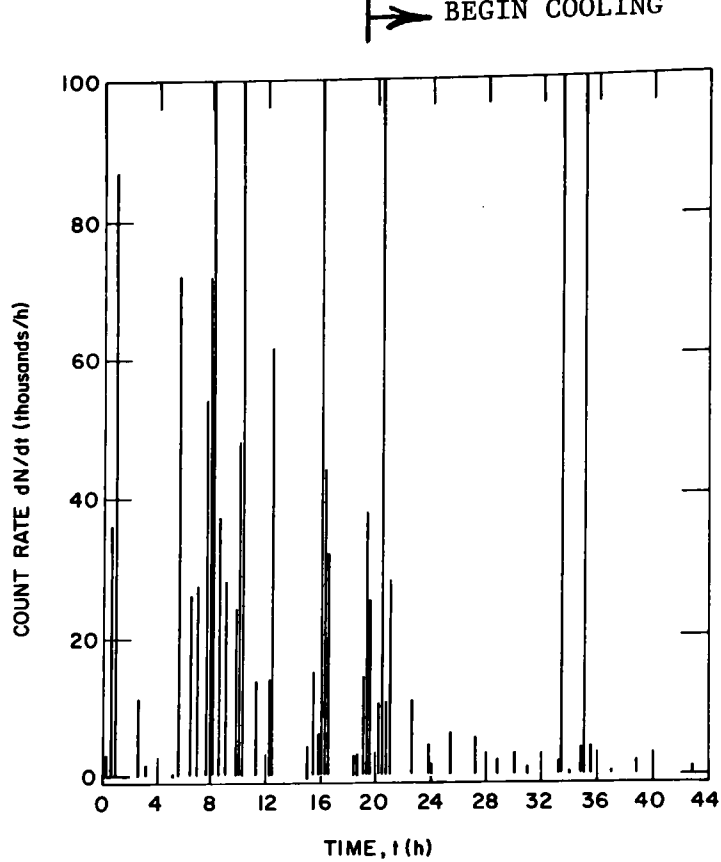Neg. No. ANL-306-78-504

Fig. 25a.   Count Rate vs Time for Panel II (175-kHz Resonant Transducer)
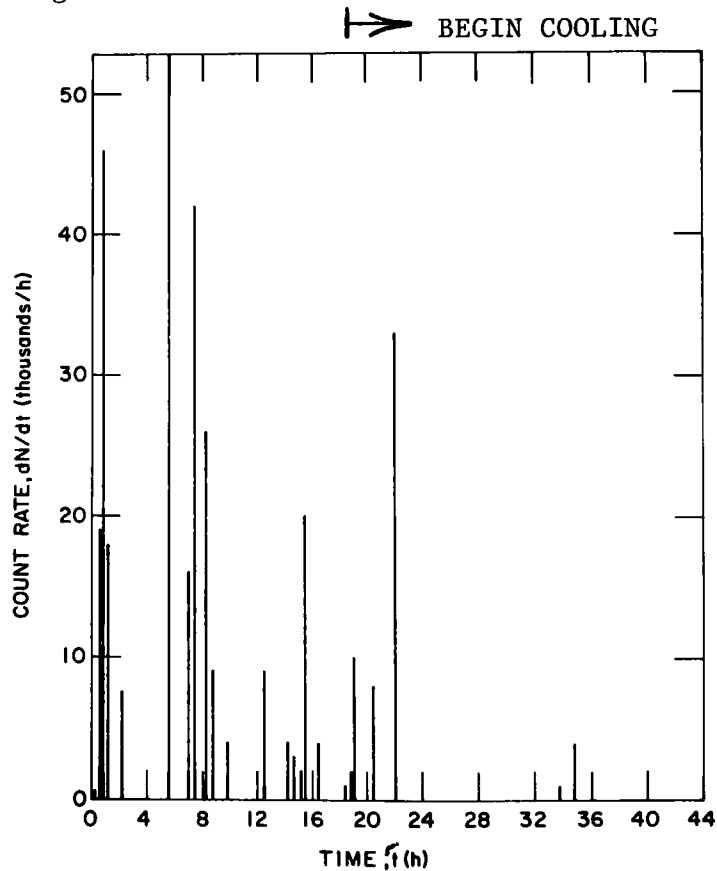   Neg. No. ANL-306-78-511

Fig. 25b.   Count Rate vs Time for Panel II (Broadband Transducer)
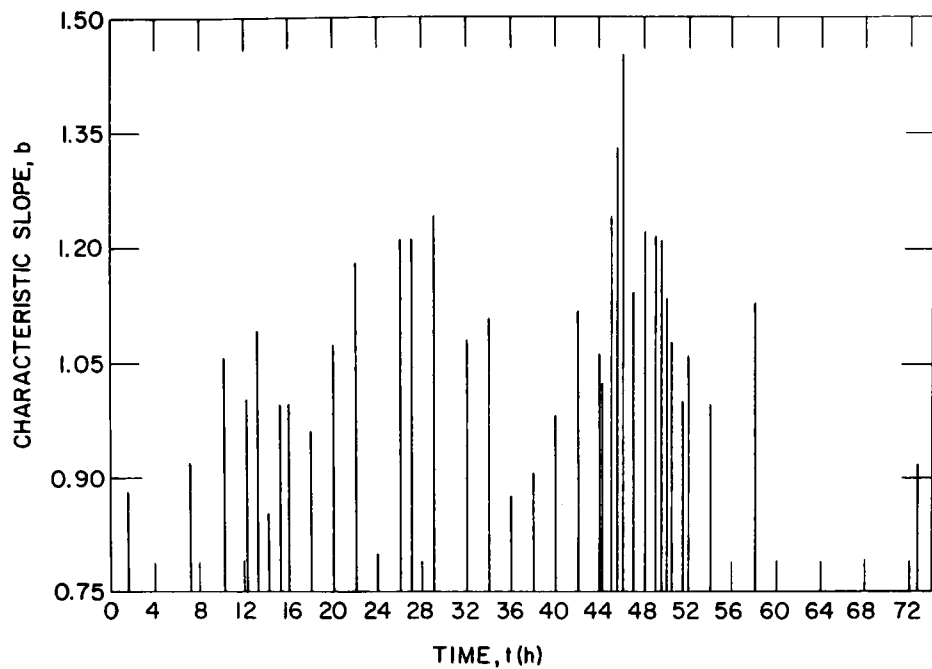   Neg. No. ANL-306-78-509

Fig. 26. Time-dependent Characteristic Slope Values for Panel I
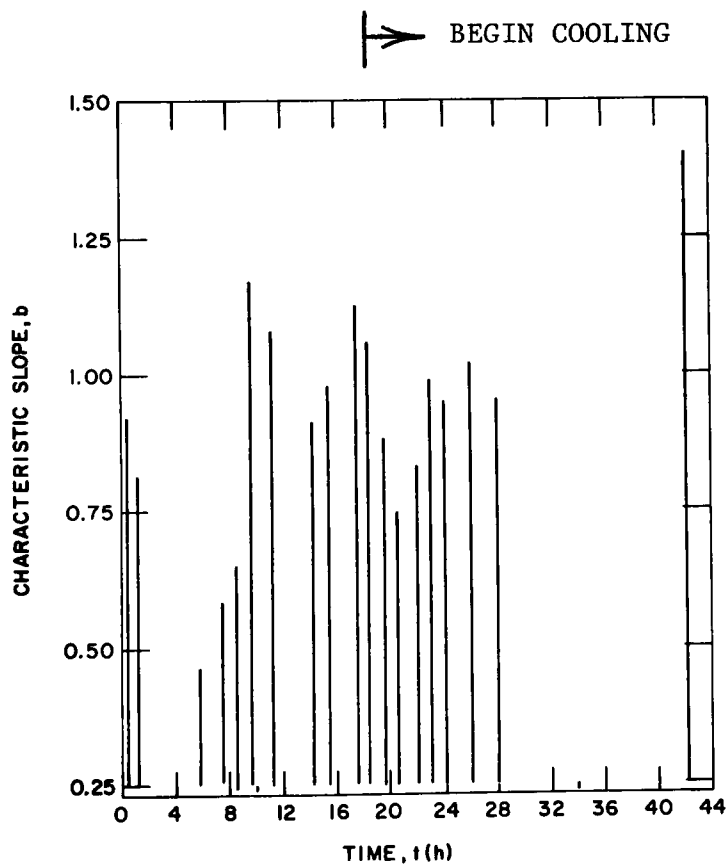(175-kHz Resonant Transducer). Neg. No. ANL-306-78-492

Fig. 27. Time-dependent Characteristic Slope Values for Panel II
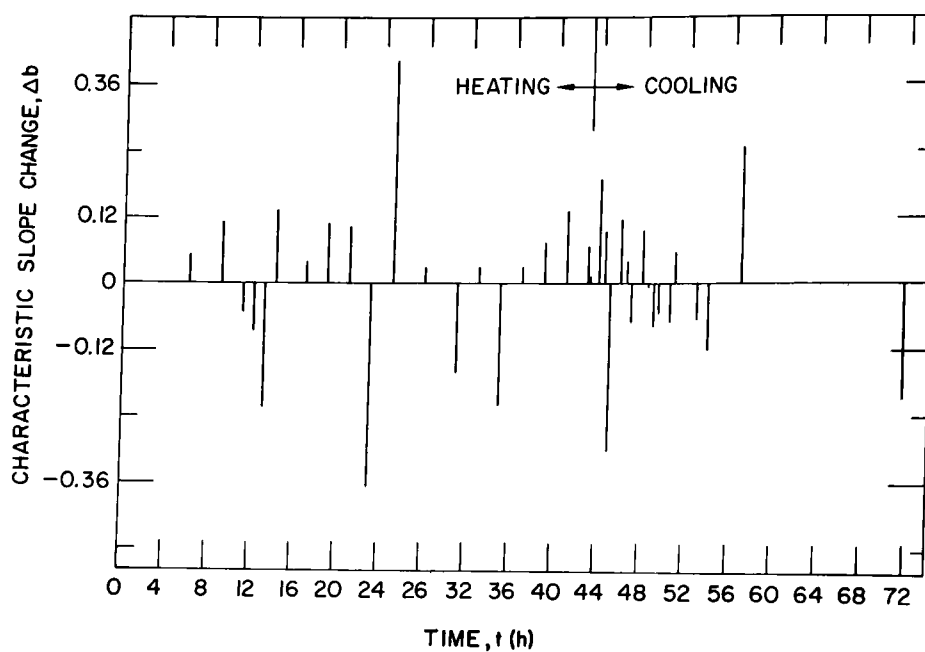(175-kHz Resonant Transducer). Neg. No. ANL-306-78-498

49

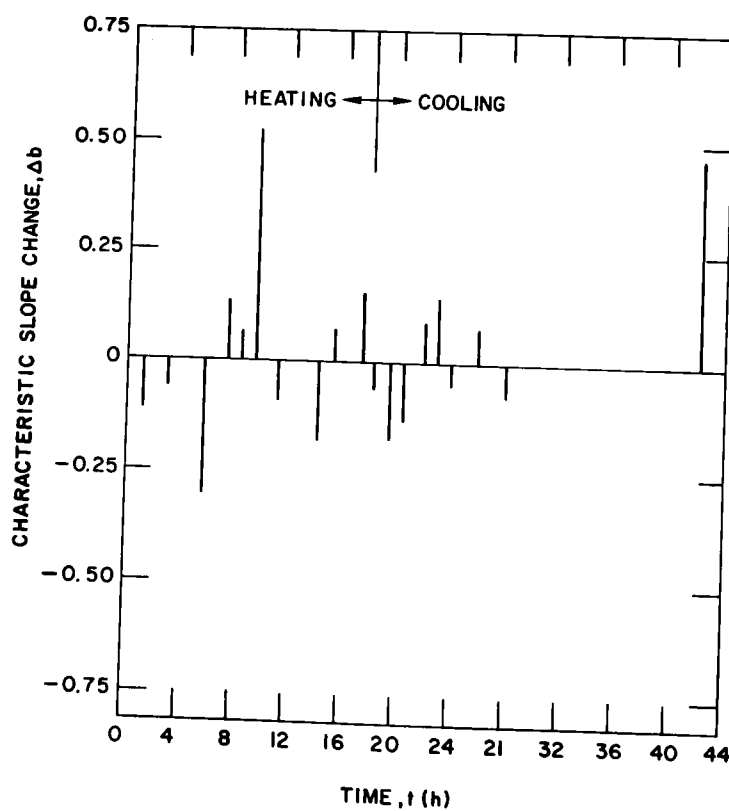Fig. 28. Time-dependent Change in Characteristic Slope Values for Panel I. Neg. No. ANL-306-78-515

Fig. 29. Time-dependent Change in Characteristic Slope Values for Panel II. Neg. No. ANL-306-78-514

50

3. Component Inspection

    a. Acoustic Monitoring of Valves

        Work has continued on the correlation of acoustic output with mass
flow rate for orifices of different sizes and shapes in the choked and unchoked
flow regimes. These results will be reported in the next Quarterly. Estimates
are being obtained on the cost of modifying commercially available acoustic-
emission equipment to produce a prototype leak-detection instrument for more
extensive field testing.

Task D — Corrosion Behavior of Materials in Coal-conversion Processes
(K. Natesan)

The objectives of this program are to (1) develop uniaxial tensile data on four commercial alloys upon exposure to multicomponent gas environments, (2) experimentally evaluate the high-temperature corrosion behavior of iron- and nickel-base alloys in gas environments with a wide range of oxygen, sulfur and carbon potentials, and (3) develop a systems approach based upon available thermodynamic and kinetic information so that possible corrosion problems in different coal-conversion processes can be evaluated.

1. Uniaxial Tensile Properties

The experimental program used to generate uniaxial tensile data on four iron- and nickel-base alloys upon exposure to multicomponent gas environments has been discussed in detail in an earlier report.[18] The composition of the alloys is given in Table XIII. The gas mixtures (Table XIV) contain CO, CO_2, H_2, H_2O, and H_2S with additions of CH_4 and/or N_2. The temperatures for the exposure of tensile specimens in the present program are 750°C (1380°F), 871°C (1600°F), and 982°C (1800°F); the test pressure is 0.101 MPa (1 atm). Figure 30 shows a photograph of the experimental system used for the pre-exposure of corrosion and mechanical test specimens. The details of the specimen support arrangement are shown in Fig. 31. Results from initial corrosion experiments on Type 310 stainless steel, Incoloy 800, Inconel 671, and U.S. Steel Alloy 18-18-2 in the gas mixtures given in Table XIV were reported earlier.[4] Details of the specimen design and fabrication and the test procedure, as well as data on the tensile properties of the four alloys in the as-received condition at temperatures of 750, 871, and 982°C, were given in an earlier report.[2] A listing of the experimental runs to be conducted in the present program is given in Table XV.

During the present quarter, 1000-h exposures of corrosion and uniaxial tensile specimens to gas mixture 1A at 750 and 871°C and to gas mixture 2A at 750°C were completed. Postexposure tensile tests of the specimens were conducted in vacuum at an initial strain rate of 4.1×10^{-4} s^{-1}. The load-elongation data from the tensile tests were converted to true stress-true strain curves for the alloys in the as-received condition and after exposure to the multicomponent gas environments. Figures 32-35 show the true stress-true strain curves for Incoloy 800, Type 310 stainless steel, U.S. Steel Alloy 18-18-2, and Inconel 671, respectively, in the as-received condition and after 1000-h exposures identified as runs A01A750 and E12A750. In general, the flow stress of the material decreases after exposure to complex gas mixtures when compared with that of the material in the as-received condition. Thermochemical calculations showed that all the alloys should develop protective oxide scales upon exposure to the gas mixtures. Microstructural observations on the type and morphology of scale layers and the extent of intergranular penetration of sulfur in these alloys are presented later in this report. Since < 10-μm-thick oxide layers developed in these alloys, the lower flow-stress values observed in the preexposed specimens may be the result of microstructural changes that accompany thermal aging of the specimens. After prolonged exposure at the test temperature, high-chromium alloys of the type used in the present investigation develop sigma phase, i.e., an intermetallic (Fe,Cr) compound, preferentially at grain boundaries. To clarify this point, specimens of different high-chromium alloys will be thermally aged for 1000 h in an argon environment at temperatures of 750, 871, and 982°C.

Figures 36 and 37 show the true stress-true strain curves for Type 310 stainless steel and Inconel 671, respectively, in the as-received condition and after a 1000-h exposure to a complex gas environment at 871°C (run A01A871). The results show that the preexposure leads to a decrease in flow stress and a substantial increase in axial strain. Incoloy 800 specimens that were exposed along with the other specimens in this run were fully embrittled, and specimens of U.S. Steel Alloy 18-18-2 were completely corroded.

The load-elongation data from the tensile tests were also used to evaluate engineering tensile properties such as 0.2% yield stress, ultimate tensile strength (UTS), uniform strain, and total elongation. Tables XVI and XVII show listings of these properties for the alloys in the as-received condition and after 1000-h exposures to complex gas mixtures at test temperatures of 750 and 871°C, respectively. Data in Tables XVI and XVII show that preexposure of the materials to multicomponent gas mixtures results in a decrease in 0.2% yield stress and UTS with only minimal increases in the uniform strain over the range of ∿ 4 to 10%.

2. Microstructrual Observations

After the mechanical tests were completed, the cross sections and fracture surfaces of uniaxial tensile specimens were examined by SEM with an energy-dispersive x-ray analyzer. Figures 38-41 show SEM photographs of the cross sections of Incoloy 800, Type 310 stainless steel, Inconel 671, and U.S. Steel Alloy 18-18-2, respectively, after a 1000-h exposure to a complex gas mixture (run A01A750). Also shown in these figures are the metallic element (chromium, silicon, and manganese) and sulfur (if present) distributions in the scale/alloy interface regions of the samples. Figures 38-40 show that the scales developed on Incoloy 800, Type 310 stainless steel, and Inconel 671 in run A01A750 are predominantly Cr-rich oxide; virtually no sulfur was detected. The thickness of the oxide scale in these specimens ranged between 3 and 5 μm, and the depth of intergranular penetration in the alloy ranged between 3 and 10 μm. On the other hand, the U.S. Steel Alloy 18-18-2 developed a much thicker two-layered scale after exposure to the gas mixture in run A01A750. The outer scale layer consisted of Ni-rich sulfide and the interior layer was of Cr-rich oxide. The thickness of each layer was ∿40 μm, and the depth of intergranular penetration was ∿ 20 μm. The sulfidation mode of attack in this alloy is consistent with earlier corrosion data[4] for this alloy in complex gas mixtures. The metallic-element-distribution photographs in Figs. 38-41 also show a predominant transport of Mn and Si toward the scale; the extent of Si migration is greatest in U.S. Steel Alloy 18-18-2, probably due to a larger initial concentration of Si in this material.

Figures 42 and 43 show the SEM photographs of the fracture surfaces of Incoloy 800 and Type 310 stainless steel tensile specimens after 1000-h exposure to the gas mixture in run A01A871 at 871°C. The X-ray analyses showed that two types of phases, i.e., (Fe,Cr) sulfide and (Fe,Ni) compound, were present in the fracture surface of Incoloy 800. In Type 310 stainless steel specimens, the X-ray analyses showed that the scale was predominantly Cr-rich oxide. There was evidence of an (Fe,Cr) intermetallic compound, probably the sigma phase, which is prevalent in iron-base alloys with high-Cr content. The sulfide phase was of the

type (Cr,Mn)S$_x$; distinct particles of this phase were observed on the fracture surface. Additional examinations of these specimens and analyses of the phases are presently being conducted.

Figures 44 and 45 show the SEM photographs of the fracture surfaces of Incoloy 800, Inconel 671, Type 310 stainless steel, and U.S. Steel Alloy 18-18-2 tensile specimens after a 1000-h exposure to gas mixture 1A at 750°C (run A01A750). The results show the presence of Cr-rich oxide scales in all the alloys with the exception of U.S. Steel Alloy 18-18-2. Additional experiments are being conducted to evaluate the tensile behavior of these alloys after exposure to the gas mixtures listed in Table XIV.

TABLE XIII. Composition (wt %) of Alloys for Uniaxial Tensile Tests

Alloy	Cr	Ni	Se	Mn	Ti	Al	C	Fe
Incoloy 800	20	32.5	0.35	0.75	0.38	0.38	0.05	balance
Type 310 stainless steel	25	20	0.4	1.5	–	–	0.25	balance
Inconel 671	48	50	–	–	0.35	–	0.05	–
U.S. Steel Alloy 18-18-2	18.5	17.8	2.05	1.25	–	–	0.06	balance

TABLE XIV. Composition[a] of Gas Mixtures for Exposure of Corrosion and Uniaxial Tensile Specimens

Species	Gas Mixture					
	1A	1B	2A	2B	3A	3B
CO	11.7	9.1	17.3	13.4	26.0	20.1
CO_2	15.4	12.0	11.5	8.9	14.9	11.5
H_2	13.0	10.0	23.0	17.8	26.0	20.1
H_2O	48.9	37.9	37.2	28.9	22.1	17.3
H_2S	1.0	1.0	1.0	1.0	1.0	1.0
CH_4	10.0	30 0	10.0	30.0	10.0	30.0

[a]Vol % at room temperature

TABLE XV. Experimental Runs[a]

Run Identification	Gas Mixture	Remarks
AO	1A	
BO	3A	Complement to Runs 1-4 of Battelle
E1	2A	
CO	1B	
DO	3B	Complement to Runs 5-8 of Battelle
E2	2A	
EO	2A	
FO	2B	Complement to Runs 13-16 of Battelle

[a]Total number of runs: 24 (8 runs at each of the three temperatures)

Exposure time for each run: 1000 h

Run Code: AO 1A 982

Run   Gas Mixture   Exposure
Identification   Identification   Temperature, °C

56

TABLE XVI. Uniaxial Tensile Properties of Four Alloys in the As-received Condition and After
1000-h Exposures to Multicomponent Gas Environments at 750°C

Alloy	Treatment	0.2% Yield Stress, MPa	Ultimate Tensile Strength, MPa	Uniform Strain, %	Total Elongation, %
Incoloy 800	As-received	91.0	226.7	4	136
	A01A750	53.3	204.2	10.8	100.4
	E12A750	40.5	200.0	8.8	70.4
Type 310	As-received	49.2	257.9	4	38
Stainless	A01A750	43.2	219.4	8.1	36.4
Steel	E12A750	36.1	222.9	9.4	27.5
U. S. Steel	As-received	63.5	191.2	8	70
Alloy 18-18-2	A01A750	57.6	181.9	12.3	64.5
	E12A750	43.7	182.6	9.8	62.5
Inconel 671	As-received	49.2	339.0	9	32
	A01A750	48.5	265.3	3.9	77
	E12A750	45.1	256.9	5.9	54.1

TABLE XVII. Uniaxial Tensile Properties of Four Alloys in the As-received Condition and After 1000-h Exposures to Multicomponent Gas Environment at 871°C

Alloy	Treatment	0.2% Yield Stress, MPa	Ultimate Tensile Strength, MPa	Uniform Strain, %	Total Elongation, %
Incoloy 800	As-received	30.7	119.7	4	123
	A01A871		Sample Embrittled		
Type 310 Stainless Steel	As-received	43.0	138.5	3	48
	A01A871	20.0	106.5	8.9	76
U. S. Steel Alloy 18-18-2	As-received	36.8	94.5	3	71
	A01A871		Sample Corroded		
Inconel 671	As-received	42.0	141.1	5	87
	A01A871	27.3	105.9	4.9	172
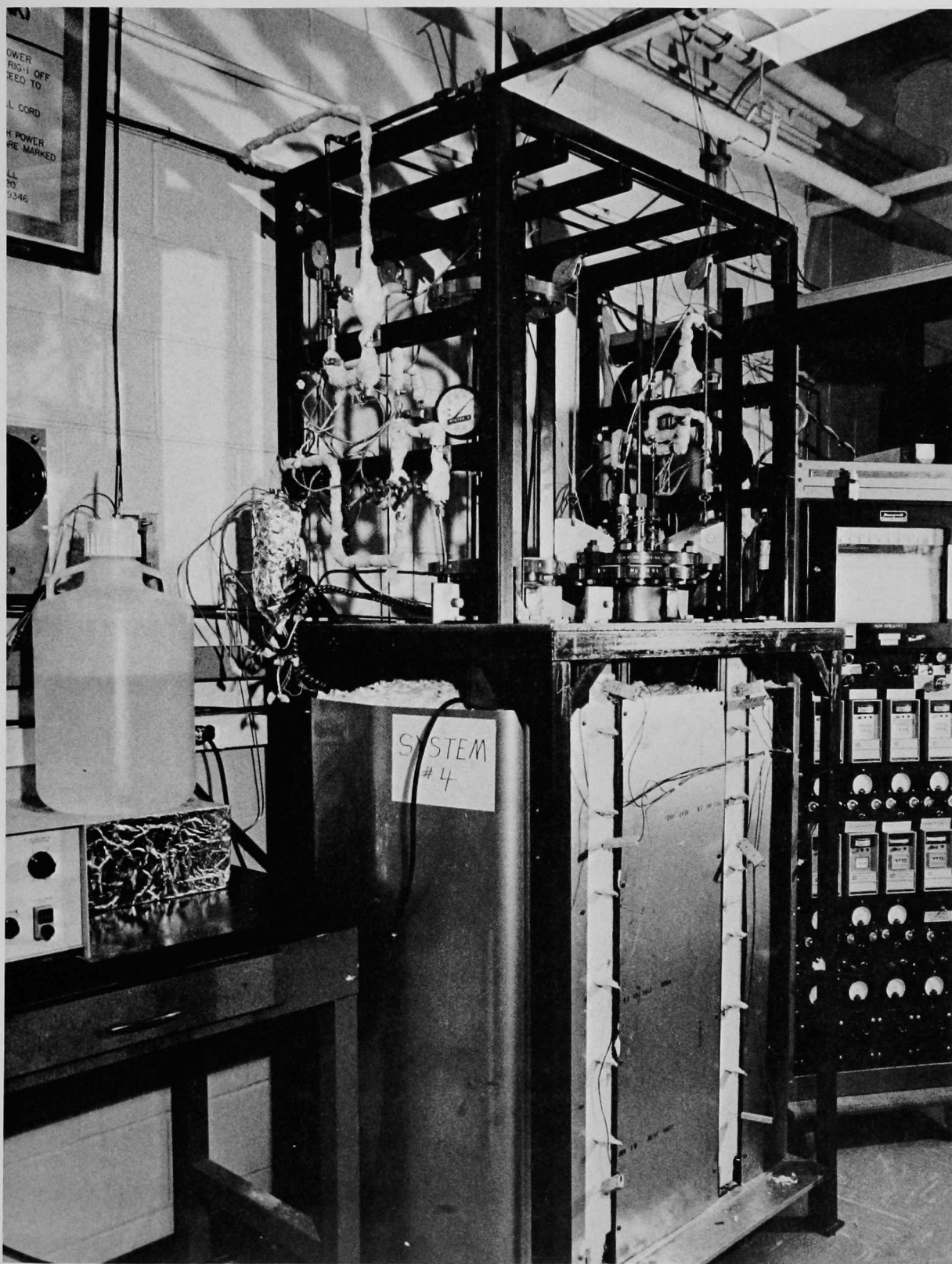
Fig. 30. Photograph of Experimental System Used for Exposure of
Corrosion and Mechanical-test Specimens
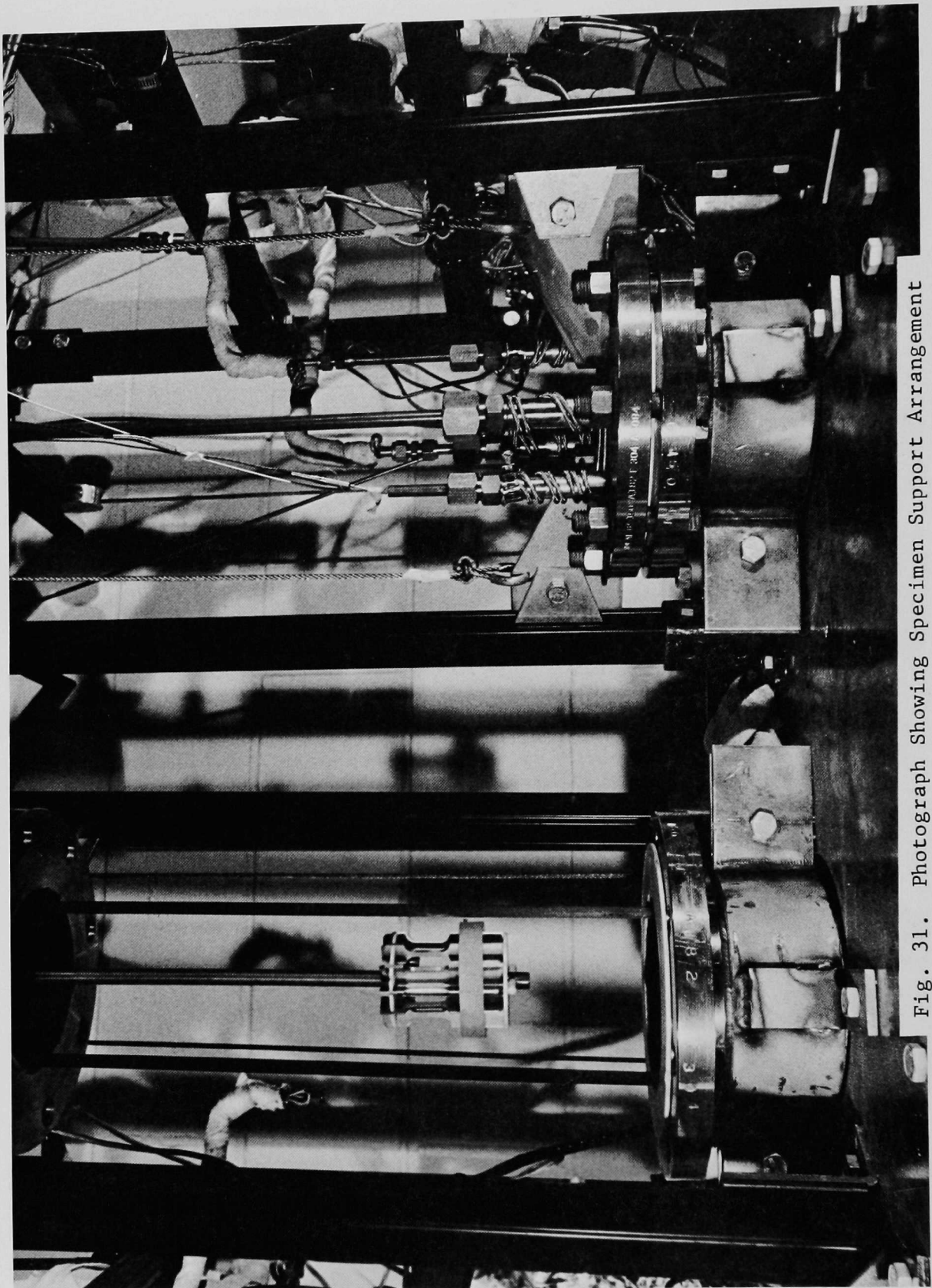
Fig. 31. Photograph Showing Specimen Support Arrangement
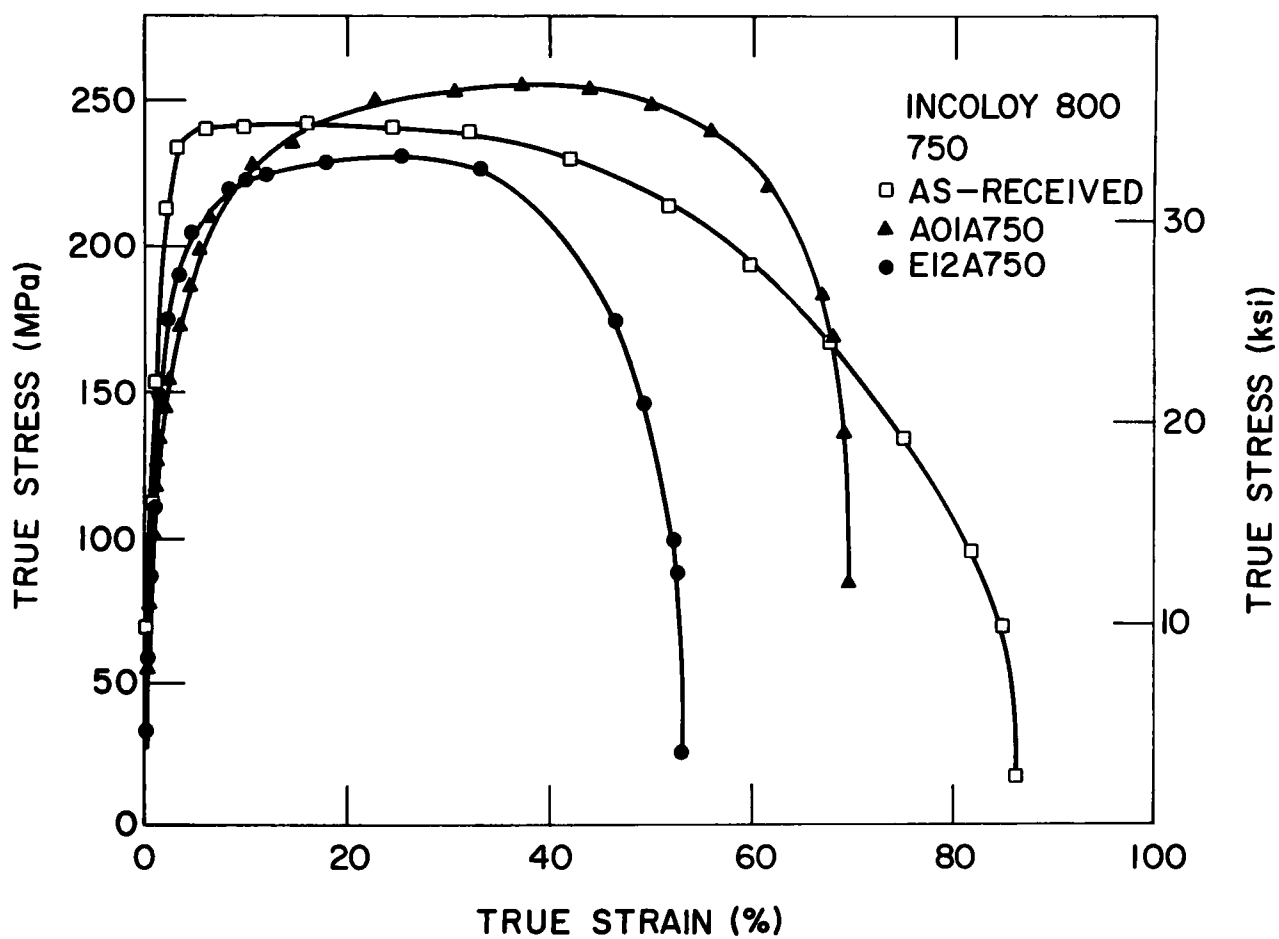
Fig. 32. True Stress-True Strain Curves for Incoloy 800 in the As-received Condition and After 1000-h Exposures to Complex Gas Mixtures at 750°C. Neg. No. ANL-306-78-328
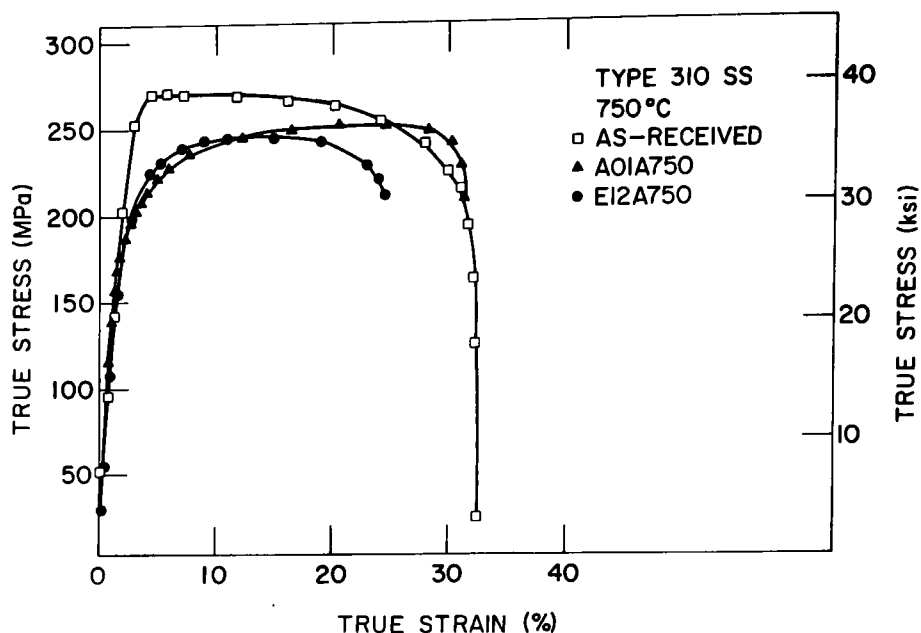
Fig. 33. True Stress-True Strain Curves for Type 310 Stainless Steel in the As-received Condition and After 1000-h Exposures to Complex Gas Mixtures at 750°C. Neg. No. ANL-306-78-307
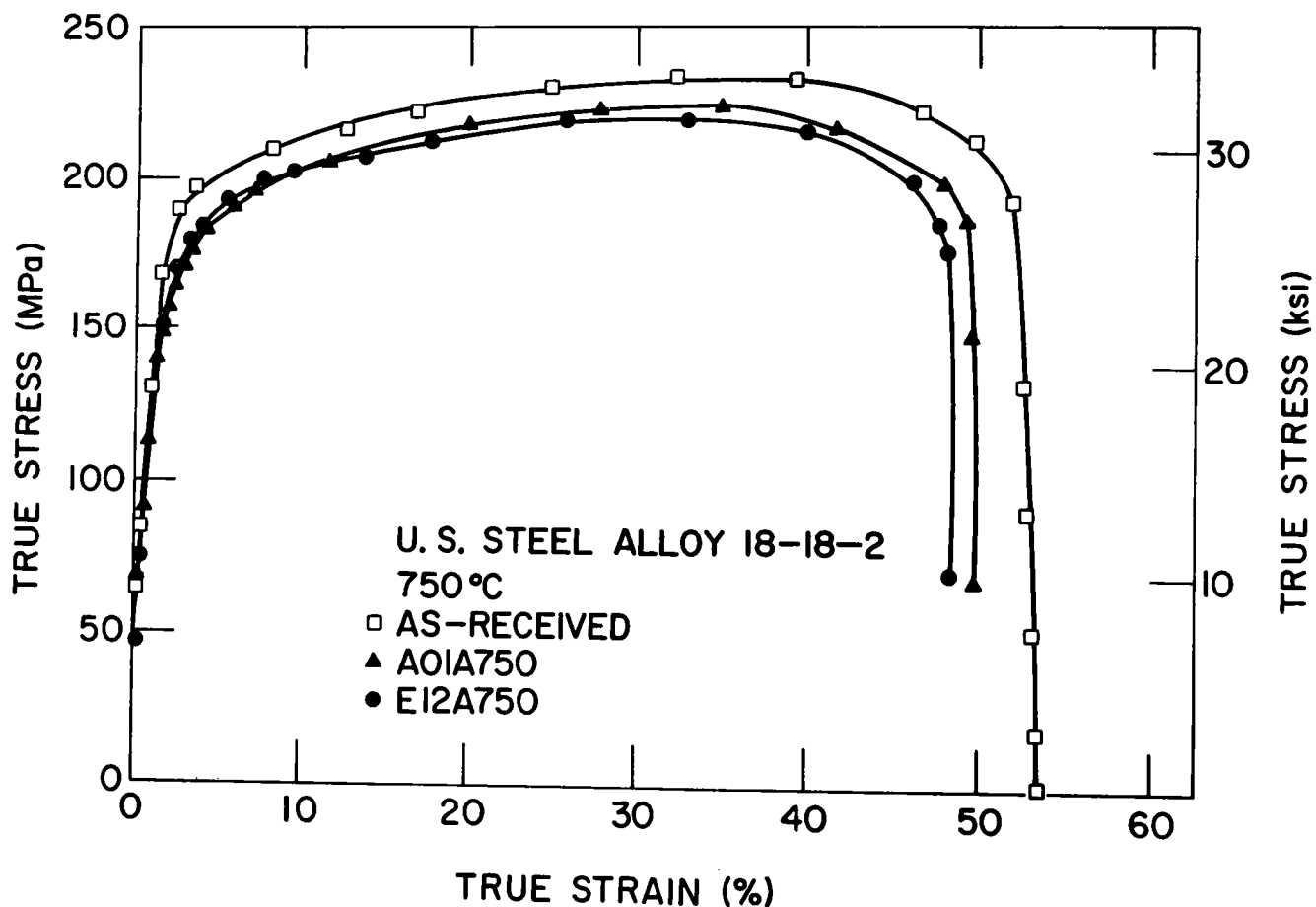
Fig. 34. True Stress-True Curves for U.S. Steel Alloy 18-18-2 in the As-received Condition and After 1000-h Exposures to Complex Gas Mixtures at 750°C. Neg. No. ANL-306-78-334
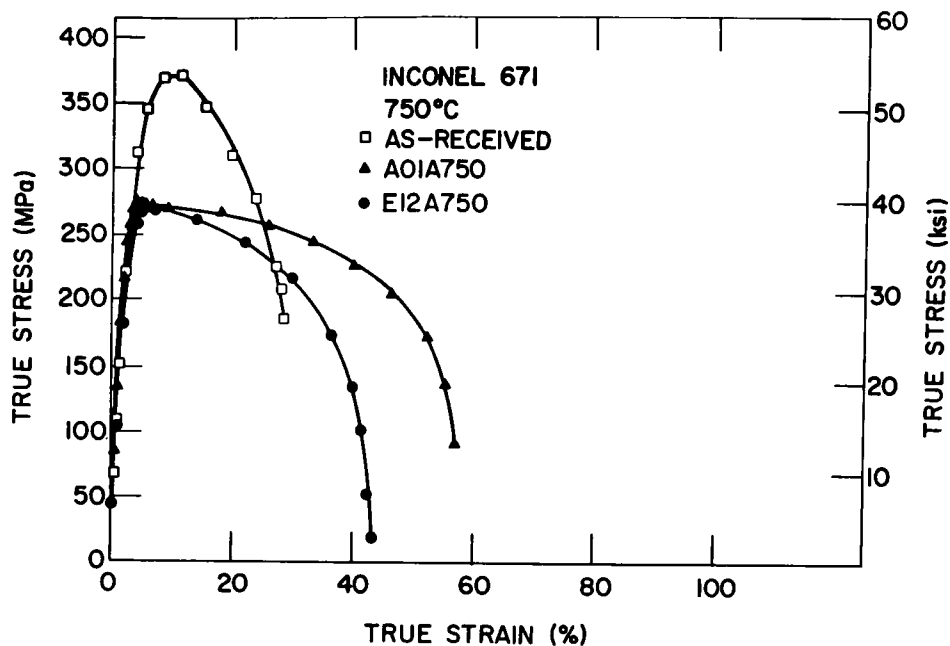
Fig. 35. True Stress-True Strain Curves for Inconel 671 in the As-received Condition and After 1000-h Exposures to Complex Gas Mixtures at 750°C. Neg. No. ANL-306-78-333
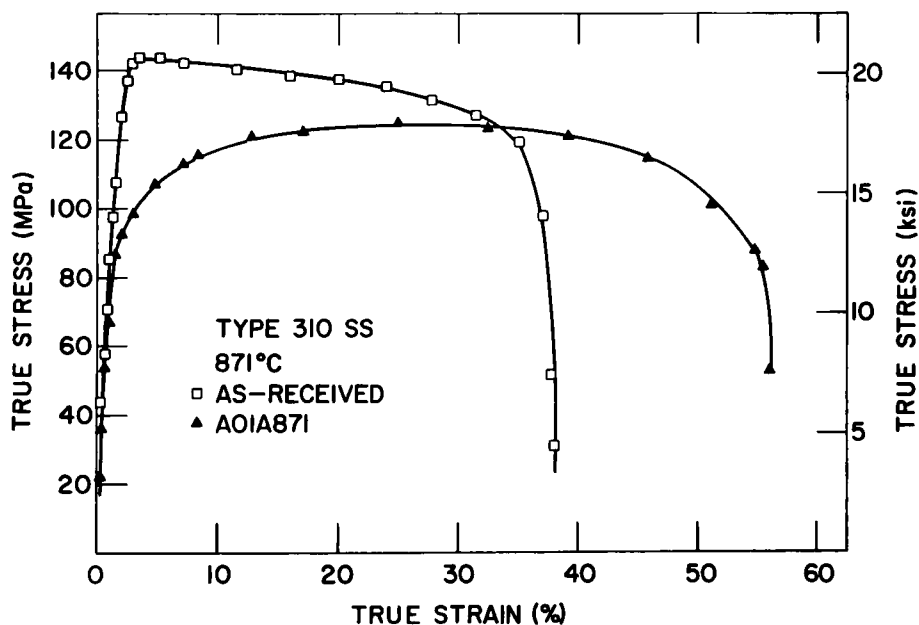
Fig. 36. True Stress-True Strain Curves for Type 310 Stainless Steel in the As-received Condition and After a 1000-h Exposure to a Complex Gas Mixture at 871°C. Neg. No. ANL-306-78-306
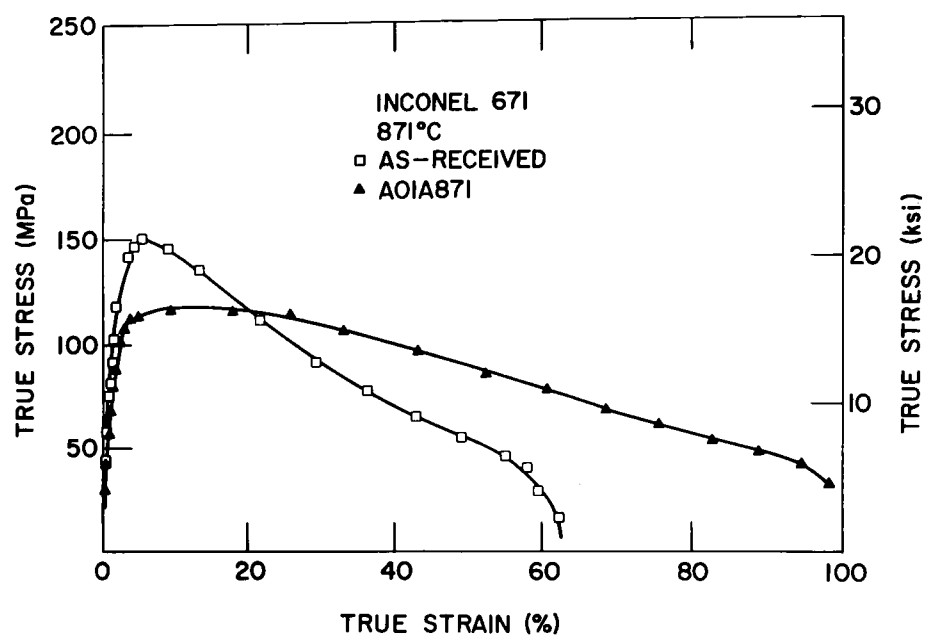
Fig. 37. True Stress-True Strain Curves for Inconel 671 in the As-received
Condition and After a 1000-h Exposure to a Complex Gas Mixture
at 871°C. Neg. No. ANL-306-78-332
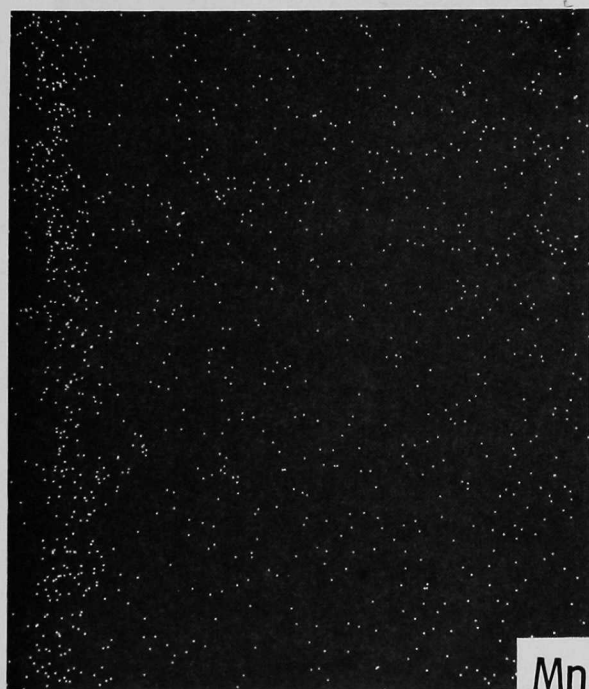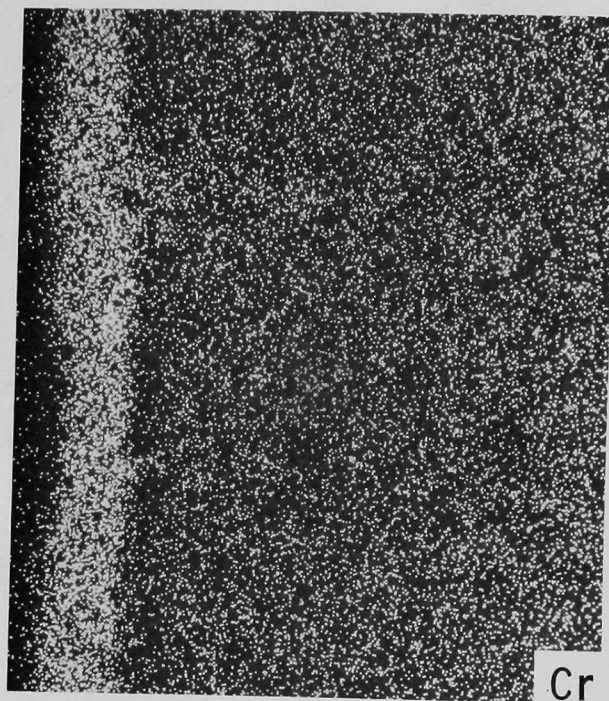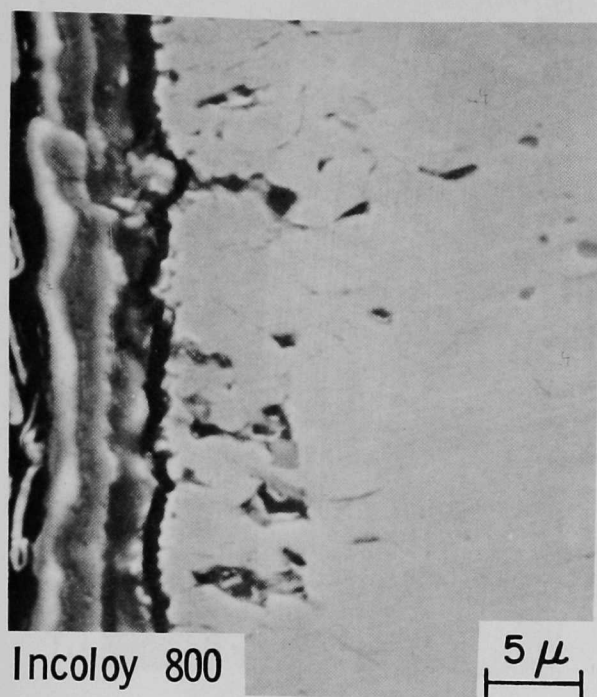
Fig. 38. X-ray Photograph and Cr, Mn, and Si Distribution in Incoloy 800 Specimen
After a 1000-h Exposure to a Complex Gas Mixture at 750°C (Run A01A750).
In the distribution pictures, light regions indicate high concentrations
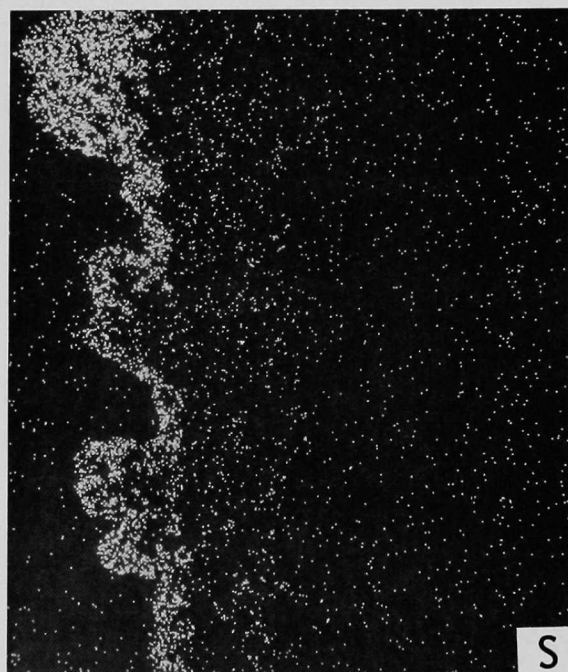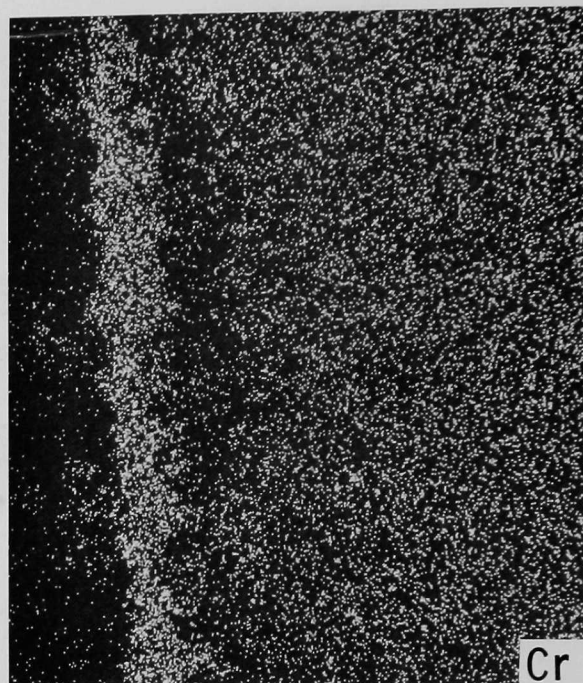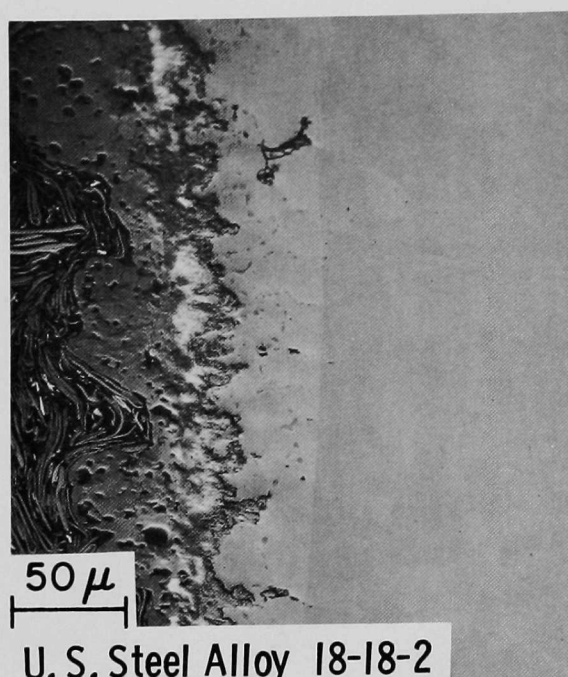of the respective elements. Neg. No. ANL-306-78-339
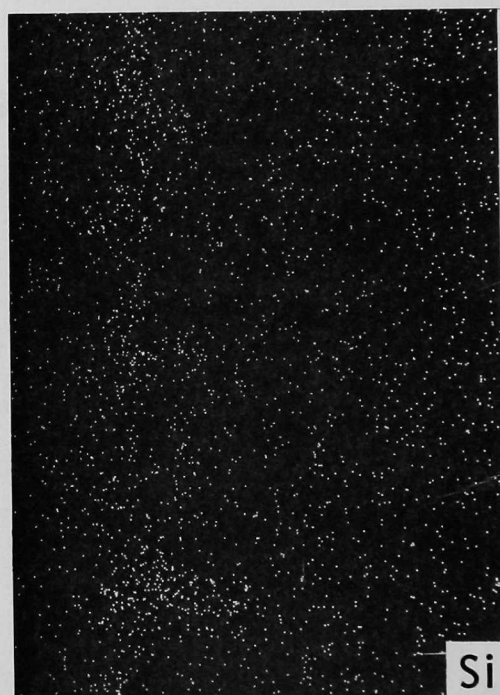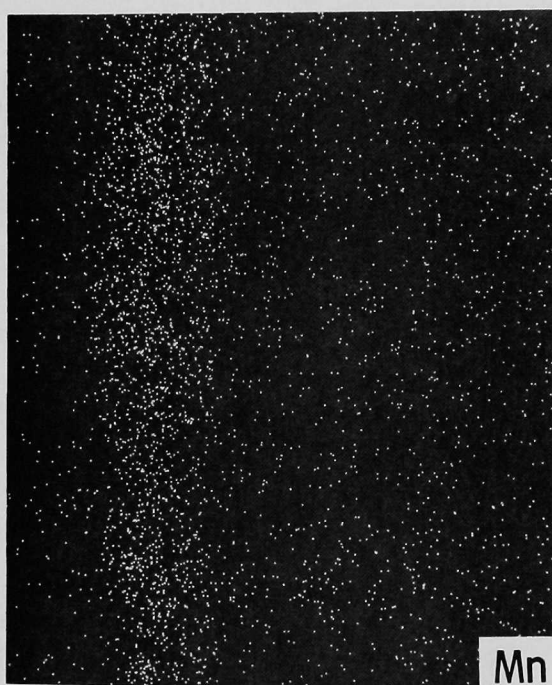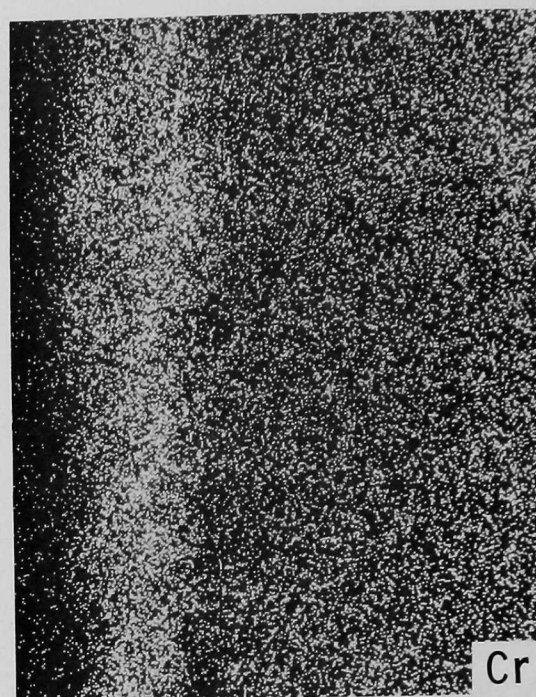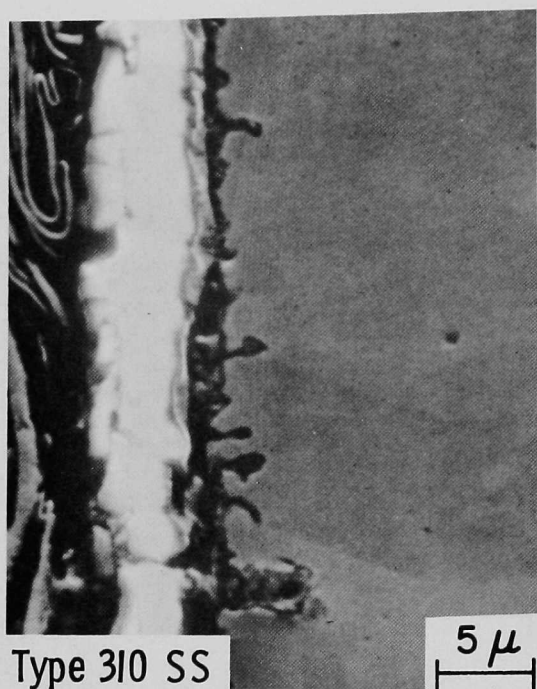
Fig. 39. X-ray Photograph and Cr, Mn, and Si Distribution in Type 310 Stainless Steel Specimen After a 1000-h Exposure to a Complex Gas Mixture at 750°C (Run A01A750). In the distribution pictures, light regions indicate high concentrations of the respective elements. Neg. No. ANL-306-78-343
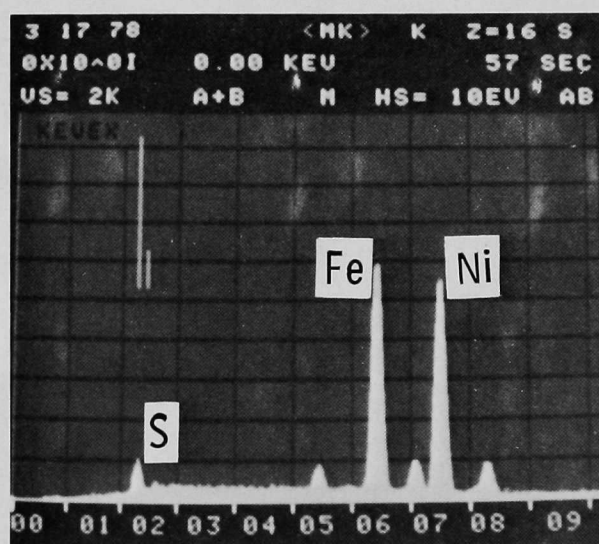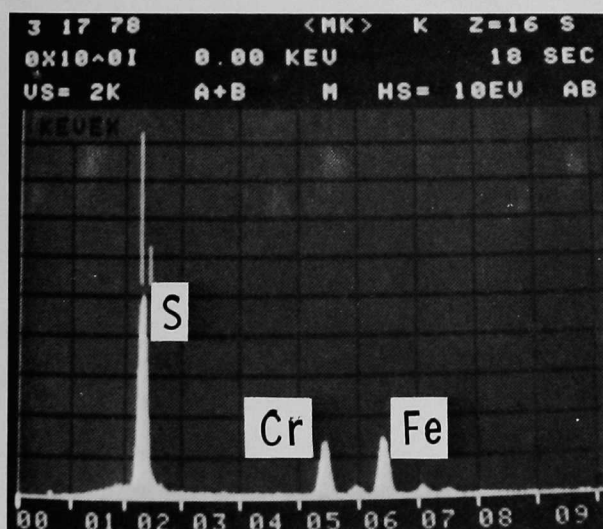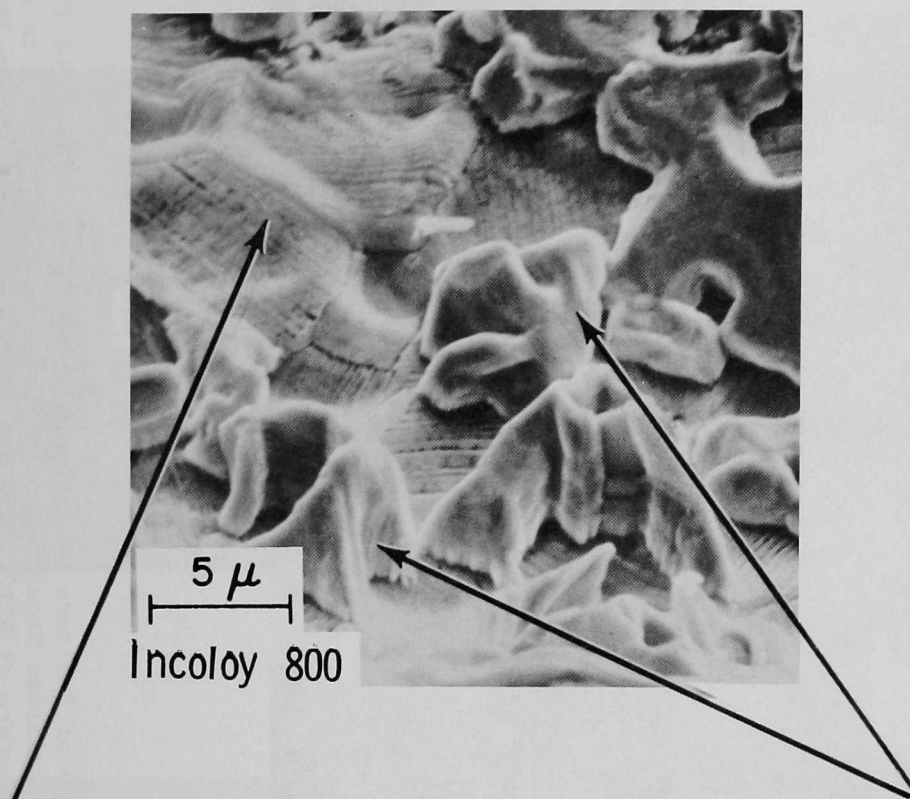
Inconel 671   5 μ   **Cr**   **S**
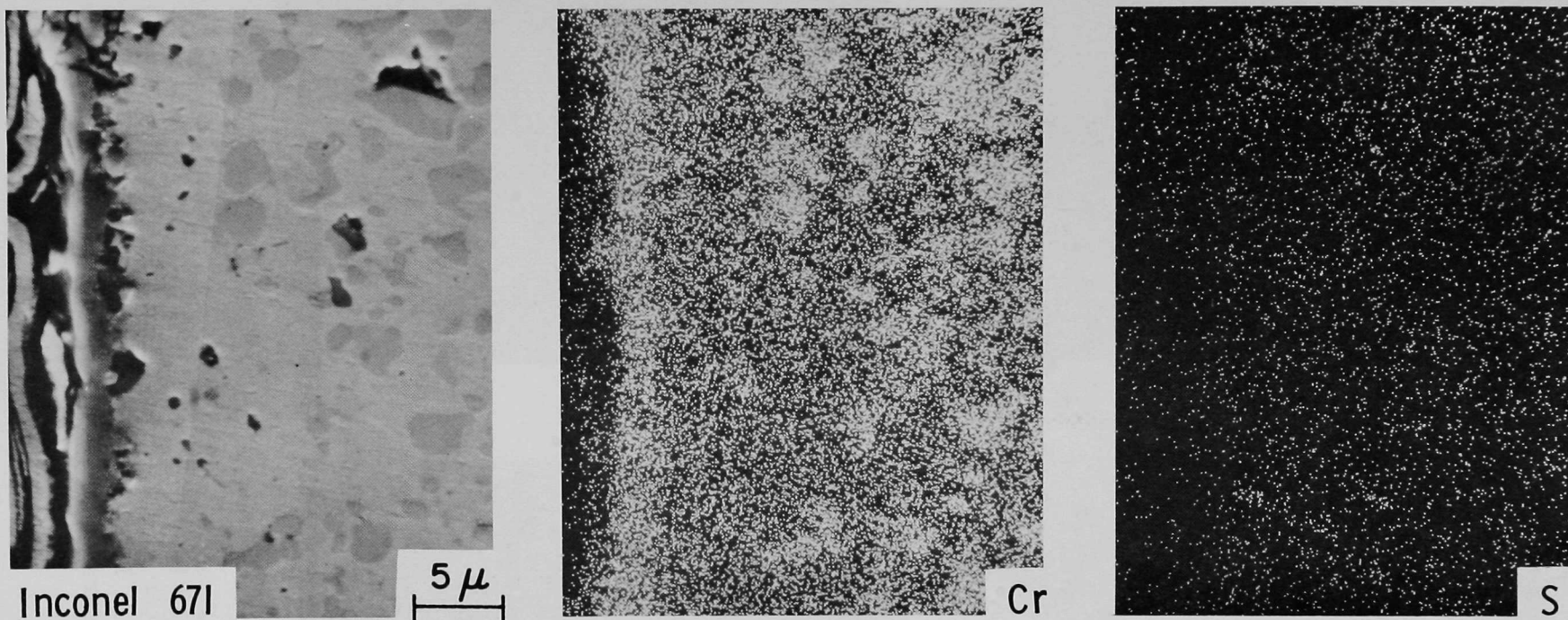
Fig. 40. X-ray Photograph and Cr and S Distribution in Inconel 671 Specimen After a 1000-h Exposure to a Complex Gas Mixture at 750°C (Run A01A750). In the distribution pictures, light regions indicate high concentrations of the respective elements. Neg. No. ANL-306-78-337

Fig. 41. X-ray Photograph and Cr, S, and Si Distribution in U.S. Steel Alloy 18-18-2 Specimen After a 1000-h Exposure to a Complex Gas Mixture at 750°C (Run A01A750). In the distribution pictures, light regions indicate high concentrations of the respective elements. Neg. No. ANL-306-78-338

Fig. 42. SEM Photograph of Fracture Surface and X-ray Identification of Phases in Incoloy 800 Specimen After a 1000-h Exposure to a Complex Gas Mixture at 871°C (Run A01A871). Neg. No. ANL-306-78-342
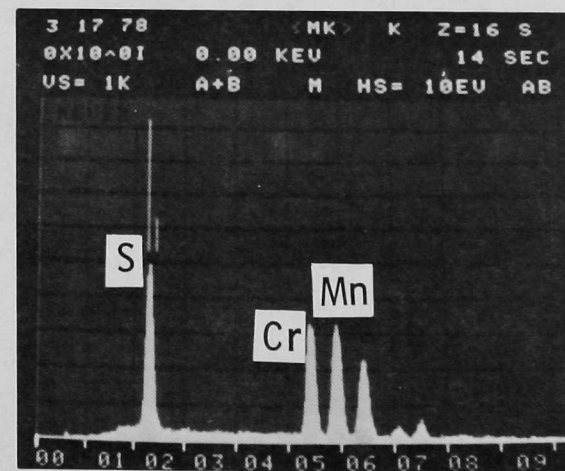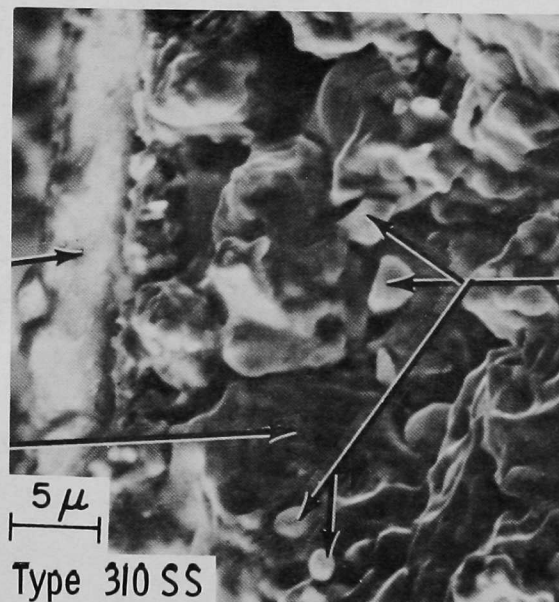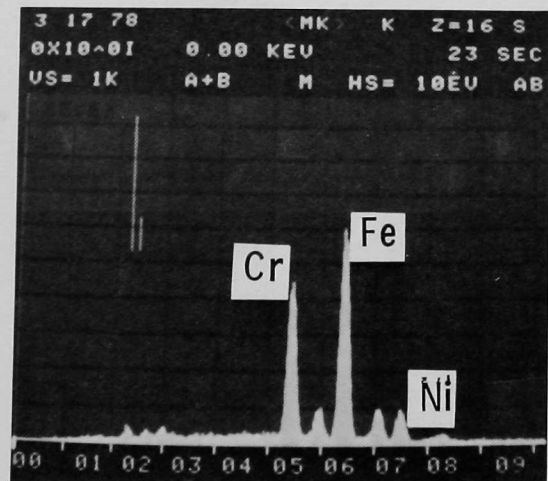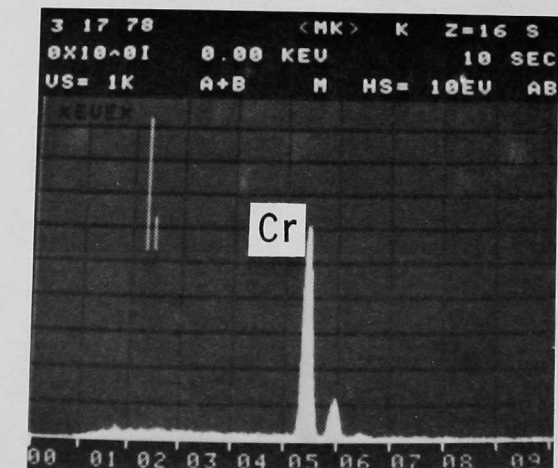
Fig. 43.   SEM Photograph of Fracture Surface and X-ray Identification of Phases in Type 310 Stainless Steel Specimen After a 1000-h Exposure to a Complex Gas Mixture at 871°C (Run A01A871).   Neg. No. ANL-306-78-340
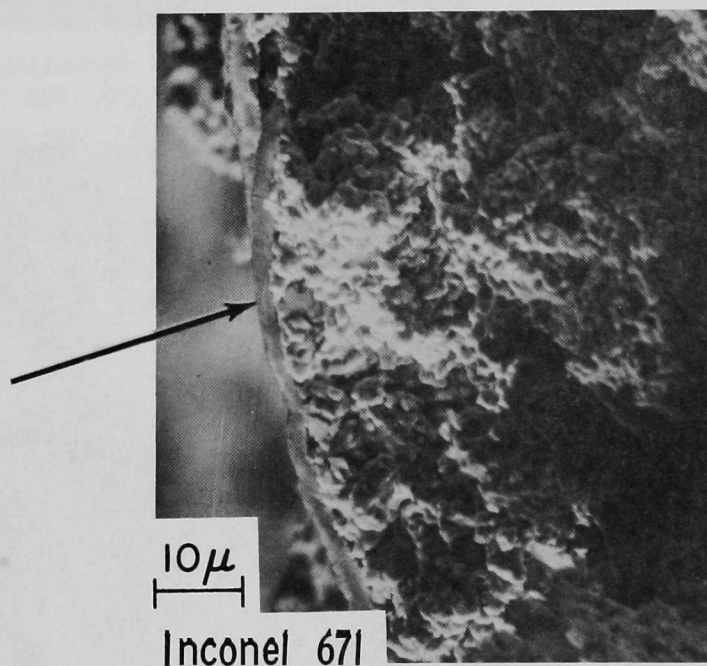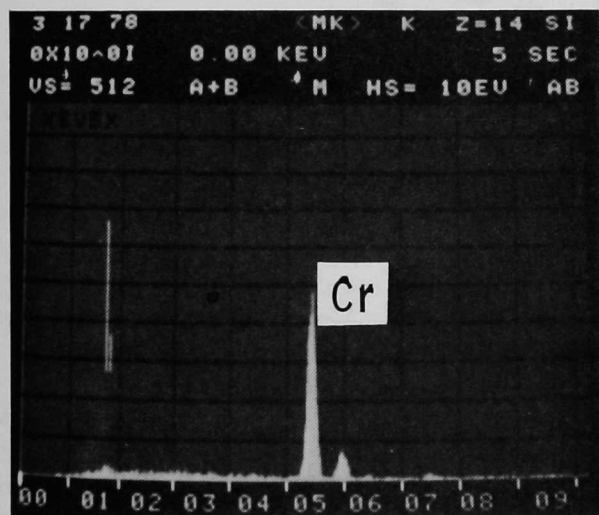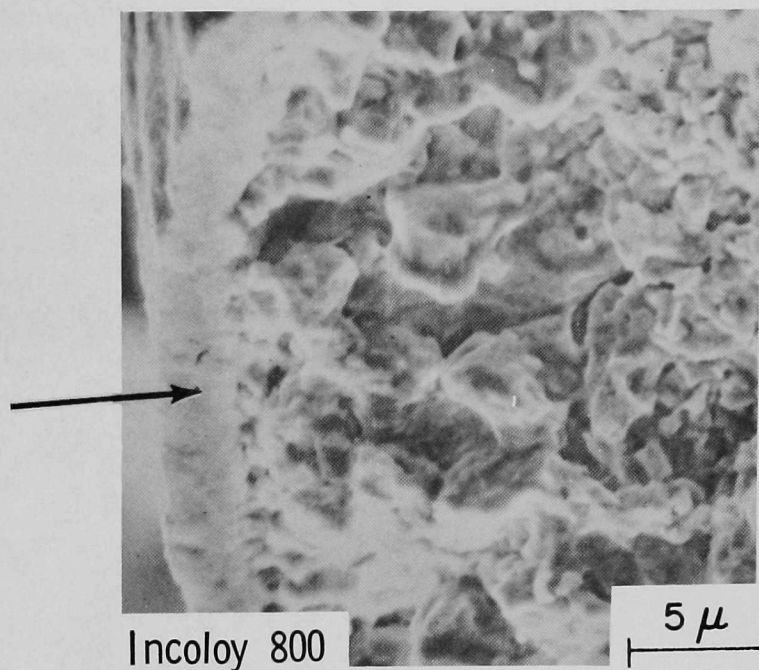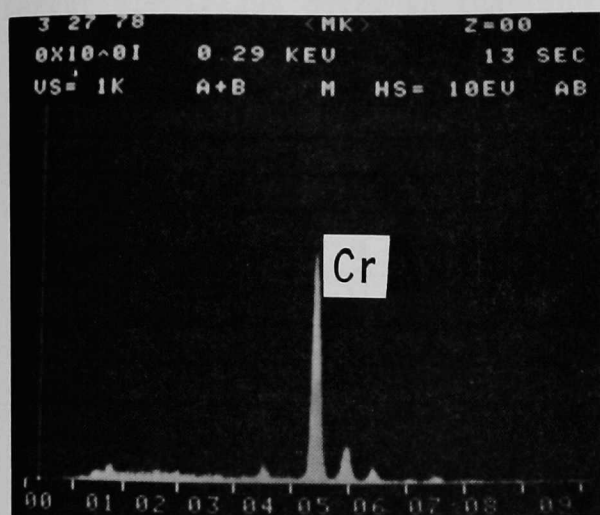
Fig. 44. SEM Photograph of Fracture Surfaces and X-ray Identification of Scales in Incoloy 800 and Inconel 671 Specimens After a 1000-h Exposure to a Complex Gas Mixture at 750°C (Run A01A750). ANL Neg. No. 306-78-341
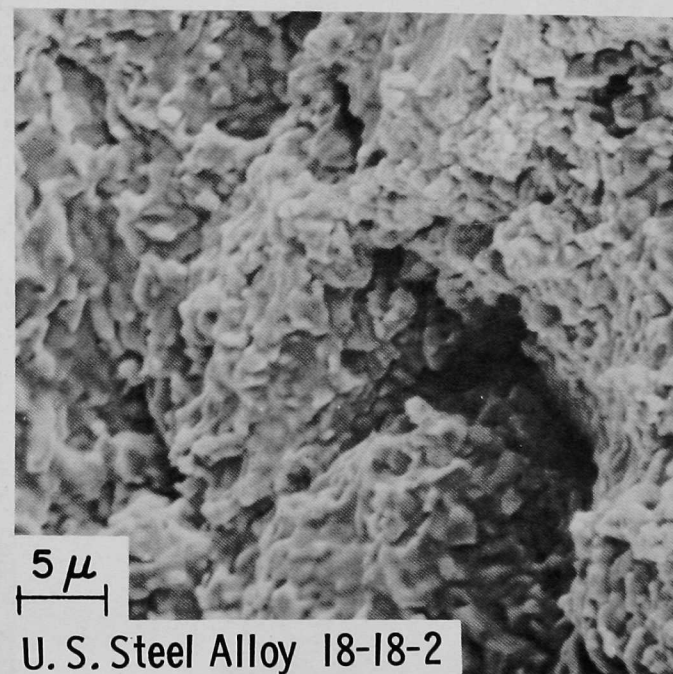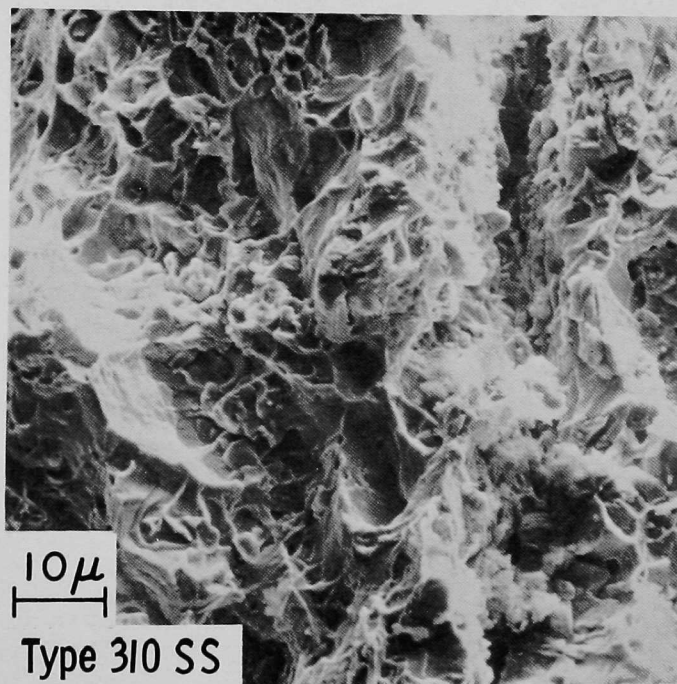
Fig. 45. SEM Photographs of Fracture Surfaces of Type 310 Stainless Steel and U.S. Steel Alloy 18-18-2 After a 1000-h Exposure to a Complex Gas Mixture at 750°C (Run A01A750). Neg. No. ANL-306-78-336

Task E -- <u>Erosion Behavior of Materials in Coal-conversion Processes</u>
       (W.J. Shack and J.Y. Park)

The high-temperature erosion-test apparatus has been assembled and is being checked out and calibrated. It is currently being operated with a transparent plexiglass cover so that the motion of the slinger arm and particles can be directly observed (see Fig. 46).

High-speed motion pictures of the moving particles have been made using the Redlake Hi-cam camera. A high-speed motion picture was taken with a film speed of 1000 frames/s and a rotor speed of 500 r/min. Sequential analysis of the film will give accurate values of particle velocities and trajectories. A detailed analysis of the results will be presented in the next Quarterly Report. These results will be used to correlate rotor speed with particle velocity and the relative angle between the particle trajectory and rotor arm. During the initial testing of the system, large-amplitude vibrations of the shaft and rotor were observed for rotational frequencies > 1450 r/min, and plastic bending of the rotor shaft occurred at 1700 r/min. At a rotational velocity of 1450 r/min, the maximum tangential component of the particle velocity, which is equal to the tip speed of the rotor, is 31 m/s. Even at this velocity, there may be enough vibration to unacceptably shorten the life of the main shaft bearing, and it is desirable to be able to achieve higher velocities. The simplest way to raise the critical frequency of the system is to reduce the mass of the rotor; therefore, new lower-mass rotor designs have been developed. In addition to obtaining higher velocities, it is also desirable to limit the angular dispersion of particles so that the angle of impingement can be accurately controlled.

A low-temperature erosion apparatus, which is also based on the high-speed rotor principle, is available at ANL and is being used to test the new lower-mass rotor designs and to analyze the effect of rotor design on angular dispersion. The angular dispersion can be measured as shown schematically in Fig. 47. A target (aluminum foil is convenient) is mounted on the wall of the apparatus. A mask, also mounted on the wall, permits particles to enter through a narrow slit of width d. The width, D, of the impact area of the particles on the target can be measured. The value of D thus obtained and the geometry of the arm, target, and mask can then be used to calculate the angular dispersion.

The initial concepts for new rotor designs are shown in Figs. 48 and 49. Preliminary versions were fabricated from aluminum and tested in the low-temperature erosion rig. The design shown in Fig. 48 gave an angular dispersion of $\sim \pm 6°$; the alternate design shown in Fig. 49 gave an angular dispersion of $\sim \pm 1°$. The second design was chosen on the basis of these results, and the new rotor for the high-temperature apparatus is being fabricated.

Room-temperature erosion tests were performed on Type 304 ss, 1015 carbon steel, Incoloy 800, Type 310 ss, Alloy 671, and Stellite 6B in the ANL low-temperature rig, using 50-μm Al_2O_3 particles with an impact velocity of 70 m/s and impingement angles of 15°, 20°, 25°, 45°, and 90°. These results are being analyzed and will be presented in the next Quarterly Report. They will represent benchmarks for later calibration and testing of the high-temperature apparatus.

In the next quarter, room-temperature calibration tests of the high-temperature apparatus will be continued and work will begin on the installation of the particle-feeding, environmental control, and heating systems.
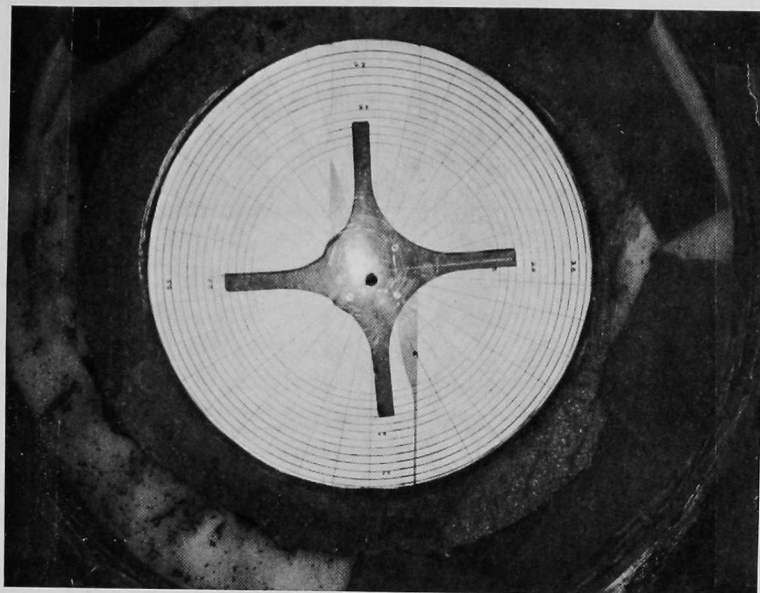
Fig. 46.   Erosion-test Apparatus, Assembled with a
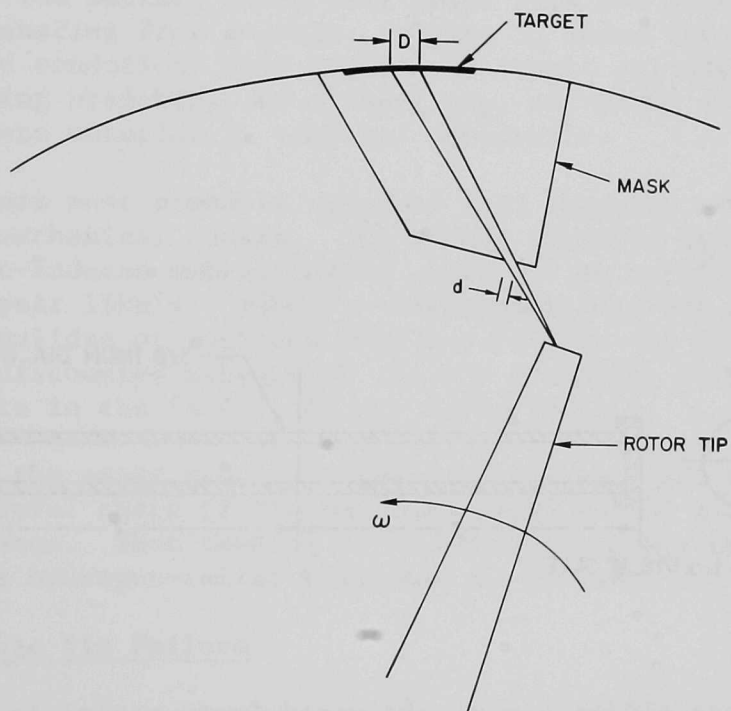Transparent Plexiglass Coverplate for
Calibration

Fig. 47.   Angular Dispersion Analysis of Particles
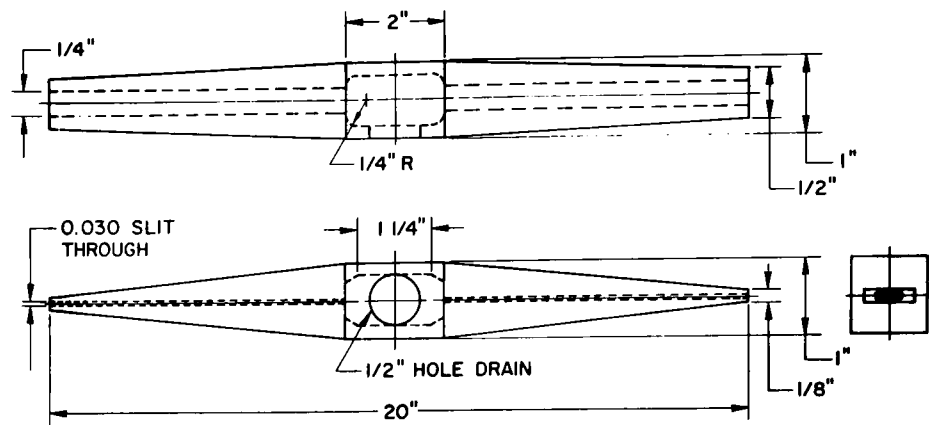Neg. No. ANL-306-78-564

75

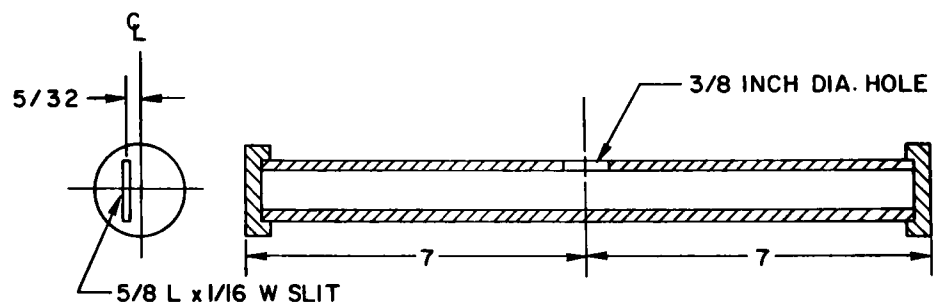Fig. 48.   Schematic of New Rotor Design.   Neg. No.
ANL-306-78-563

Fig. 49.   Schematic of Alternative Rotor Design.   Neg. No.
ANL-306-78-562

Task F -- Component Performance and Failure Analysis (S. Danyluk, G.M. Dragel, W.J. Shack, and J.Y. Park)

The activity during this quarter involved the examination of components from the HYGAS Pilot Plant, the HYGAS Ash Agglomerating Gasifier, and the Grand Forks Energy Research Center.

1. HYGAS Valve Assembly Leaf Spring Failure

A Type 416 stainless steel leaf spring from a three-stage reciprocating compressor failed after 3-5 months of intermittent operation. The total period of service was ∿ 1000 h (∿ 42 days). These helical springs are used in the suction and discharge valve assemblies of the third stage of the compressor, which was used to compress gas usually consisting of H_2, CO and traces of CO_2 and H_2O. Four or five days prior to the failure, the gas consisted of 82-84 mole % H_2, 11-14 mole % CO, and traces of CO_2 and H_2O. The suction temperature was 24°C (75°F) while the discharge temperature was 104°C (219°F). The discharge pressure was 7.2 MPa (1050 psi). After the failure occurred, chemical analysis verified that the leaf spring was of Type 416 stainless steel. However, the measured carbon content was high (0.34 wt %, versus the recommended value of 0.15 wt %). Micro-hardness values showed Vickers' hardness numbers of 540-630 kg/mm^2 both near to and far from the fractured end. The recommended value for hardened and tempered Type 416 stainless steel is 180-360 kg/mm^2.

The leaf spring is shown in Fig. 50; the fracture surface and gouge are evident. In Fig. 51, a more detailed view of the fracture surface and gouged area; pits are also visible at the surface.

An optical micrograph of the spring in the as-received condition is shown in Fig. 52. The surface shows many small pits and surface irregularities. A crack is seen emanating from a gouge. Figure 53 shows this same crack in the polished and etched condition; four additional cracks are also seen. Micrographs of one crack, showing branching and a crack tip, are shown in Fig. 54. The micro-structure of the base material is tempered martensite.

The failure most probably resulted from improper tempering in conjunction with chemical and mechanical causes. Improperly tempered martensite is prone to cracking. Hydrogen-induced embrittlement could not be verified, and hydrogen attack does not appear likely. Electron-microprobe analysis could not verify whether hydrides, halides or sulfides were involved in the failure. Carburization and oxidation are discounted because of the low operating temperature. The role of the observed pits in the failure is not understood.

Although the exact cause for the failure could not be pinpointed, proper tempering and a careful check of the surface finish should minimize the possi-bility of a recurrence. Shot peening or electroplating may be advisable. If the latter is chosen, a hydrogen-relief treatment is advised.

2. HYGAS Hinge Pin Failure

A RA-330 stainless steel hinge pin from a solids-transfer valve, LV-339, was found to be bent, corroded and galled. The valve is immersed in the steam-

oxygen region of the fluidized bed of the gasifier. The hinge pin, which supports a link, is held by two end brackets and is free to rotate. The operating temperature was 1010-1093°C (1850-2000°F); the pressure was 6.9 MPa (1000 psig).

A photograph of the as-received pin is shown in Fig. 55. The diameter is out of round and the pin is bent. Additional photographs of surface pitting and galling are shown in Fig. 56. Considerable damage is evident at the hinge end. The pit depth and galling are also shown in Fig. 57. The galled regions were shiny; this indicates that the pits formed prior to the galling. Grain-boundary penetration (most probably by sulfides) and internal corrosion were also found; these results are shown in Fig. 58. A heavy corrosion scale is seen at the OD, and the grain boundaries and twins are outlined with corrosion product. Confirmation of the nature of the corrosion product is in progress.

This analysis confirms the pilot plant's preliminary finding that the hinge pin had been exposed to excessive loads. The pitting corrosion, at this time in the service life, is not as serious a problem as the overloading. Reduction of the applied loads and replacement of the hinge pin with a harder material are recommended.

3. HYGAS Ash Agglomerating Gasifier Internal Cyclone Failures

a. Type 310 Stainless Steel Cyclone

An internal cyclone wall, of 0.64-cm (0.25-in.)-thick Type 310 stainless steel, was eroded by coal-particle impingement and failed by perforation. The coal-particle velocity was 25-50 m/s (120-160 f/s) and the operating temperature was 927-982°C (1700-1800°F). The total service life was 480 h (20 days). The typical gas composition (mole %) with air/steam was 10 CO, 10 H_2, 8 CO_2, 62 N_2, balance steam; the composition with steam/oxygen was 30 CO, 45 H_2, 15 CO_2 and 10 N_2. The average particle size was 0.0425 cm (40 mesh).

A photograph of the cyclone, showing the particle inlet and the eroded section, is shown in Fig. 59. The perforation occurred at an angle of 20-30° relative to the inlet axis of the cyclone; wall thinning is observed around the perforation. A photograph of the eroded region, as seen through the cyclone inlet, is shown in Fig. 60. The topography of the internal surface appears nonuniform. The eroded regions were sectioned for optical, scanning-electron, and transmission-electron microscopy. A photograph of a polished cross section from the region indicated in Fig. 59 is shown in Fig. 61. The direction of particle impingement is indicated; wall thinning is readily seen.

Photographs of the internal surface and a cross section of the polished and etched region are shown in Fig. 62a and b, respectively. Figure 62a shows ridges that have developed as a result of particles plastically deforming the surface. Figure 62b shows a region made hollow by particle impongement and erosion. The micrograph also reveals grain-boundary precipitates. However, the precipitation apparently did not contribute to the failure.

SEM photographs of the internal surface from an area similar to that shown in Fig. 62 are given in Fig. 63. Ridges due to particle "plowing" are visible in Fig. 63a. Figure 63b shows the termination points of the particle

travel. The ridged areas (tracks) caused by removal of base material by the impinging particles are similar to the ones shown in Fig. 62a. Particle sizes of 0.20-0.30 mm are estimated from the width of the tracks. Corrosion with breakdown of the corrosion scale does not appear to be the principal mechanism for erosion in this case.

b. Cyclone with RA-330 Stainless Steel Insert

An internal cyclone with a 0.64-cm (0.25-in.)-thick insert made of Type RA-330 stainless steel failed due to a combination of erosion and corrosion of the insert. The insert is a patch that was welded into the Type 310 stainless steel cyclone described above after the cyclone had failed due to erosion. Number 182 welding rods, with a nominal composition (wt %) of 67 Ni, 0.05 C, 7.75 Mn, 7.5 Fe, 14 Cr, 0.1 Cu, 0.4 Ti, 1.75 Cl, and 0.5 Si, were used to weld the insert. The cyclone was operated for a total of $\sim$ 288 h ($\sim$ 14 days) at a gas temperature of $\sim$ 816-927°C ($\sim$ 1500-1700°F) before the failure was discovered. During operation, coal-particle sizes ranged from 0 to 0.0425 cm (0-40 mesh), and the average gas velocity at the inlet to the cyclone was 23-27 m/s (75-90 fps). The cyclone was operated with coke and subbituminous coal feed with air, which produced a gas composition (mole %) of 52.1 N_2, 16.0 CO, 9.72 CO_2, 14.34 H_2, 1.0 CH_4, and 6.91 H_2O; and with coke and bituminous coal feed (Illinois No. 6 high-sulfur coal), which produced a gas composition (mole %) of 52.5 N_2, 12.12 CO, 8.45 CO_2, 9.43 H_2, 0.71 CH_4, 0.17 H_2S, and 16.59 H_2O.

Optical micrographs of the internal surface of the insert, and a schematic of the patched cyclone, are shown in Fig. 64. Perforations and a rough, uneven surface are visible. A cross-sectional view of the weld and insert in the polished and etched condition is shown in Fig. 65. The heat-affected-zone (HAZ) adjacent to the weld can be seen. Particle impingement is from the direction indicated and is reflected in the topography of the internal surface. The weld and HAZ are not as severely eroded as the insert material, as shown in Fig. 66 where the HAZ is observed to be protruding beyond the severely eroded region of the insert material. The grain boundaries of the base material are decorated with precipitates, as shown in Fig. 67; however, the precipitation, which results from heat treatment or operation at high temperatures, did not contribute to the failure.

Optical micrographs of the corrosion scale and grain-boundary penetration that had occurred at the ID of the insert are shown in Fig. 68. The corrosion scale in (b) has separated from the base material. This separation, during pilot plant operation, allows the corrosive environment to further attack the base metal.

The RA-330 stainless steel insert failed because of a combination of corrosion and erosion, in contrast to the Type 310 stainless steel failure. The weld used in repairing the cyclone was not as severely affected as the insert material. This is attributed to the positioning of the weld relative to the cyclone inlet axis.

c. Cyclone with Hard-faced Type RA-330 Stainless Steel Insert

An internal cyclone with a 0.64-cm (0.25-in.)-thick insert of Type RA-330 stainless steel hard-faced with a cobalt-based material (a patch welded to repair the two previous failures described above) failed due to erosion-corrosion of the

weld region. The weld, made with a No. 182 welding rod, was more severely affected than the base material because of its position relative to the cyclone inlet axis. The cyclone was operated for a total of $\sim$ 32 h before the failure was discovered, with particle sizes of up to 0.0425 cm (40 mesh), a gas velocity at the cyclone inlet of 23 to 27 m/s (75 to 90 fps) and a gas temperature of 927°C ($\sim$ 1700°F). Coke and bituminous coal feed were used and produced a gas composition (mole %) of 46.3 N_2, 20.4 CO, 8.38 CO_2, 18.6 H_2, 1.72 CH_4, 4.3 H_2O, and 0.26 H_2S.

Optical photographs of a portion of the insert are shown in Fig. 69. Figure 69a is an overall view, while (b) and (c) are higher magnifications of two selected areas. The perforations occurred in the weld region (Fig. 69b); surface roughening of the weld is visible in Fig. 69c. A photograph of a polished and etched cross section of the insert is shown in Fig. 70. A heavy corrosion scale is visible at the weld, while the insert is relatively free from corrosion and erosion.

The cobalt hardfacing is shown in cross section in Fig. 71. The microstructure consists of precipitates and a grain-boundary eutectic phase. The interface between the hardfacing and the substrate shows recrystallized base material. A higher-magnification micrograph of the microstructure of the coating and the interface between the coating and substrate is shown in Fig. 72. The microstructure of the coating is similar in appearance to iron-base alloys that contain ferrite and pearlite. Carbides have precipitated to the grain boundaries of the substrate, probably when the hardfacing was deposited. The precipitation did not apparently affect the erosion resistance of the insert.

A composite cross section of the coating is shown in Fig. 73. This figure indicates that the coating thickness was not uniform over the internal surface of the insert.

The two micrographs in Fig. 74 show cracking in the base metal near the coating-substrate interface (a) and corrosion and grain-boundary sulfide formation near the weld (b). Both these phenomena will contribute to the degradation of the insert.

The failure of the RA-330 hard-faced insert is due to erosion and corrosion of the weld metal itself. Fusion-line cracking was not observed in the section examined, and carbide precipitation did not apparently contribute to a decrease in the resistance to erosion-corrosion. The hard-faced ID of the insert withstood the erosion very well.

4.   Grand Forks Energy Research Center Taphole Cooling Coil Failure

A 0.64-cm (0.25-in.)-OD Hastelloy G cooling coil that carries water and is used in controlling slag flow in the Grand Forks Energy Research Center Gasifier developed a leaking intergranular crack and large hole. The inlet water temperature is $\sim$ 27°C ($\sim$ 80°F) while the outlet temperature is $\sim$ 93°C ($\sim$ 200°F). The temperature in the combustion zone ranges from 482 to 2132°C (900 to 2250°F). The crack initiated at the OD where slag is solidified. The temperature at the OD of the cooling coil is unknown. The cracking is attributed to stress corrosion

80

(IGSCC) caused by sensitization (precipitate or solute segregation to the grain boundaries) and by residual and thermal stresses.

A schematic of the slagging fixed-bed gasifier with an enlarged view of the hearth (just below the oxygen-steam tuyeres) and slag-flow control system is shown in Fig. 75. The water-cooled taphole is formed to assume the proper shape at the pilot plant. Optical photographs of the tube, including a cross section through its center portion, are shown in Fig. 76. The circumference is out of round, and consequently the tube is severely cold worked. A cross section of the tube at higher magnification is shown in Fig. 77. Surface imperfections and localized corrosion at the OD are clearly visible. These regions most probably were the initiation sites for the crack. A polished and etched cross section of the tube, containing an intergranular crack that had initiated at the OD, is shown in Fig. 78. The crack had penetrated ∿ 50% of the wall thickness in this region. A higher magnification micrograph of this crack is shown in Fig. 79. The crack proceeds from the OD to the ID along grain boundaries that apparently contain precipitates.

Scanning-electron micrographs of a fracture surface are shown in Fig. 80. The fracture surface in Fig. 80a contains circular depressions along which the crack propagated. These depressions were also visible at the outer surface; Fig. 80b shows several such depressions that contain a nonconducting phase. X-ray fluorescence spectroscopy showed that this phase contained the elements Mg, Si, Ca, S, and Cu.

The failure of the Hastelloy G tube is attributed to IGSCC. From discussions with Cabot Corporation personnel, it was concluded that the alloy Hastelloy C-276 would be more resistant to IGSCC, especially since the tube is cold worked and exposed to a sulfur environment.
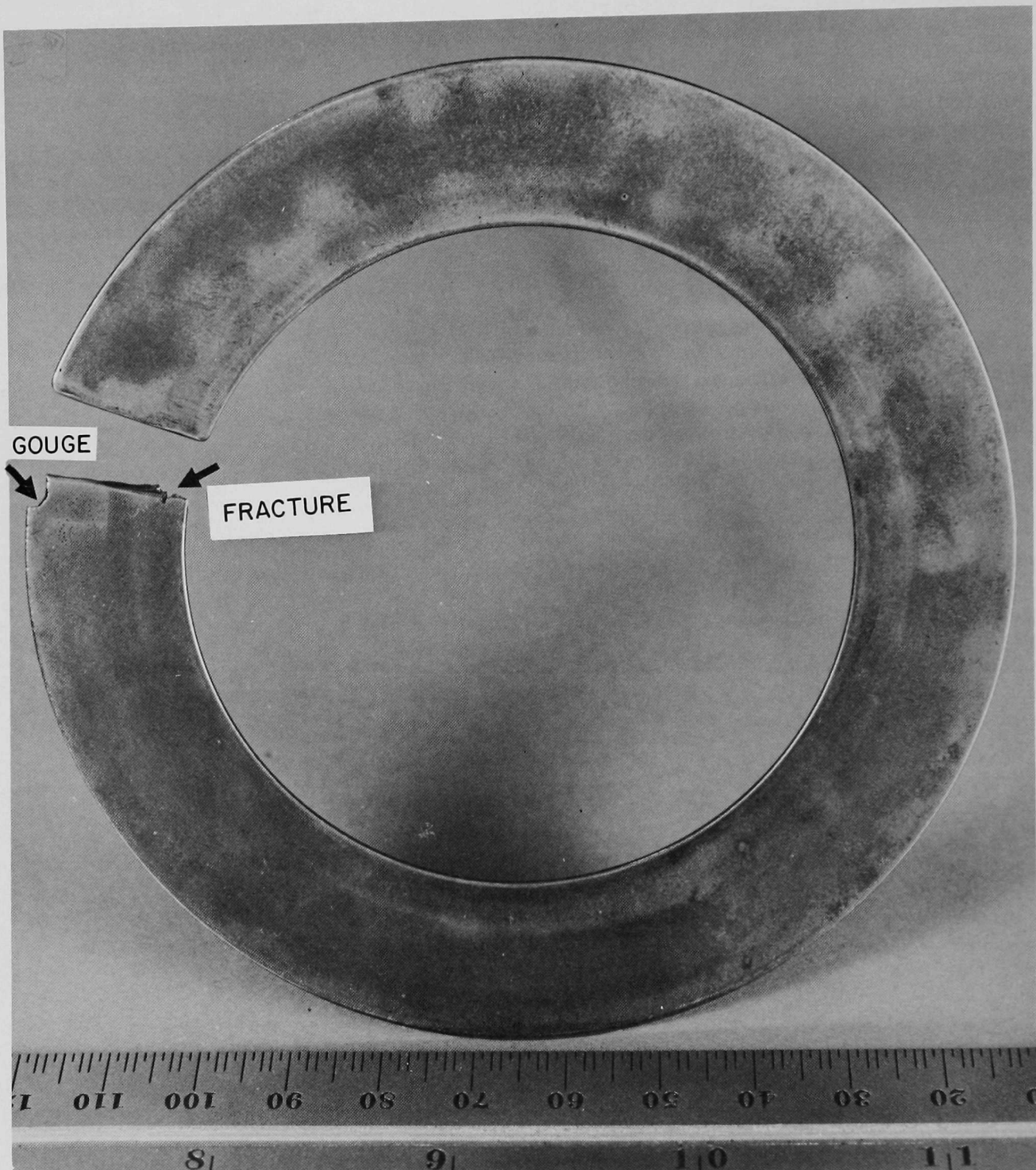
Fig. 50. HYGAS Valve Assembly Leaf Spring. The spring is helical and the fracture surface and gouge are readily visible. ANL Neg. No. 306-77-546

Fig. 51. Enlarged View of Fracture Surface and Gouged Area of HYGAS Valve
Assembly Leaf Spring. ANL Neg. No. 306-77-547
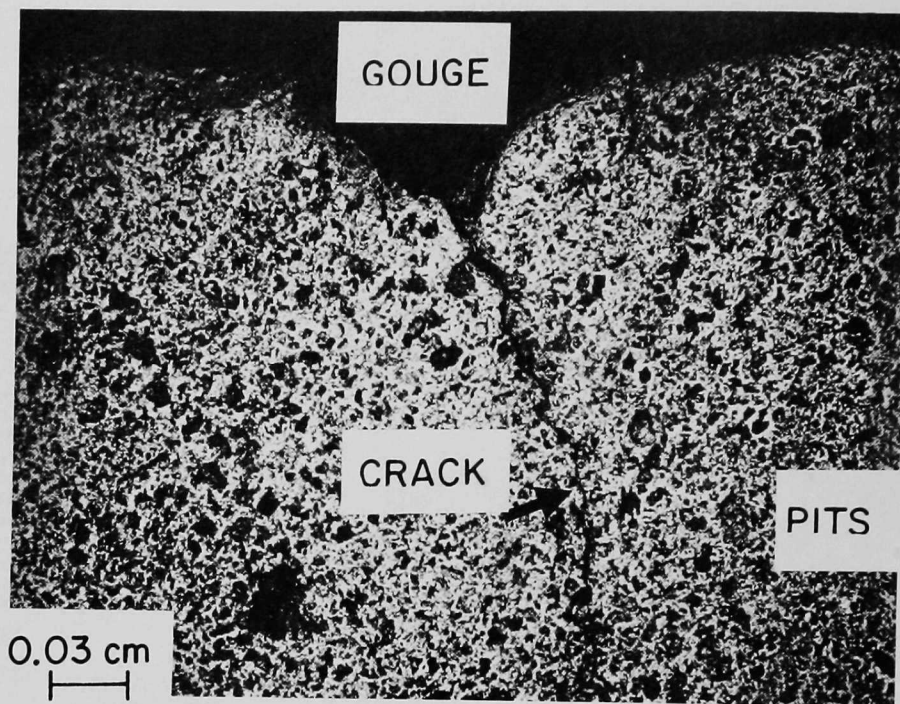
Fig. 52. Top Surface of HYGAS Valve Assembly Leaf Spring, in the As-received
Condition. A crack is emanating from a gouge. Neg. No. ANL-306-78-580
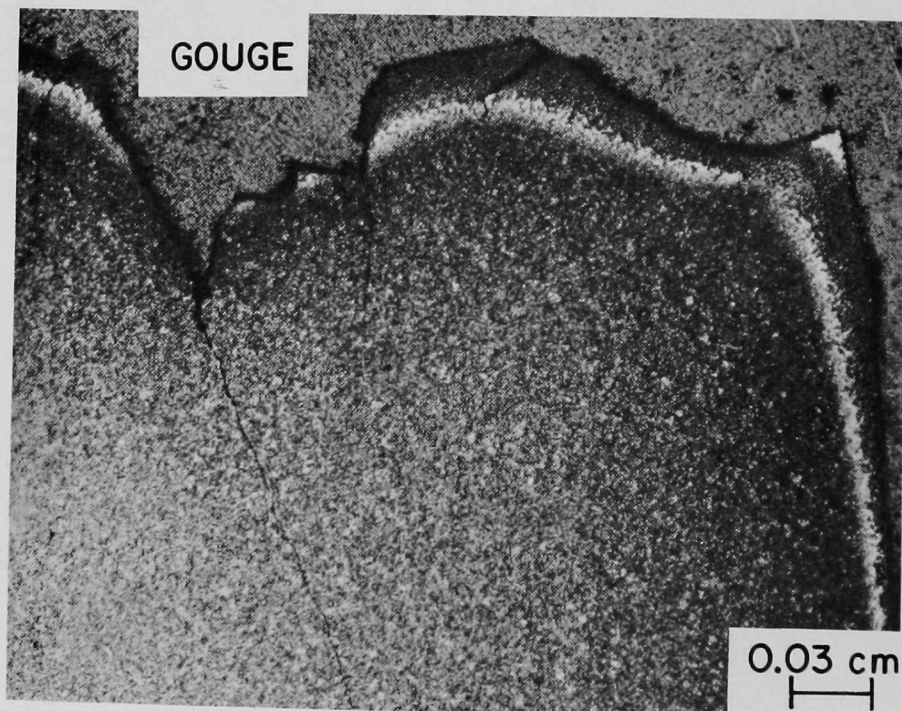
Fig. 53. Polished and Etched Surface of HYGAS Valve Assembly Leaf Spring,
Showing Cracks Originating in a Gouged Region. Neg. No. ANL-306-78-574

(a)

BRANCHING CRACKS

0.02 mm

0.02 mm

(b)
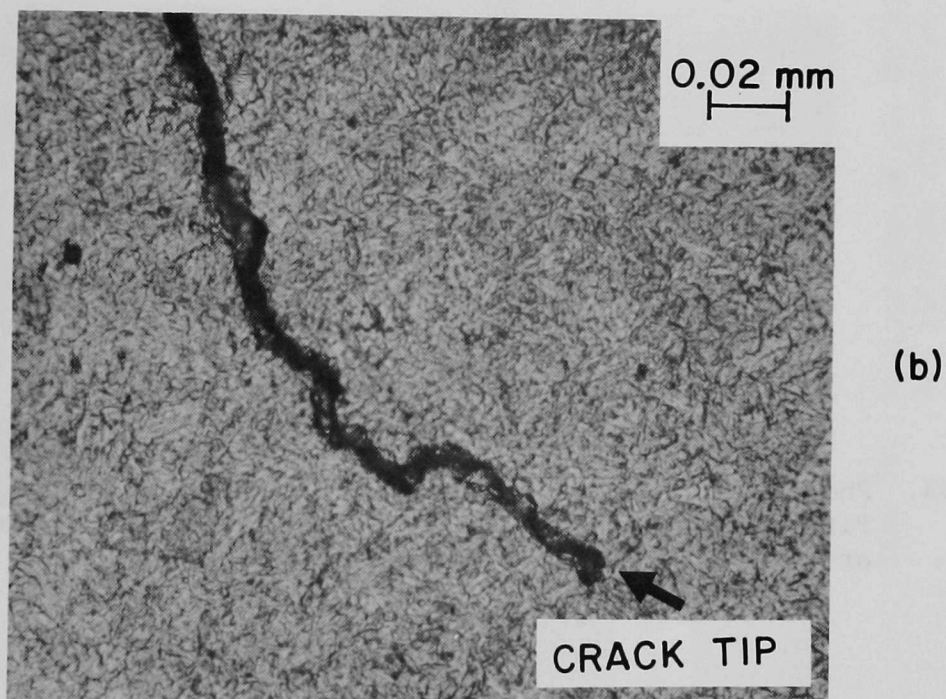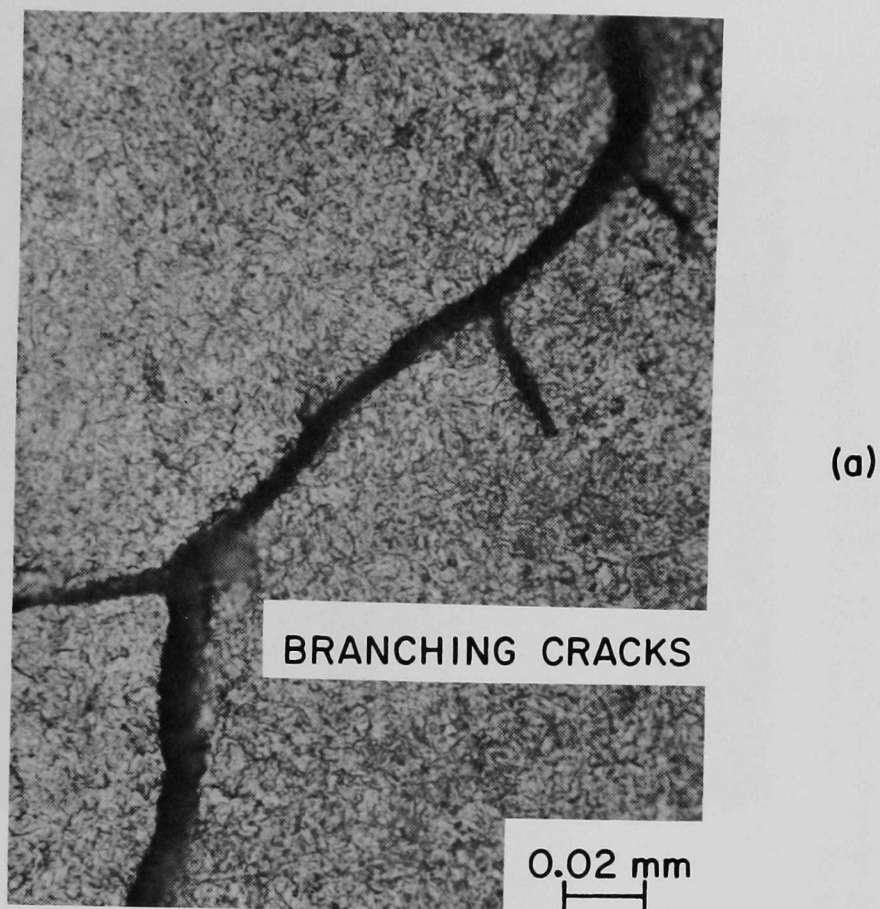
CRACK TIP

Fig. 54. HYGAS Valve Assembly Leaf Spring Cracks. Branched cracks are shown
in (a) and the crack tip is shown in (b). The microstructure is
tempered martensite. Neg. No. ANL-306-78-583
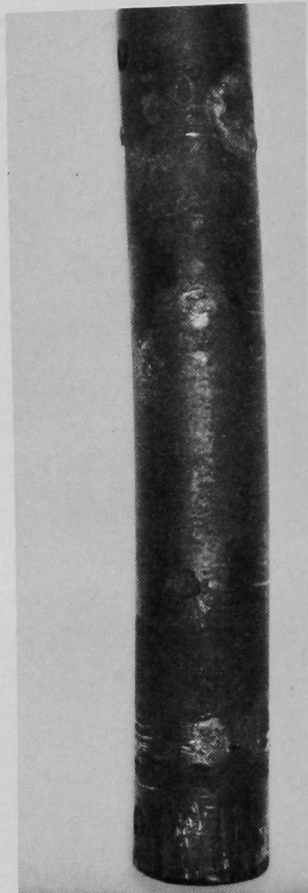
1.8 cm

⊢——⊣

Fig. 55. Photograph of HYGAS Hinge Pin IGT-77-D. The pin is bent.
Pitting is seen along its length and abrasion and galling
are visible at one end. Neg. No. ANL-306-78-592
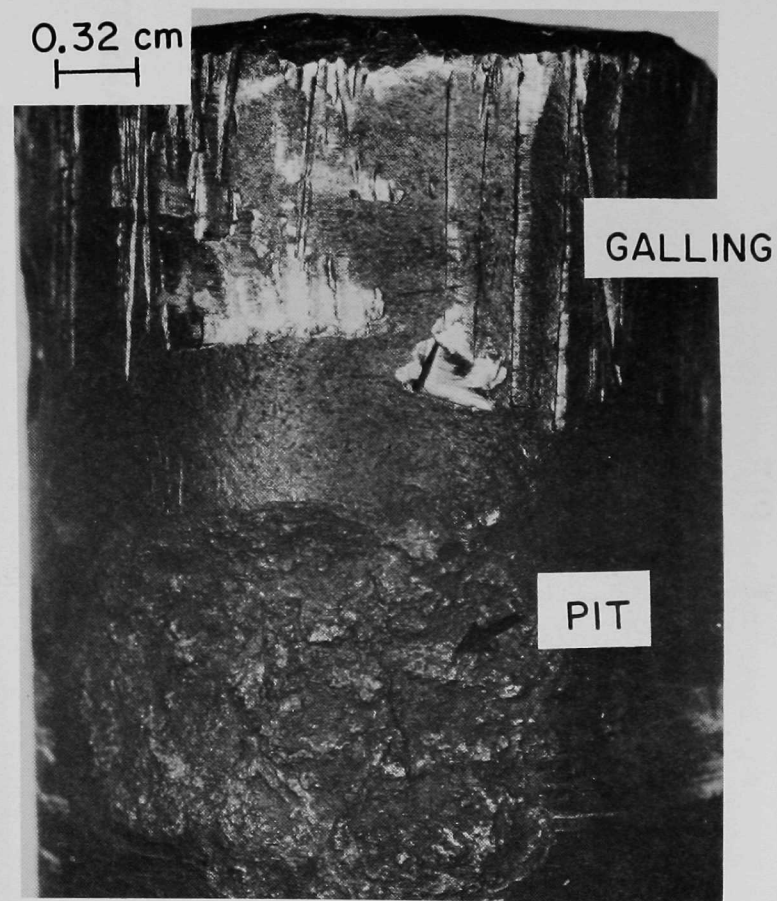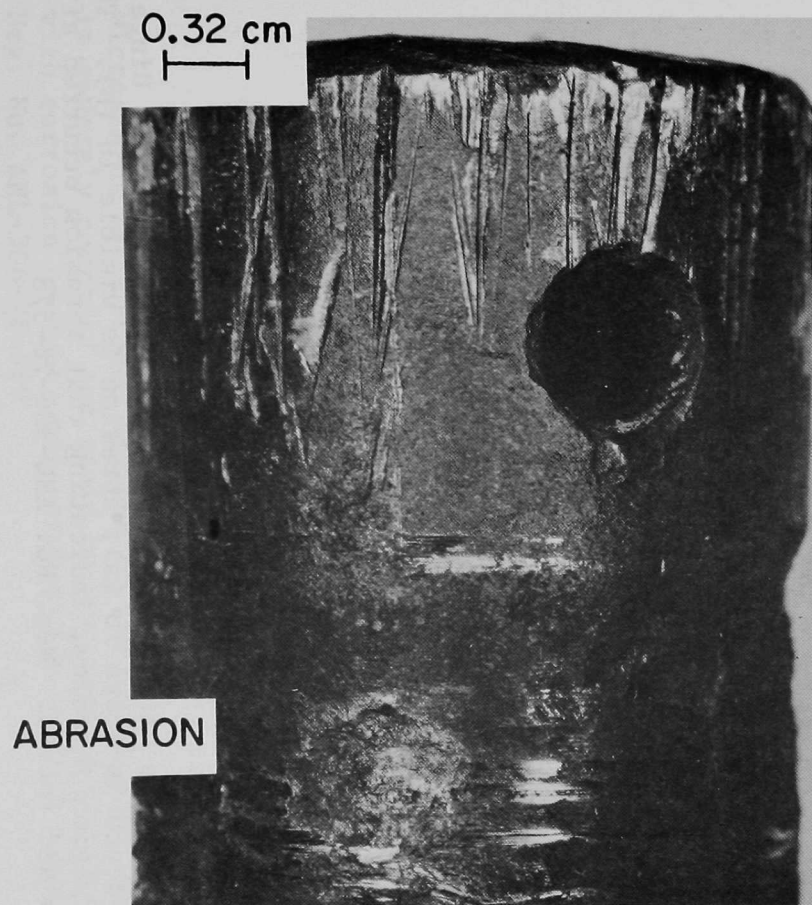
Fig. 56. Photographs of the HYGAS Hinge Pin. Pitting corrosion, galling, and abrasion are visible. The abraded region is shiny. Neg. No. ANL-306-78-568

87
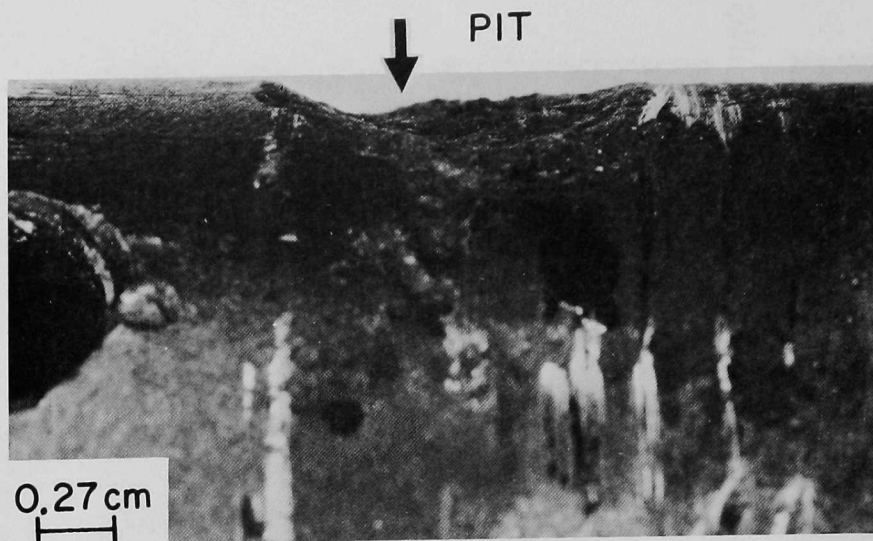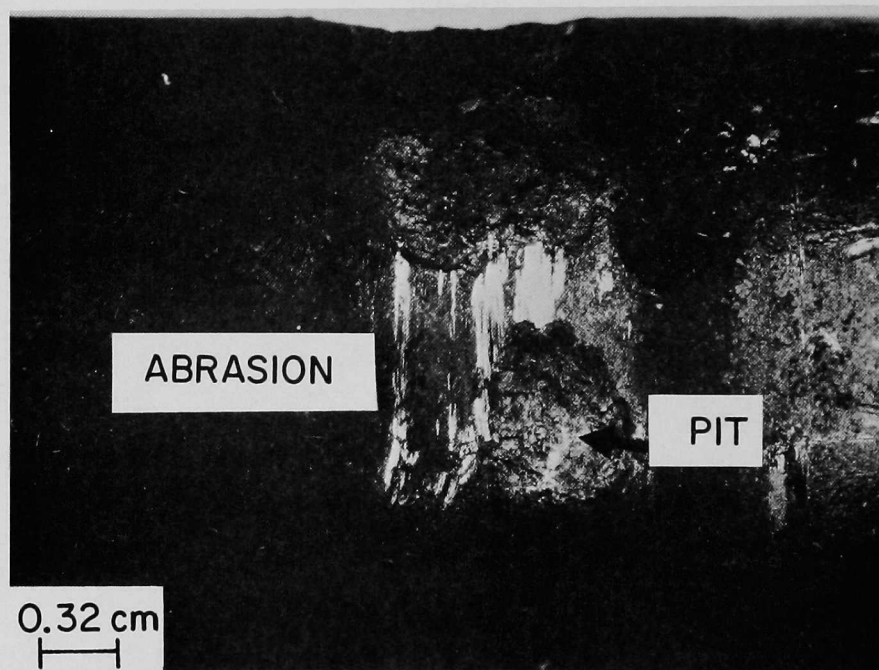
Fig. 57. Photographs of a Pit and An Abraded Region of the HYGAS Hinge Pin. The pit depth is shown in (a); abrasion is visible in (b). The abraded region is shiny, indicating that abrasion occurred after the pits had formed. Neg. No. ANL-306-78-578
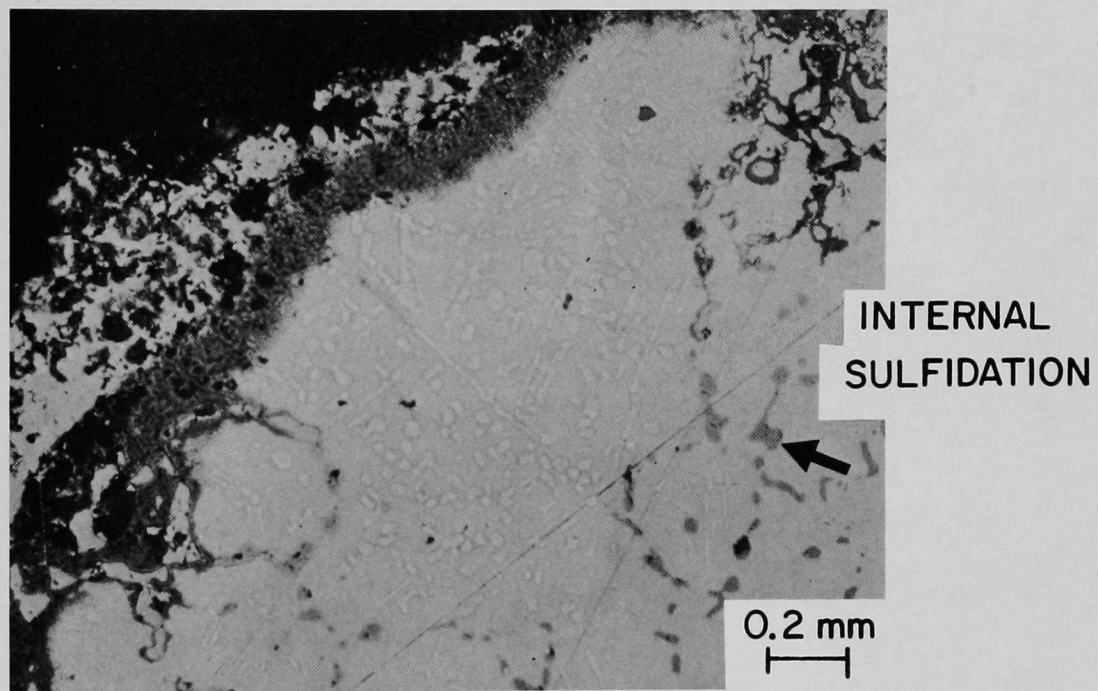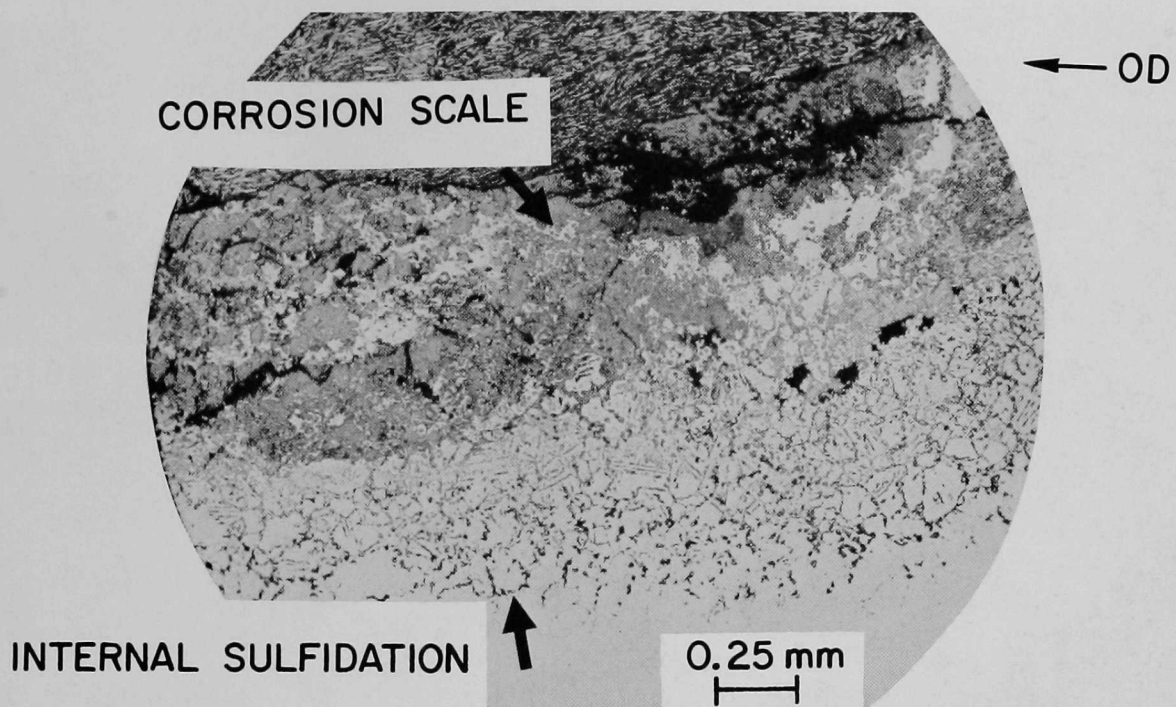
Fig. 58. Micrographs of Corroded Regions of the HYGAS Hinge Pin. The OD
is severely corroded and grain boundaries and twins are outlined
with corrosion product, most probably a sulfide phase.
Neg. No. ANL-306-78-569
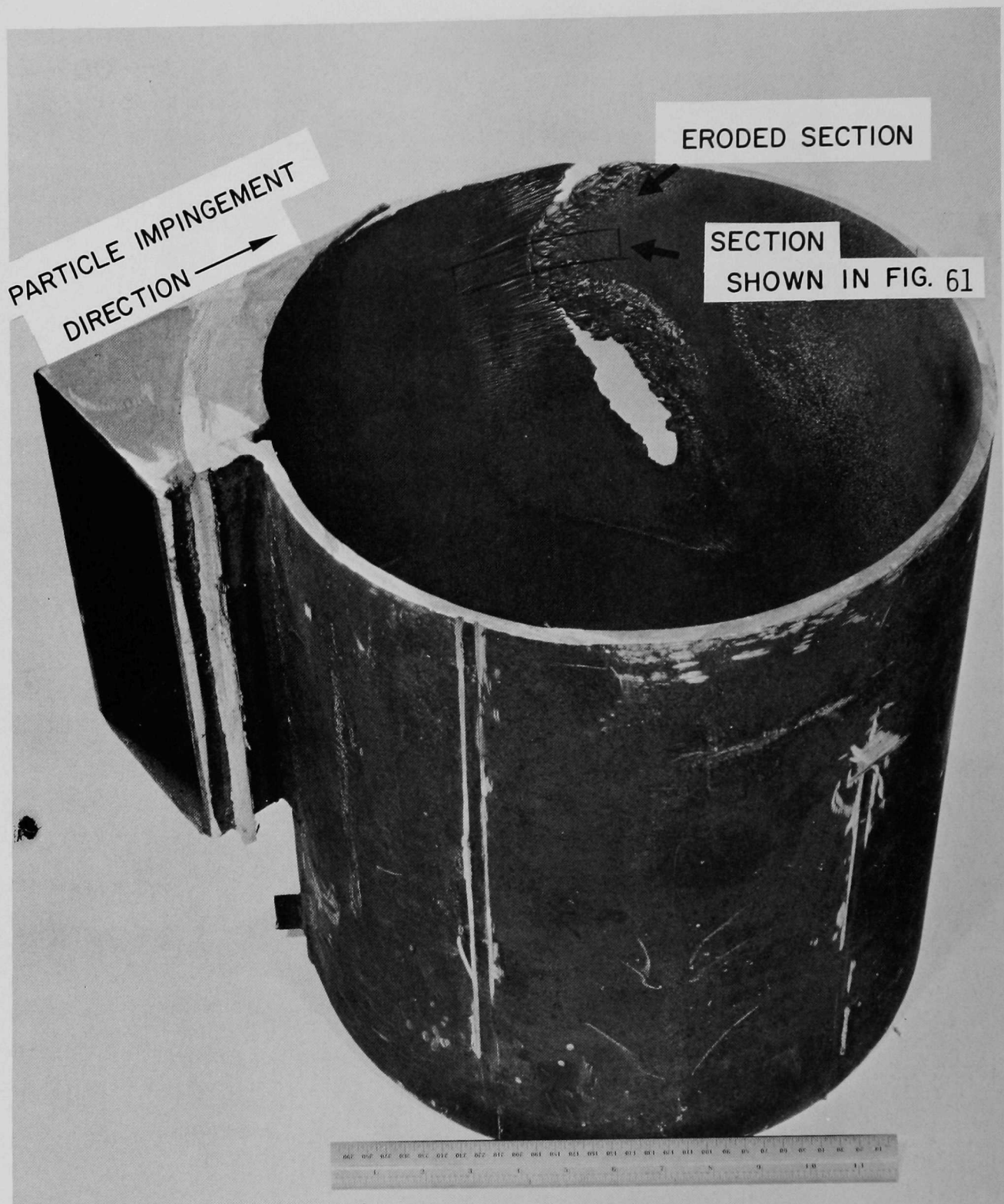
Fig. 59. Photograph of the Type 310 Stainless Steel Internal Cyclone. The
          particle impingement direction and the eroded section are indicated.
          ANL Neg. No. 306-77-543

MATERIAL BUILDUP
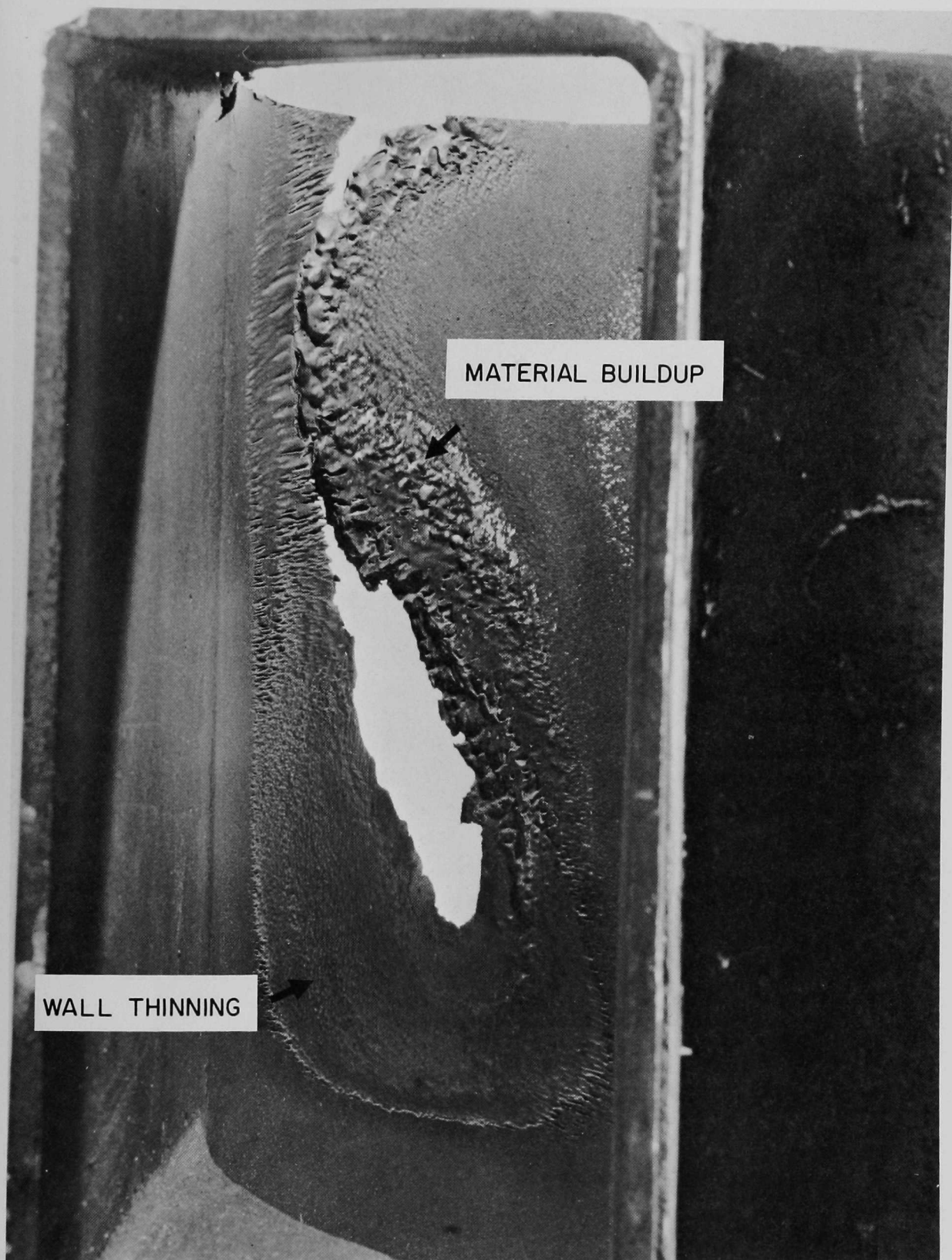
WALL THINNING

Fig. 60. Photograph of the Eroded Region of the Internal Cyclone. The view is through the particle inlet section. Wall thinning is seen at the near section and material buildup is seen at the far section of the perforation. ANL Neg. No. 306-77-541

PARTICLE DIRECTION

0.26 cm
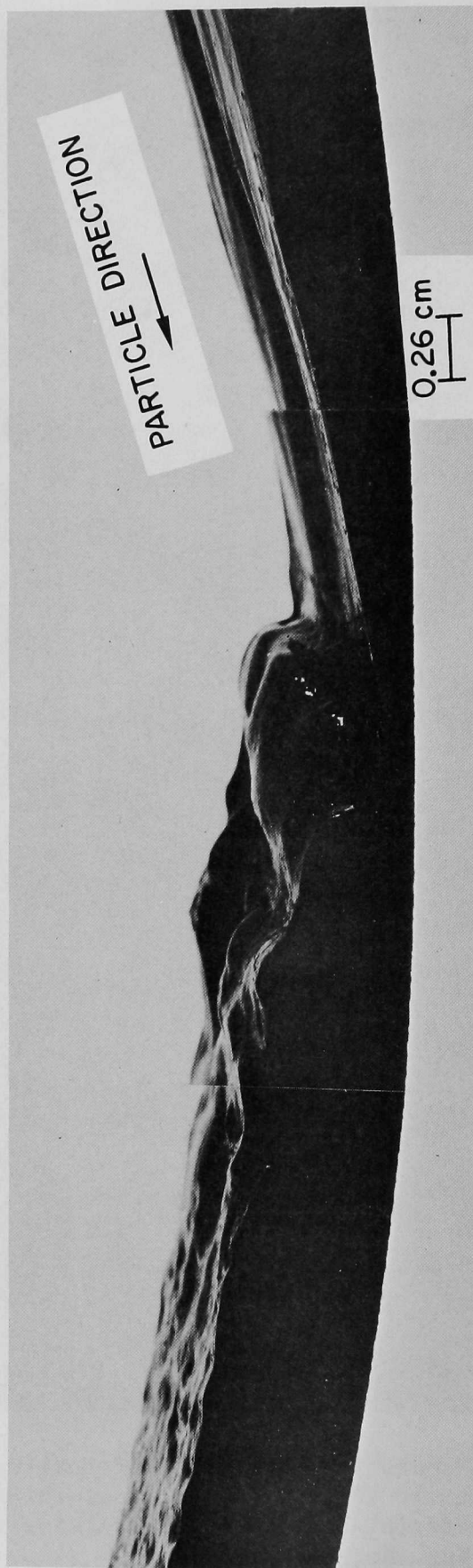
Fig. 61. Photograph of a Polished Cross Section from the Region Indicated in
Fig. 59. Thinning of the wall is readily seen. ANL Neg. No. 306-78-579
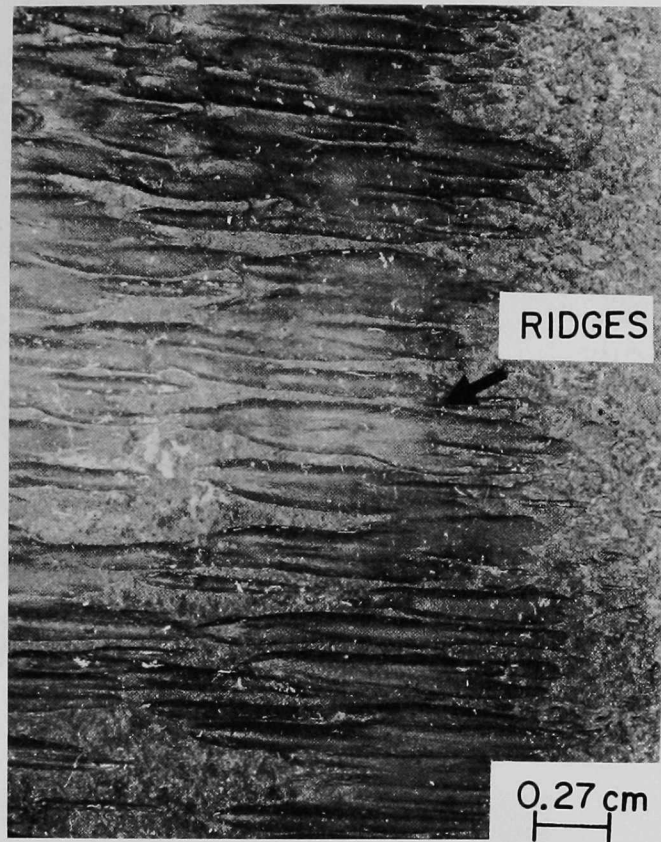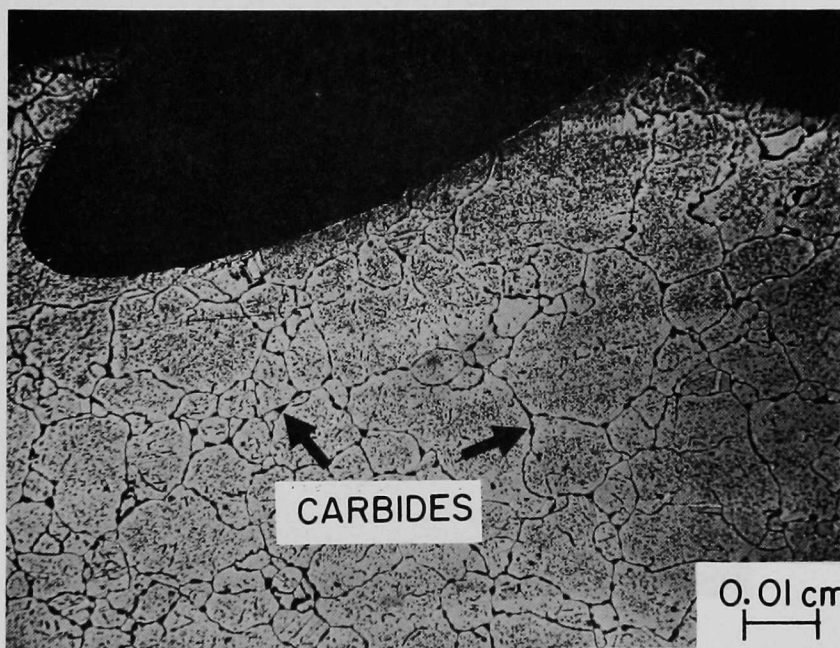
Fig. 62. Photographs of the Internal Surface (a) and a Cross Section (b) of the Cyclone. The ridges in (a) were formed by the impinging particles. The hollow region in (b) was caused by particle bombardment. Sensitization of the steel (carbide precipitation at the grain boundaries) is also visible in (b). ANL Neg. No. 306-78-581
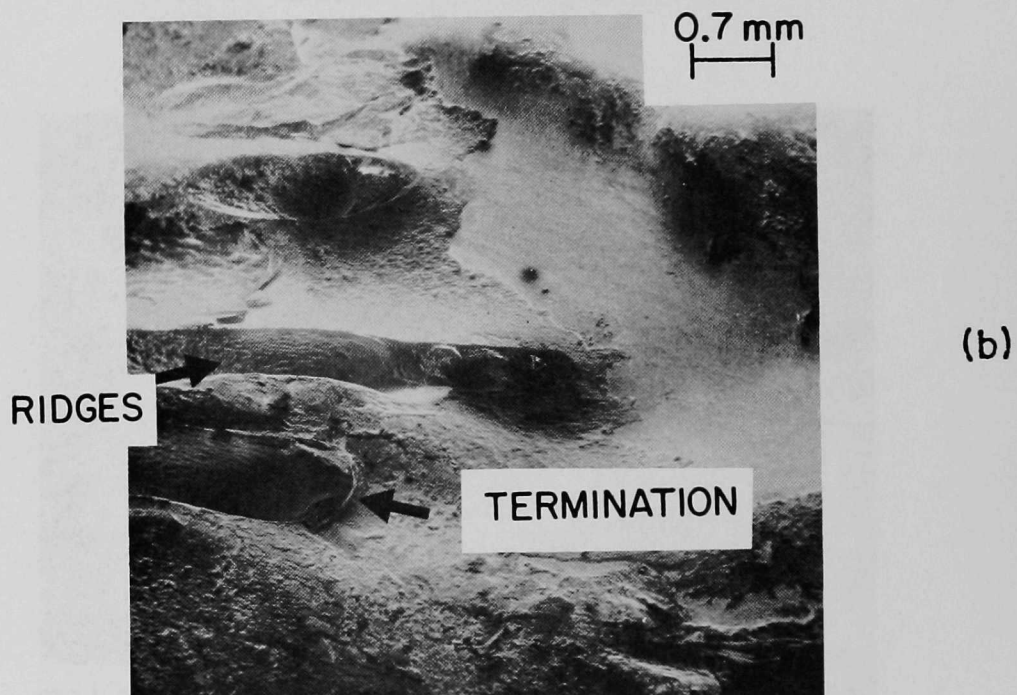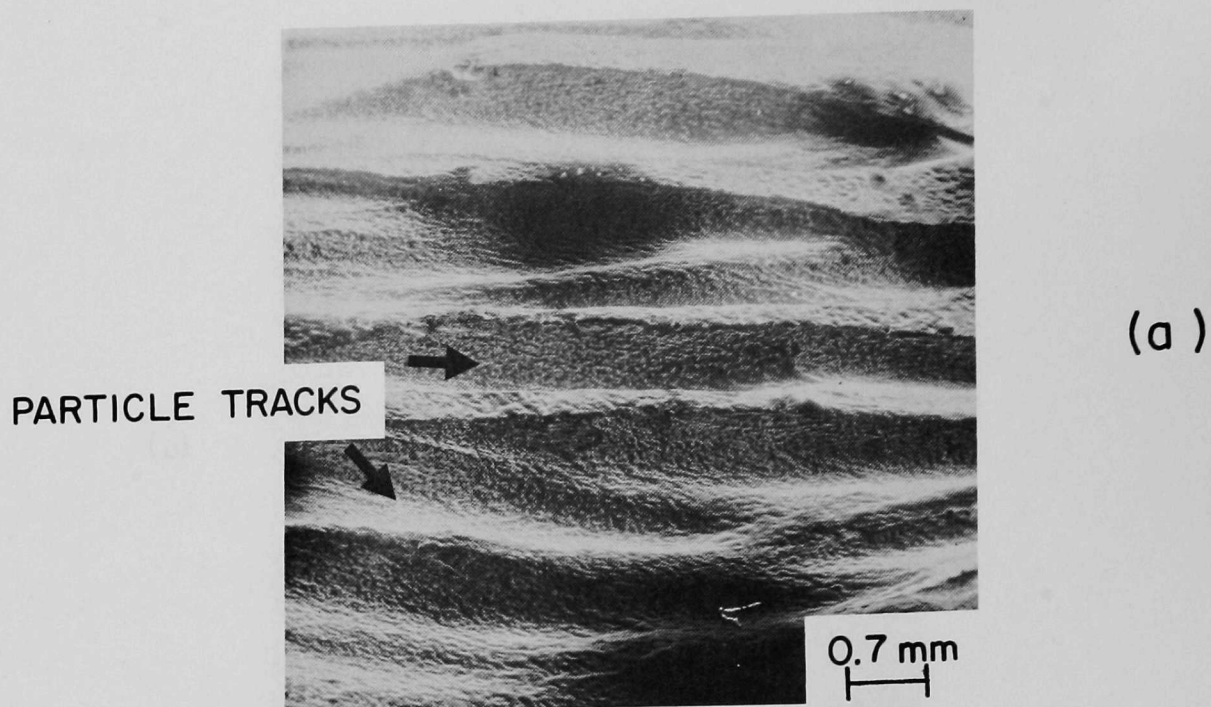
Fig. 63. Scanning-electron Micrographs of the Eroded Surface. Ridges in
(a) are caused by particle deformation of the surface. The micrograph
in (b) shows the termination points of particle trajectories.
Neg. No. ANL-306-78-582
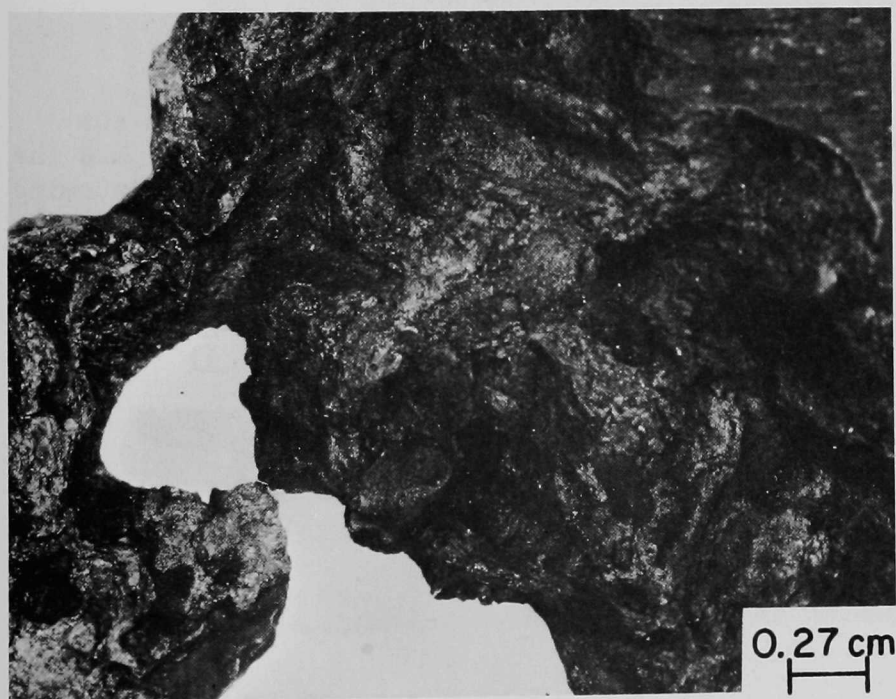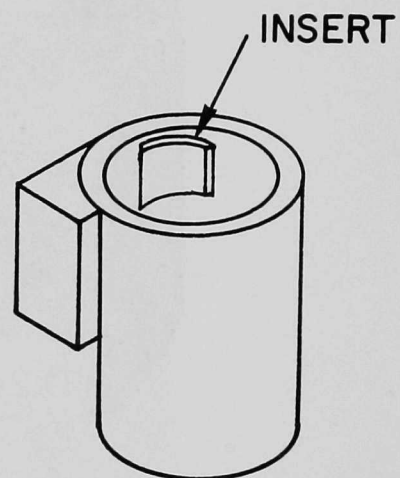
Fig. 64. Optical Micrographs of the Eroded Stainless Steel Insert and a Schematic of the HYGAS Low-Btu Internal Cyclone. Neg. No. ANL-306-78-573
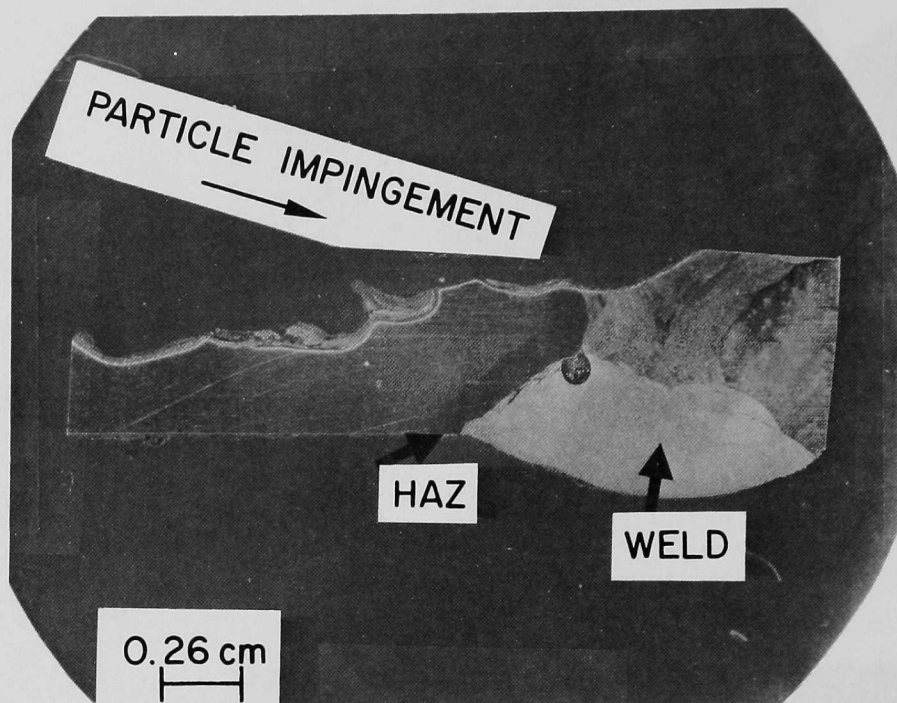
Fig. 65. Cross-sectional View of the Eroded Stainless Steel Insert in the Polished and Etched Condition. The heat-affected zone (HAZ) and the weld are readily seen. The surface topography reflects the incoming particle trajectories. Neg. No. ANL-306-78-570
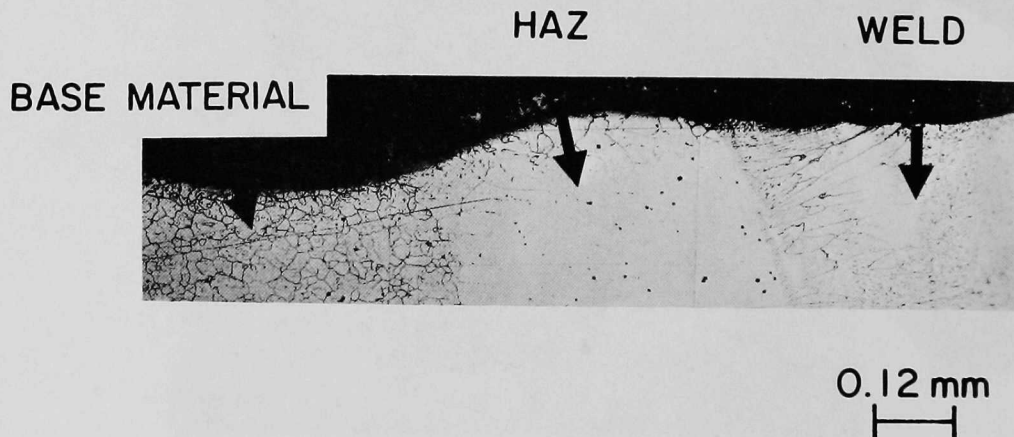
Fig. 66. The HAZ and Stainless Steel Insert at the ID. The HAZ has not eroded to the same extent as the insert material. Neg. No. ANL-306-78-591
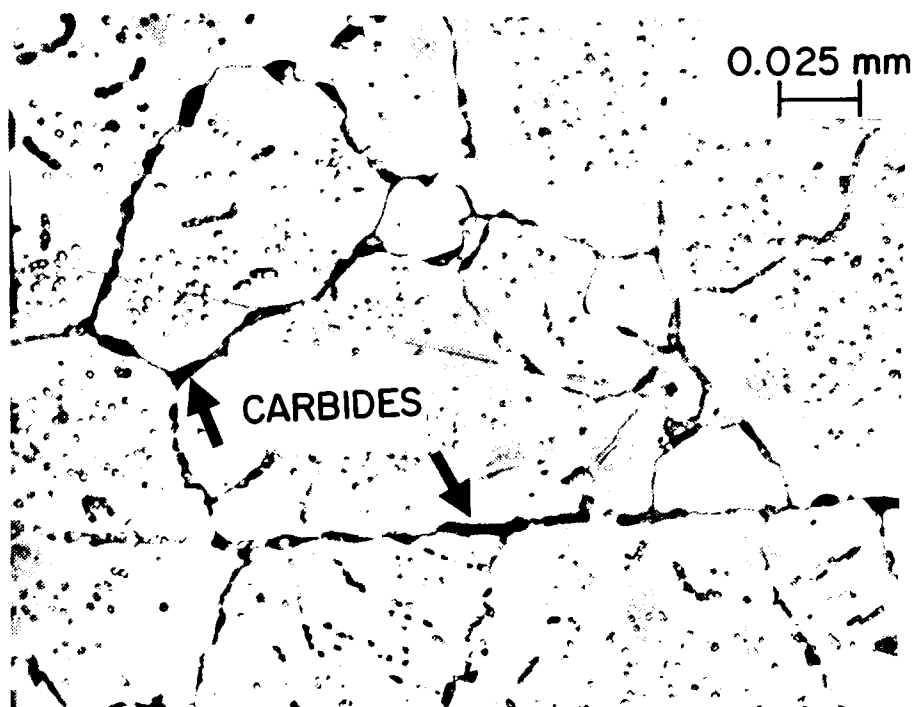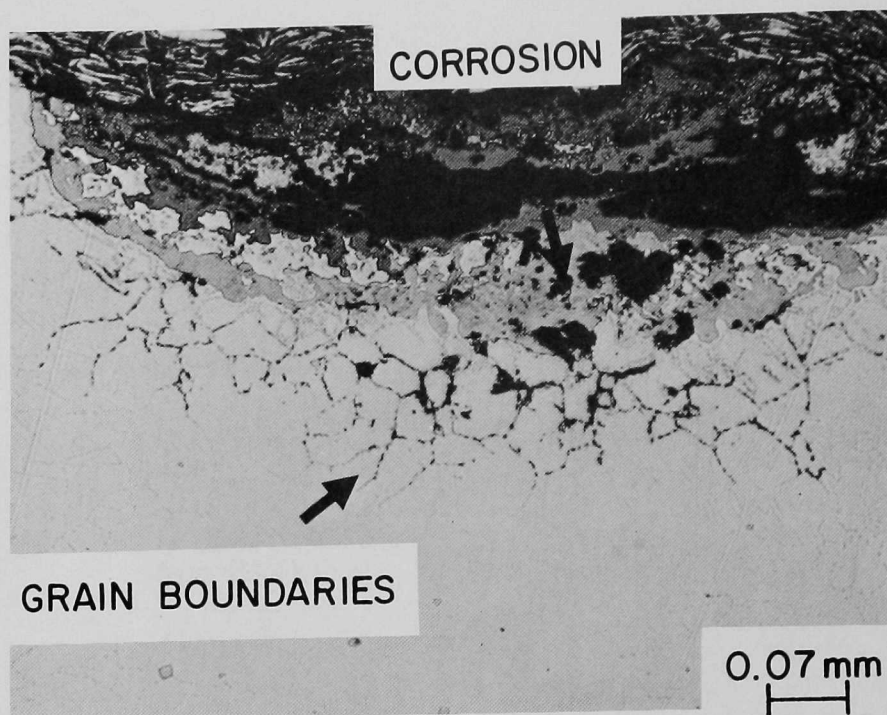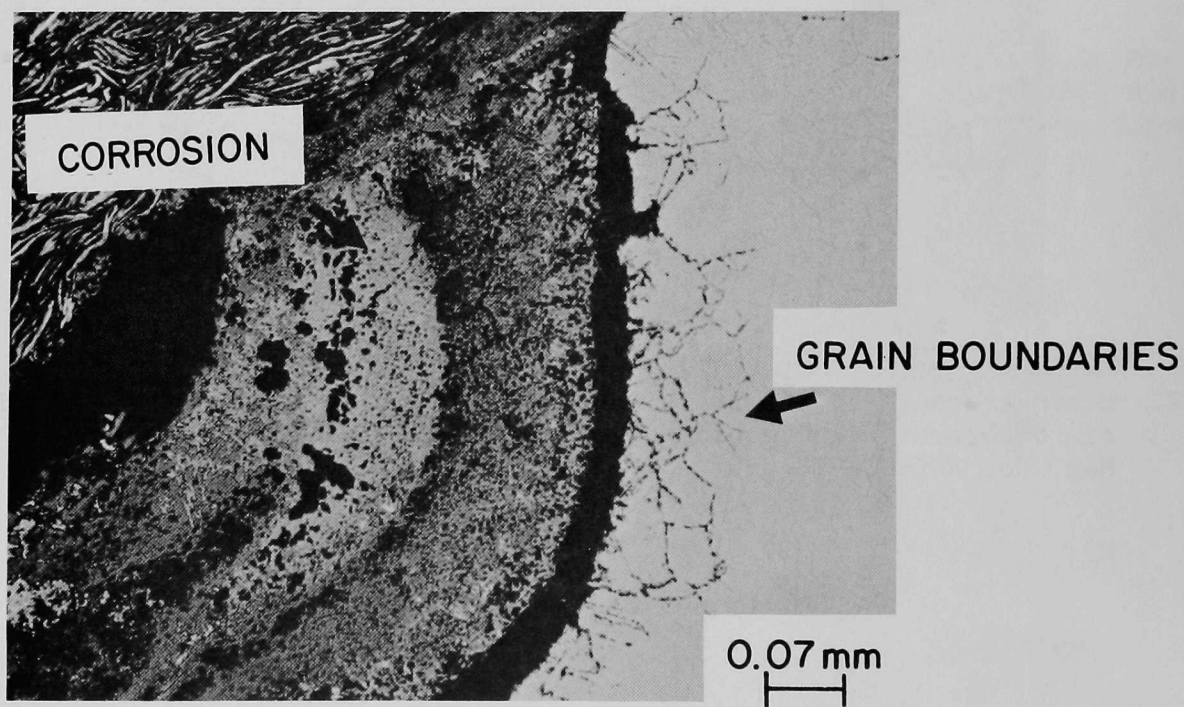
Fig. 67. Microstructure of the Stainless Steel Insert Material. Grain boundaries
are decorated with carbides as a result of sensitization.
Neg. No. ANL-306-78-590

CORROSION

GRAIN BOUNDARIES

0.07 mm

(a)

CORROSION

GRAIN BOUNDARIES

0.07 mm

(b)

Fig. 68. Corrosion at the ID of the Stainless Steel Insert. The grain boundaries are embrittled, probably by sulfides. Neg. No. ANL-306-78-589
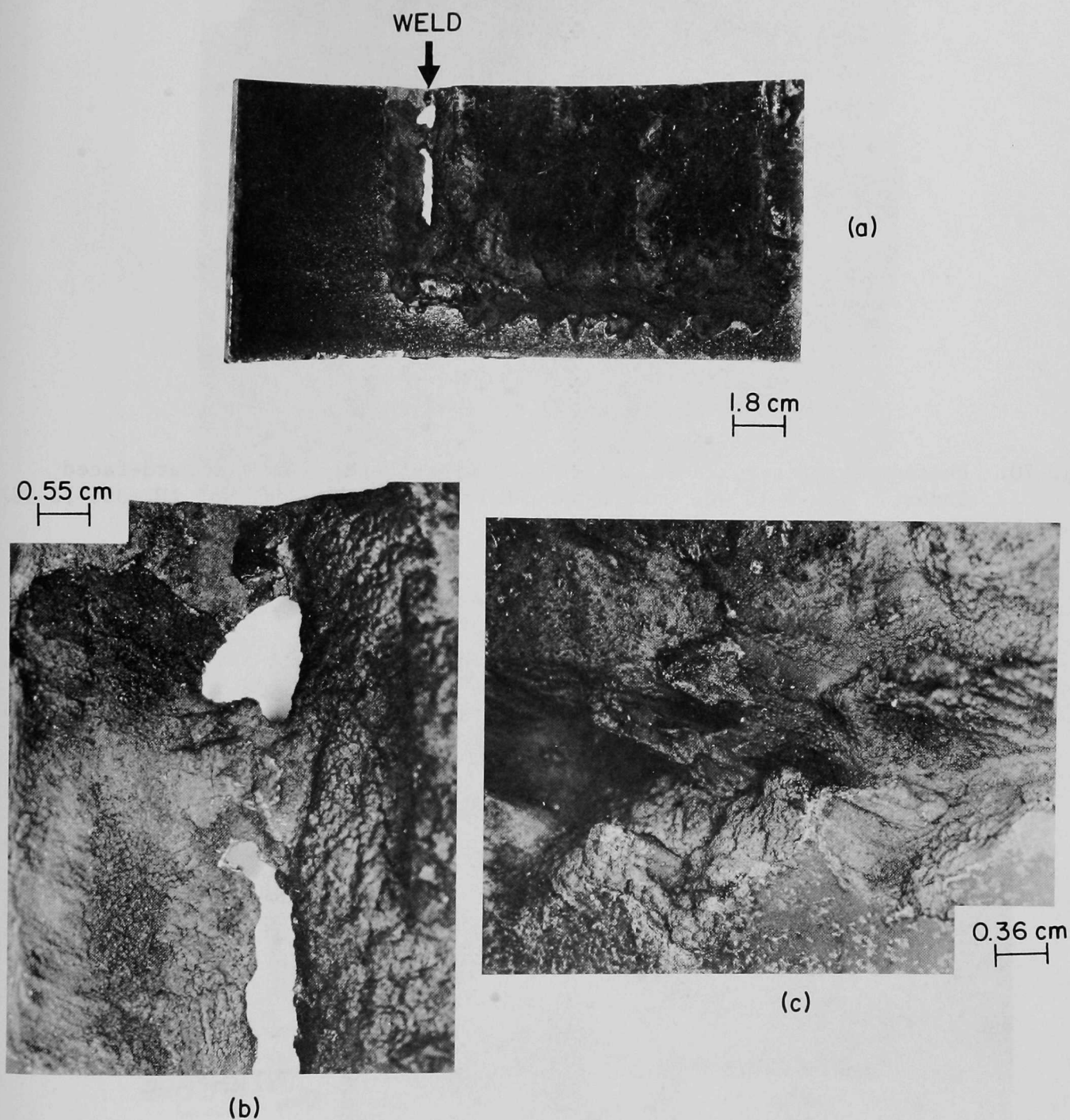
Fig. 69. Optical Photograph of a Portion of a Cobalt-based Hard-faced Cyclone Insert (a); Higher Magnifications of Two Selected Regions (b) and (c). Perforations occurred in the weld region, which was the most severely affected. ANL Neg. No. 306-78-588
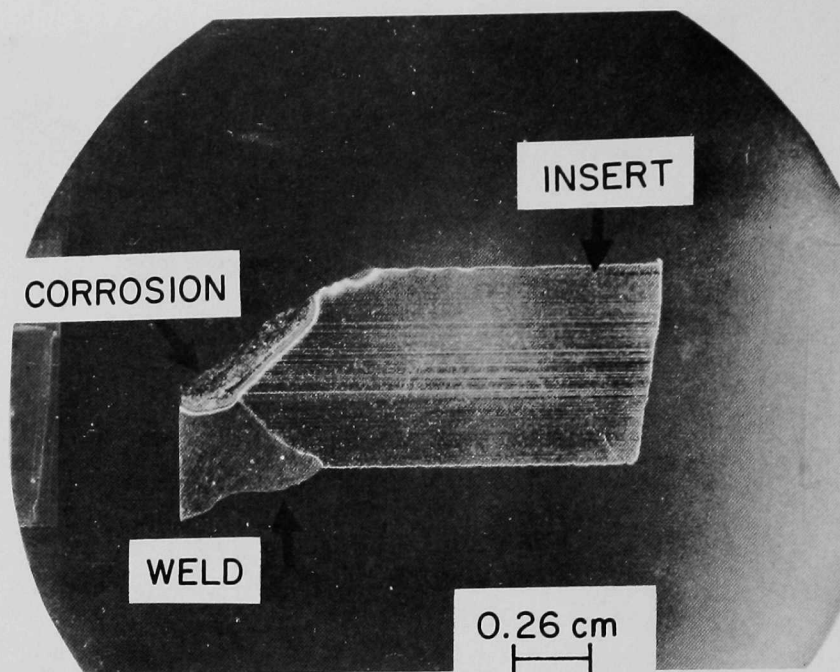
99

Fig. 70. Photograph of a Polished and Etched Cross Section of the Hard-faced Insert. The weld and insert material are shown. Neg. No. ANL-306-78-587
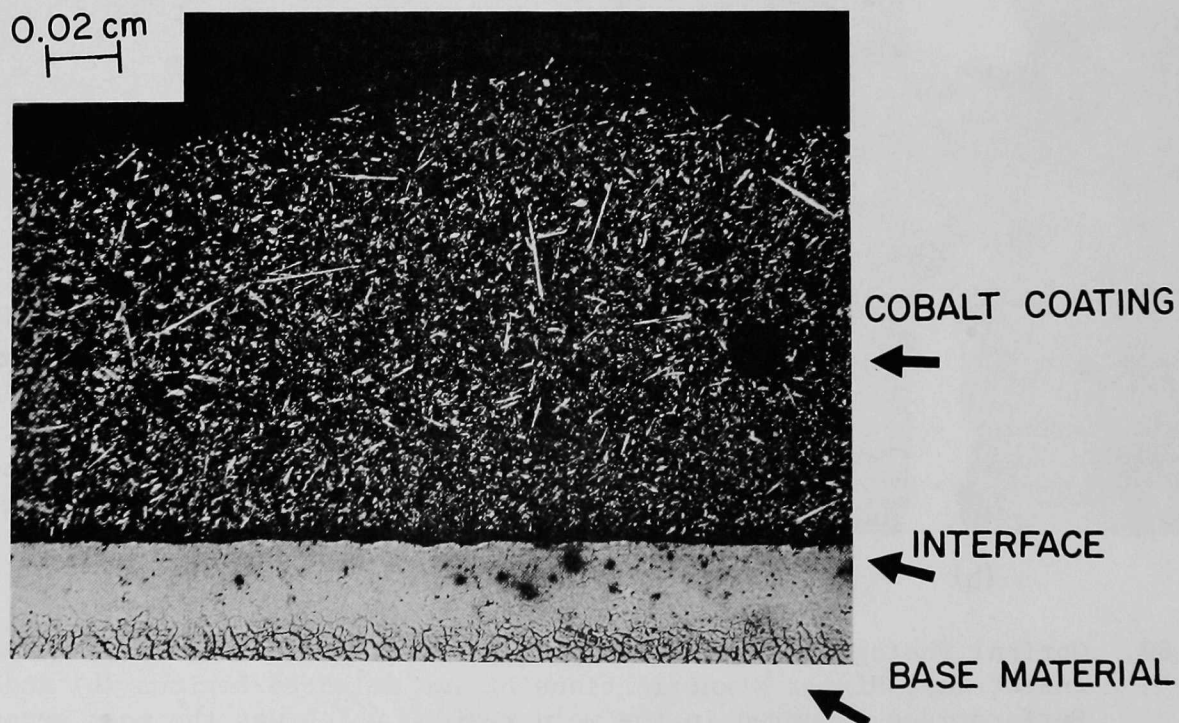

Fig. 71. Micrograph of a Cross Section of the Cobalt Hardfacing. The micro-structure in the coating appears similar to ferrite and pearlite that are formed in iron-based alloys. Neg. No. ANL-306-78-586
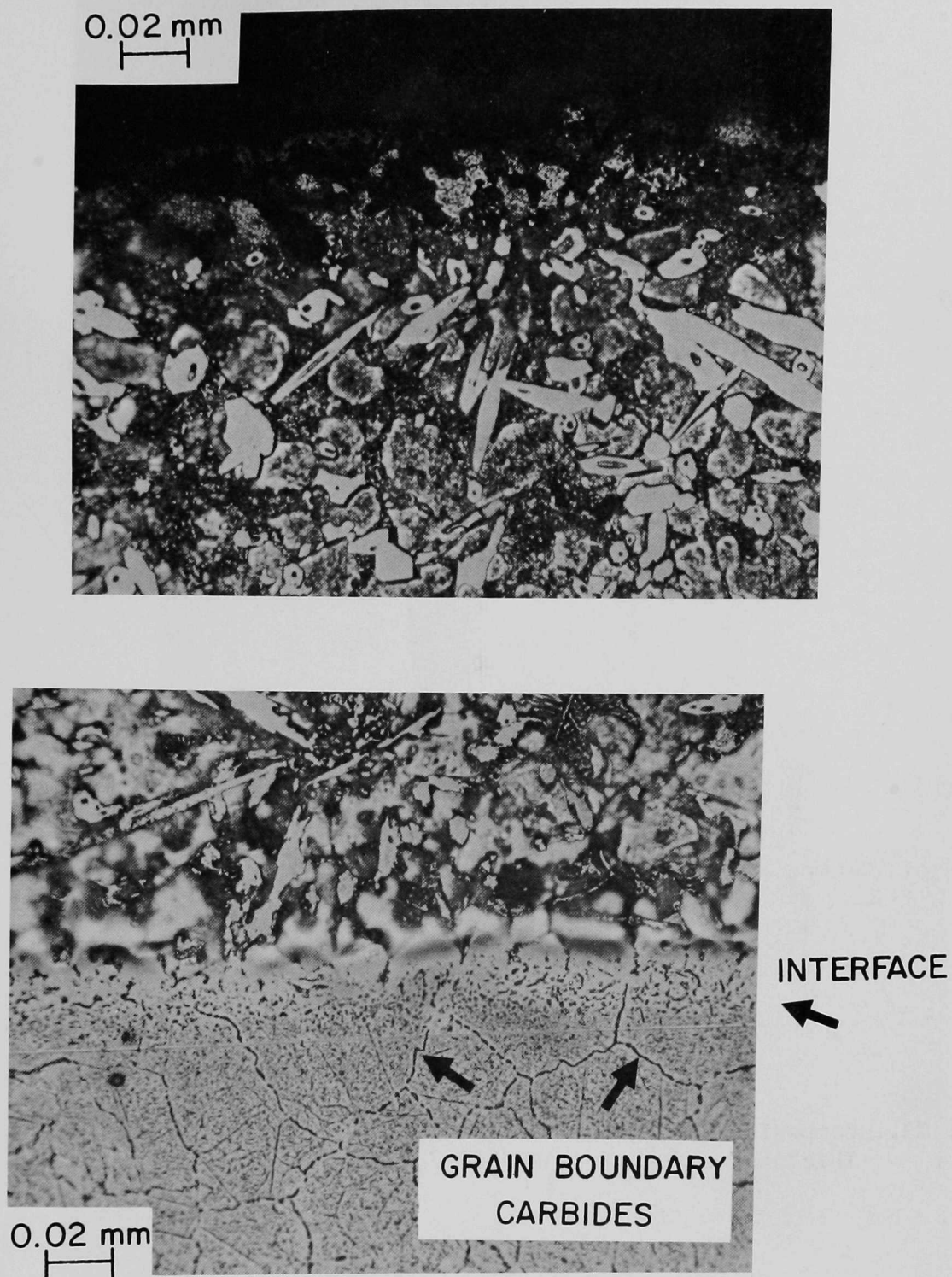
Fig. 72. Microstructure of the Cobalt Hardfacing and the Inter-
face Between the Coating and Substrate. The micro-
structure in the coating appears similar to ferrite and
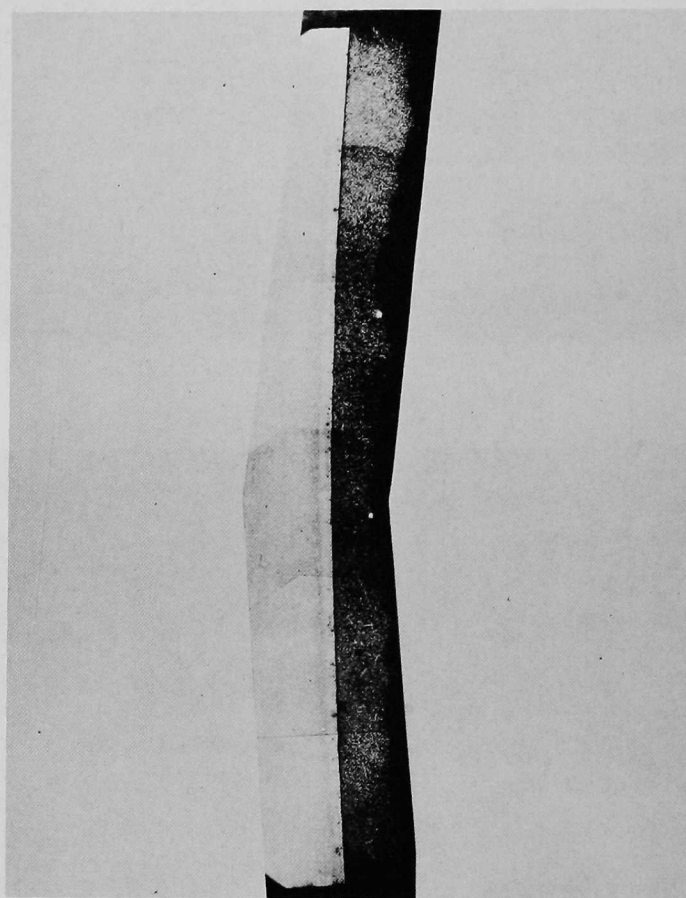pearlite that are formed in iron-based alloys. ANL Neg.
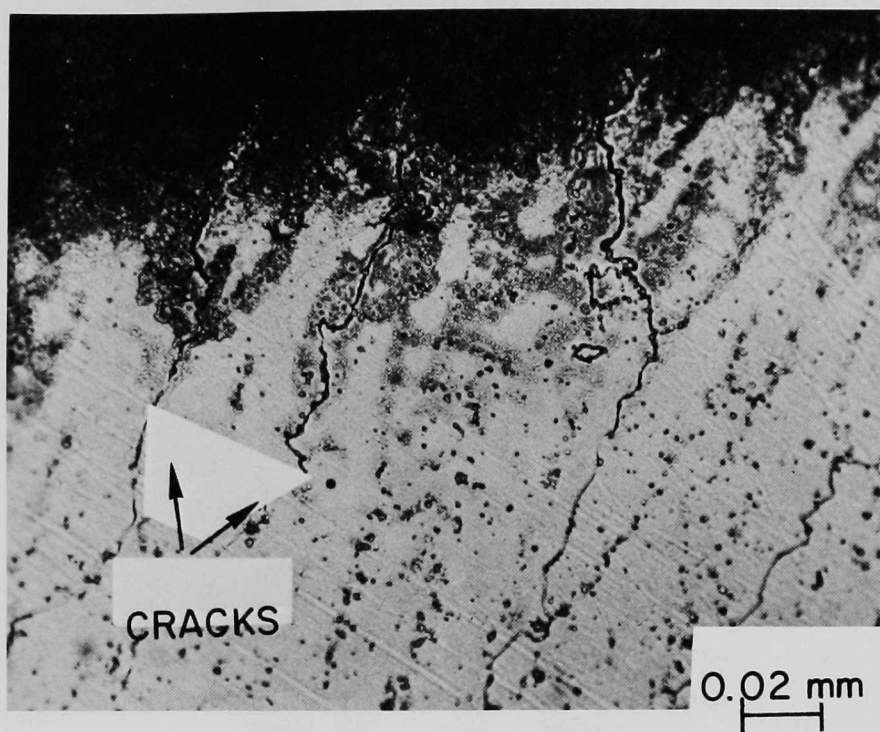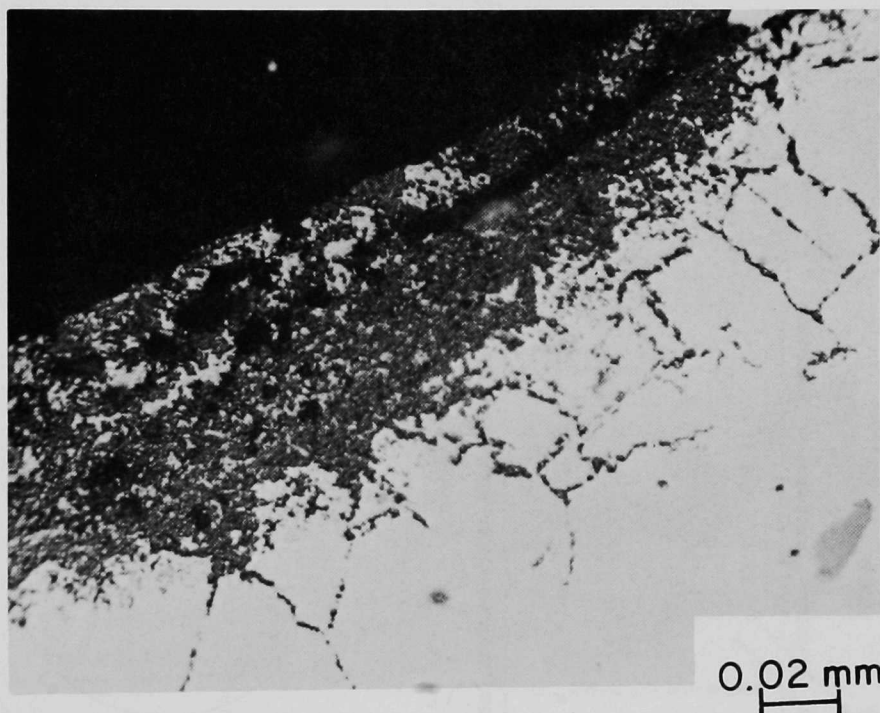No. 306-78-584

Fig. 73. Composite Photograph of the Coating, Showing the Nonuniform Coating Thickness. Neg. No. ANL-306-78-565

Fig. 74. Micrographs of Cracks at the Interface Between the Coating and Sub-
strate (a) and Corrosion and Sulfide Formation Near the Weld Region
(b). ANL Neg. No. 306-78-585

COAL
LOCK

6'-7"

TC

GAS
OFFTAKE

23'-3"

37'-11"

TC

TC

TC

OXYGEN-
STEAM
TUYERES

16 3/8"

34"

SLAG
BREAKER

SIGHT
TUBE

SLAG
LOCK

8'-1"

16 3/8" diam

1/4" od Hastelloy
coil

1"

Rotating slag breaker

Reciprocating slag breaker

Gas burner

Thermocouple

Slag breaker

Slag observation port
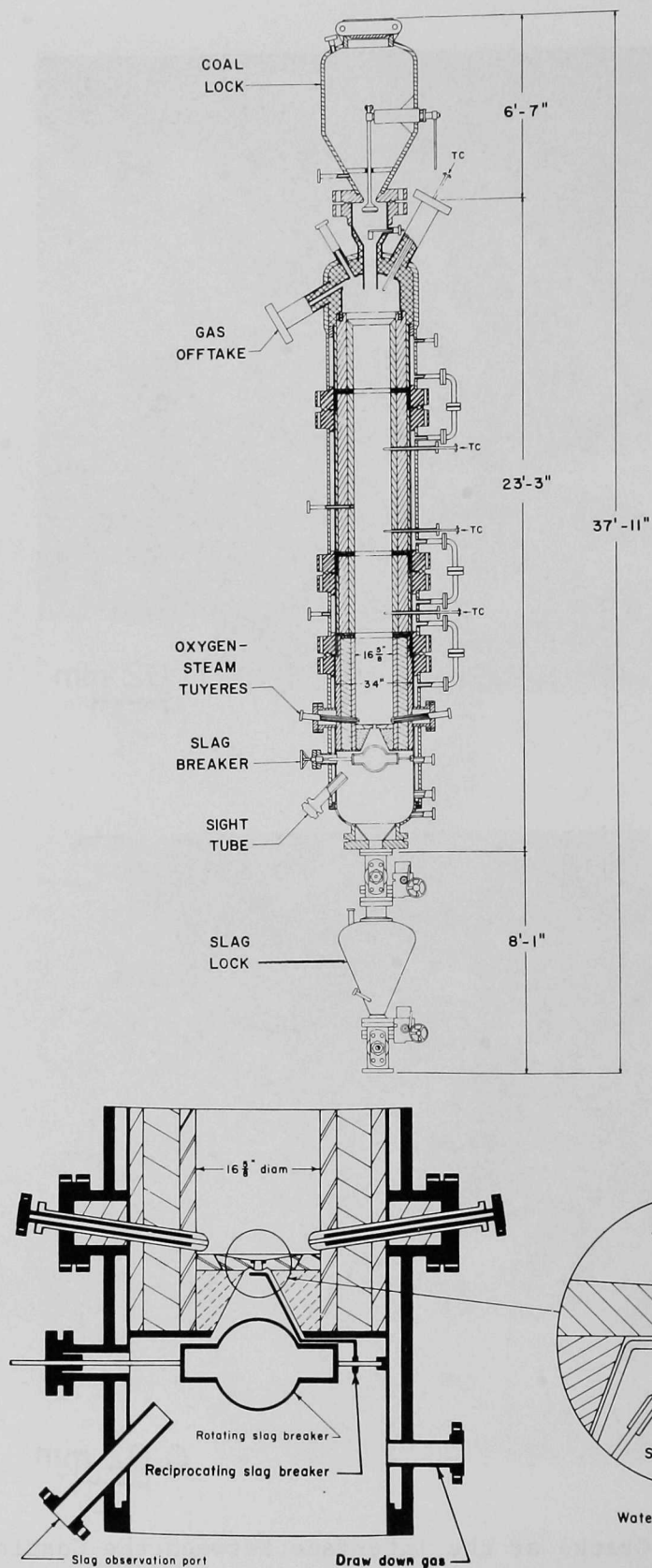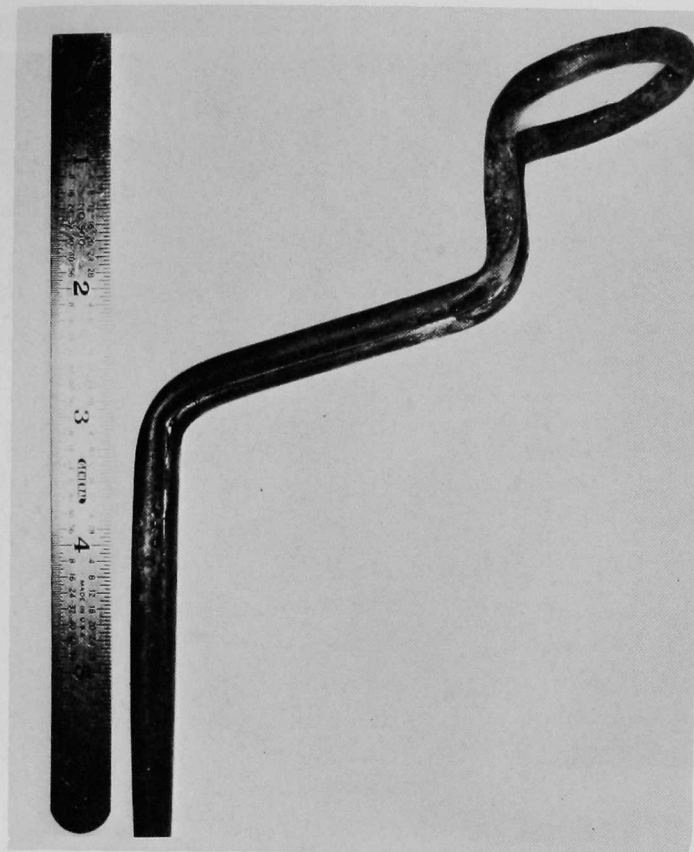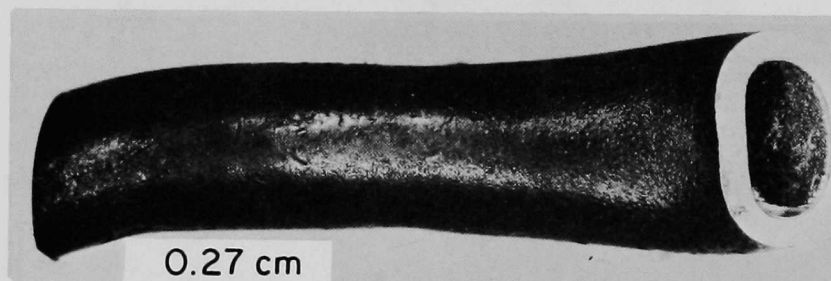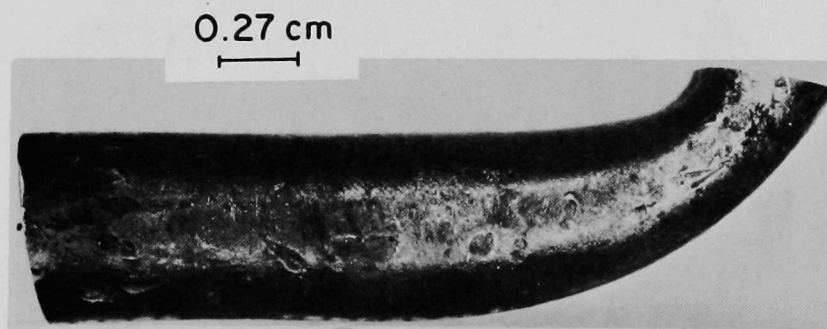
Draw down gas

Water-cooled taphole

Fig. 75. Schematic of the Grand Forks Energy Research Center Slagging Gasifier
and an Enlarged View of the Hearth Plate Section and Water-cooled
Taphole. ANL Neg. No. 306-78-567

Fig. 76. Optical Photographs of the Taphole Cooling Coil: Overall view (a), Cross-sectional View (b), and Top View (c). The tube ID is out of round, and the outer surface contains many imperfections. ANL Neg. No. 306-78-572
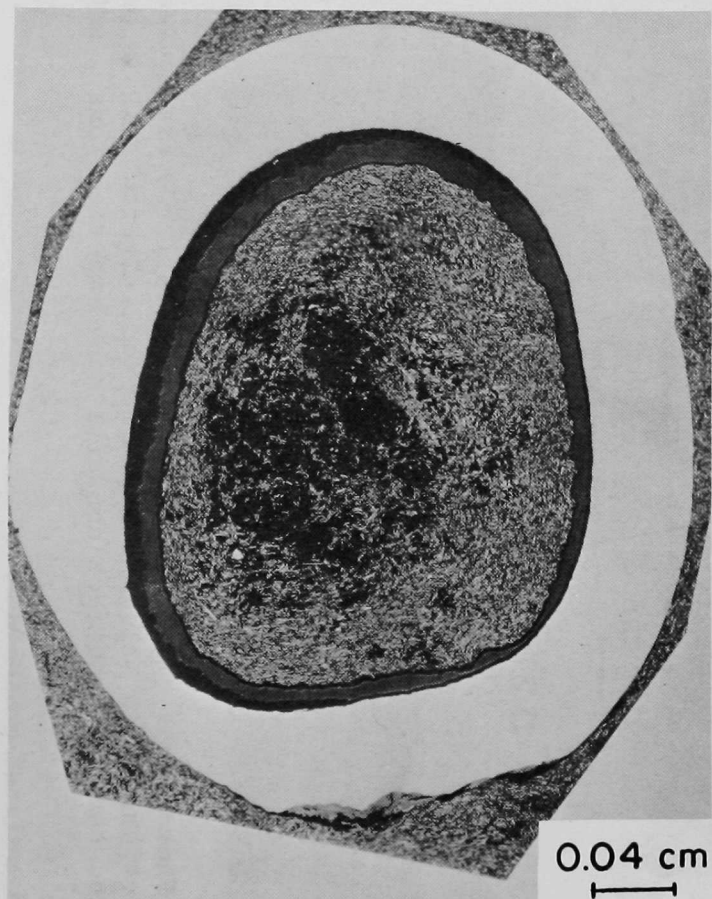
Fig. 77. Optical Photograph of a Cross Section of the Taphole Cooling Coil. A corrosion scale is seen at the ID, and localized corrosion is visible at the OD. Neg. No. ANL-306-78-575
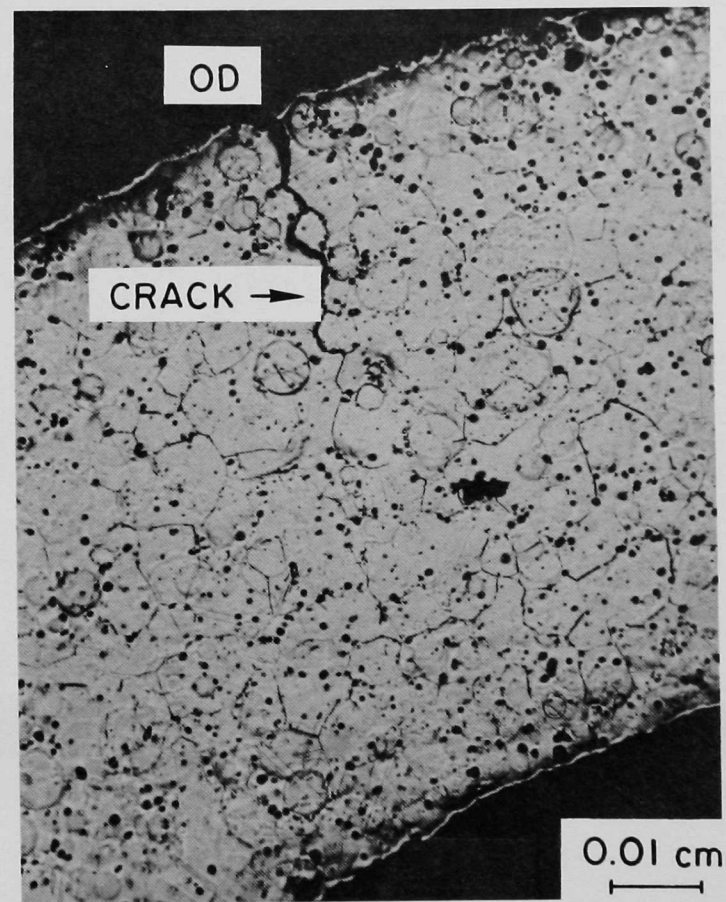
Fig. 78. Polished and Etched Micrograph of a Crack in the Hastelloy G Taphole Cooling Coil. The crack propagates from the OD toward the ID and is intergranular. Higher-magnification micrographs of this crack are shown in Fig. 79. Neg. No. ANL-306-78-577
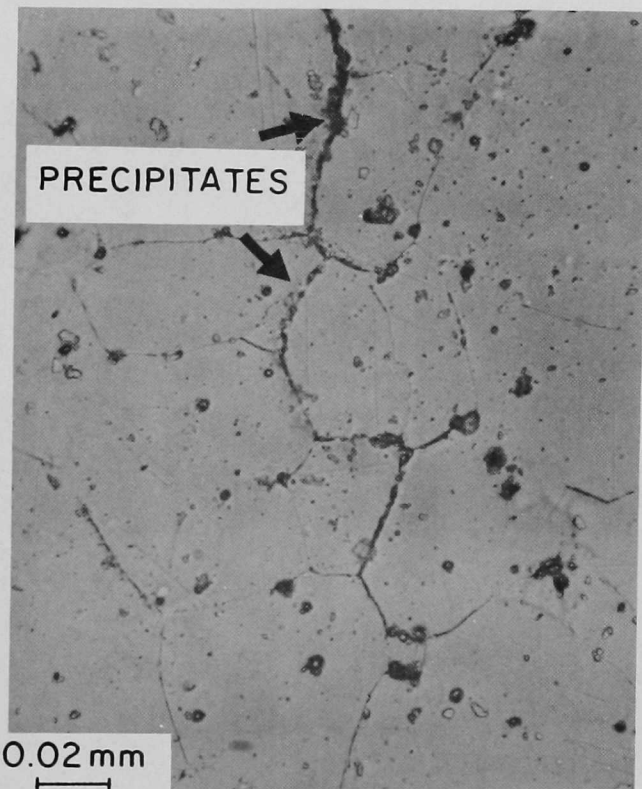
Fig. 79. Enlarged Micrographs of the Intergranular Crack Shown in Fig. 78. Recrystallization is visible at the OD where the crack initiated, and precipitates are observed at the grain boundaries. ANL Neg. No. 306-78-576

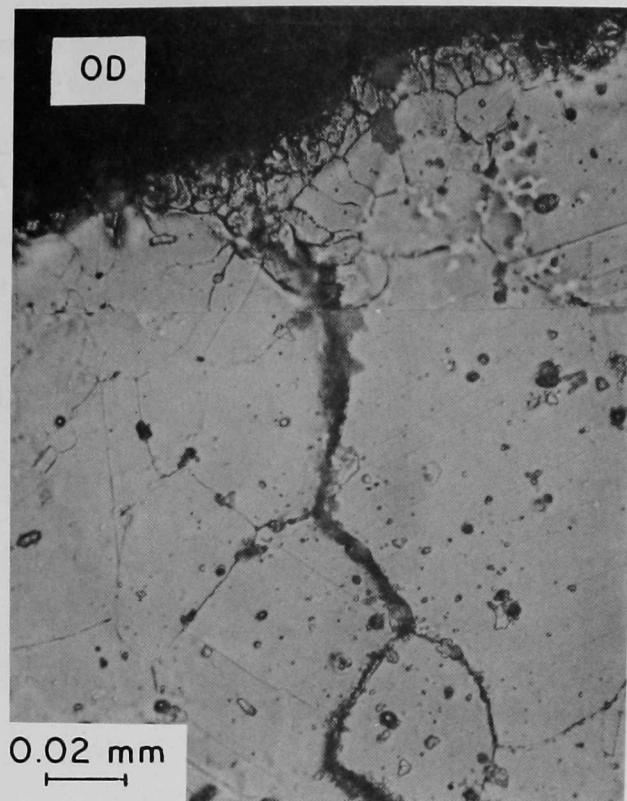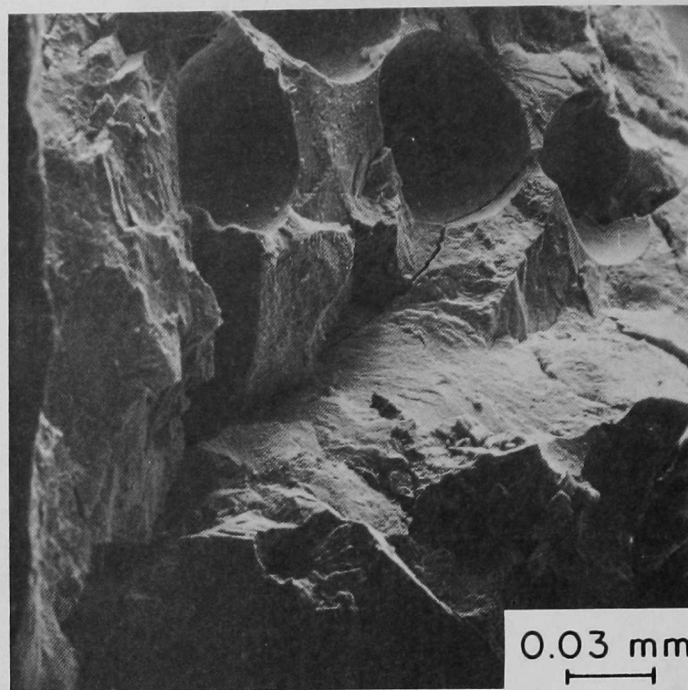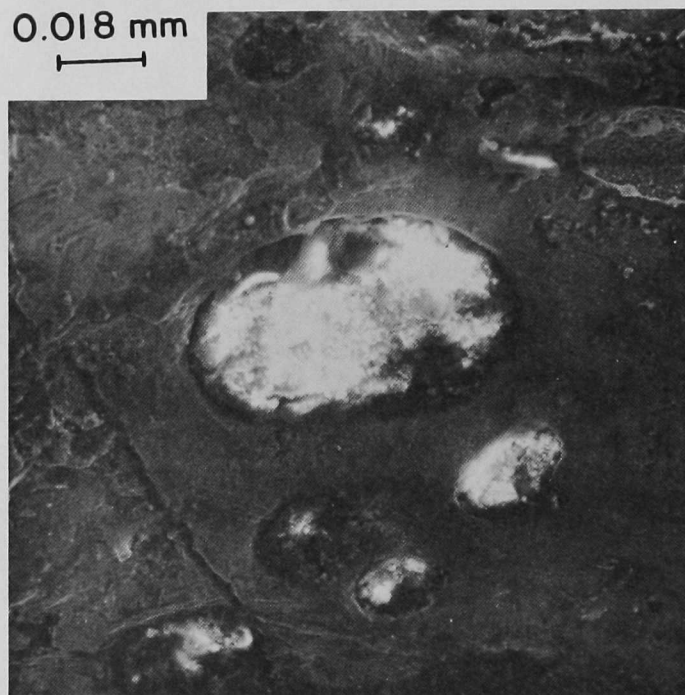Fig. 80. Scanning-electron Micrographs of the Fracture Surface (a) and the Outer Surface (b). Circular regions on the fracture surface in (a) contained non-conducting phases as shown in (b). ANL Neg. No. 306-78-571

REFERENCES

1. Materials Technology for Coal-Conversion Processes: Twelfth Quarterly Report, July-September, 1977, Argonne National Laboratory, ANL-78-6.

2. Materials Technology for Coal-Conversion Processes: Eleventh Quarterly Report, April-June, 1977, Argonne National Laboratory, ANL-77-62.

3. J.W. Byron, Phillips Petroleum Company, Homer City, PA, personal communication.

4. Materials Science Division Coal Technology Tenth Quarterly Report, January-March, 1977, Argonne National Laboratory, ANL-77-41, p. 2.

5. Materials Science Division Coal Technology Eighth Quarterly Report, July-September, 1976, Argonne National Laboratory, ANL-76-125, p. 11 .

6. Metals Handbook, 8th Ed. (American Society for Metals, 1976), Vol. 11, p. 165.

7. C. Eckart, "The Scattering of Sound from the Sea Surface", J. Acoust. Soc. Am., 25 (3), 566-570 (1953).

8. Horton, C.W. and Muir, T.G., "Theoretical Studies on the Scattering of Acoustic Waves from a Rough Surface", J. Acoust. Soc. Am., 41 (3), 627-634 (1967).

9. Horton, C.W., Mitchell, S.K., and Barnard, G.R., "Model Studies on the Scattering of Acoustic Waves from a Rough Surface", J. Acoust. Soc. Am., 41 (3), 635-643 (1976).

10. Welton, P.J., Frey, H.G., and Moore, P., "Experimental Measurements of the Scattering of Acoustic Waves by Rough Surfaces", J. Acoust. Soc. Am., 52 (5, Part 2), 1553-1563 (1972).

11. Tu, C.M. and Fung, A.K., "Backscatter Measurements of Acoustic Waves Scattered from Statistically Known Inhomogenous Rough Media", J. Acoust. Soc. Am., 53 (3), 953-954 (1973).

12. Boyd, M.L. and Deavenport, R.L., "Forward and Specular Scattering from a Rough Surface: Theory and Experiment", J. Acoust. Soc. Am., 53 (3), 791-801 (1973).

13. deBilly, M., Cohen-Ténoudji, F., Jungman, A., and Quentin, G.J., "The Possibility of Assigning a Signature to Rough Surface Using Ultrasonic Backscattering Diagrams", IEEE Trans. Sonics Ultrason., SU-23 (5), 356-363 (1976).

14. deBilly, M., Doucet, J., and Quentin, G.J., "Angular Dependence of the Backscattered Intensity of Acoustic Waves from Rough Surfaces", Ultrasonics International 1975 (IPC Science and Technology Press, Ltd., Surrey, England), paper 11.2.

15. Quentin, G., deBilly, M., Cohen-Ténoudji, F., Doucet, J., and Jungman, A., "Experimental Results on the Scattering of Ultrasound by Randomly or Periodically Rough Surfaces in the Frequency Range 2 to 25 MHz", 1975 Ultrasonics Symposium Proceedings, IEEE Cat. No. 75 CHO 994-4SU, pp. 102-106.

16. Wadin, J.R. and Dunegan, H.L., "The Use of Spatial Filtering and Distribution Analysis of Acoustic Emission Signals to Isolate and Characterize Subcritical Crack Growth", Proc. Third Acoustic Emission Symposium, Tokyo, Japan, September 16-18, 1976.

17. Davis, W.R., "Acoustic Emission in Refractory Materials", Proceedings of the Institute of Acoustics Symposium on Acoustic Emission, December 21-22, 1976, Paper 4-18-1.

18. Materials Science Division Coal Technology Ninth Quarterly Report, October-December, 1976, Argonne National Laboratory, ANL-77-5.

Internal:

E. G. Pewitt
R. G. Matlock
B. R. T. Frost
R. W. Weeks (6)
M. F. Adams
O. K. Chopra
S. Danyluk
D. R. Diercks

W. A. Ellingson (6)
J. Fischer
K. J. Reimann
C. A. Youngdahl
A. A. Jonke
T. F. Kassner
C. R. Kennedy
K. Natesan

E. L. Hartig
J. Y. Park
R. B. Poeppel
W. J. Shack
A. B. Krisciunas
ANL Contract Copy
ANL Libraries (5)
TIS Files (6)

External:

DOE-TIC, for distribution per UC-90c (276)
Manager, Chicago Operations Office
Chief, Chicago Patent Group
President, Argonne Universities Association
Materials Science Division Review Committee:
    G. S. Ansell, Rensselaer Polytechnic Inst.
    R. W. Balluffi, Cornell Univ.
    S. L. Cooper, Univ. Wisconsin
    S. Doniach, Stanford Univ.
    H. L. Falkenberry, Tennessee Valley Authority
    C. Laird, Univ. Pennsylvania
    D. Lazarus, Univ. Illinois
    M. T. Simnad, General Atomic
    A. R. C. Westwood, Martin Marietta Laboratories
R. R. Adams, Battelle Columbus Laboratories
E. M. Anderson, The Babcock & Wilcox Company
W. G. Bair, Inst. of Gas Technology
W. Bakker, USDOE/FE
J. A. Brooks, Amoco Oil Co., Naperville, Ill.
S. Carson, CE Lummus Co., Bruceton, Pa.
W. C. Corder, Battelle Columbus Laboratories
M. Crowley, Standard Oil of Indiana, Naperville, Ill.
J. Flagg, Universal Oil Products Co., Des Plaines, Ill.
E. Fox, Stearns-Roger Corp., Homer City, Pa.
H. E. Frankel, USDOE/FE
S. M. Gaitonde, Commonwealth Edison Co., Maywood, Ill.
D. Glaser, Stearns-Roger Corp. Denver
H. Heysteck, Tuscaloosa Metallurgy Research Center, University, Ala.
V. Hill, IIT Research Inst.
D. Hull, Phillips Petroleum Co., Homer City, Pa.
R. I. Jaffeee, Electric Power Research Institute
D. L. Keairns, Westinghouse Research Labs.
H. Leavenworth, Albany Metallurgy Research Center
A. V. Levey, Lawrence Berkeley Laboratory
R. Lewis Synthane Pilot Plant, USDOE/FE, Pittsburgh
G. Long, Northern Illinois Gas Co., Aurora
R. M. Lundberg, Commonwealth Edison Co., Chicago
J. M. O'Donnell, The Lummus Co., Bloomfield, N. J.
A. L. Plumley, Combustion Engineering Power Systems, Windsor